

REPORT DOCUMENTATION PAGE

AFRL-SR-AR-TR-02-

Public reporting burden for this collection of information is estimated to average 1 hour per response, including the time for reviewing instructions, gathering existing data needed, and completing and reviewing this collection of information. Send comments regarding this burden estimate or any other aspect of this burden to Department of Defense, Washington Headquarters Services, Directorate for Information Operations and Reports (0704-0188), 4302. Respondents should be aware that notwithstanding any other provision of law, no person shall be subject to any penalty for failing to comply with a collection of information if it does not have a valid OMB control number. PLEASE DO NOT RETURN YOUR FORM TO THE ABOVE ADDRESS.

0354

1. REPORT DATE (DD-MM-YYYY) 12-10-2002		2. REPORT TYPE Final Report		3. DATES COVERED (From - To) 15-09-2001 to 14-09-2002	
4. TITLE AND SUBTITLE Flight Demonstration of Stealthy Closed-Loop Attitude Control				5a. CONTRACT NUMBER F49620-01-C-0044	
				5b. GRANT NUMBER	
				5c. PROGRAM ELEMENT NUMBER 65502F	
6. AUTHOR(S) A. B. Cain, T. T. Ng, E. J. Kerschen, H. F. Fasel, E.D. Fasse and D. M. Israel				5d. PROJECT NUMBER 66STTR	
				5e. TASK NUMBER	
				5f. WORK UNIT NUMBER	
7. PERFORMING ORGANIZATION NAME(S) AND ADDRESS(ES) Innovative Tech. Appl. Co. University of Arizona P.O. Box 6971 P.O. Box 210158 Chesterfield, MO 63006 Tucson, AZ 85721-0158				8. PERFORMING ORGANIZATION REPORT NUMBER ITAC-TR-1-2002	
9. SPONSORING / MONITORING AGENCY NAME(S) AND ADDRESS(ES) Air Force Office of Sci. Res. 4015 Wilson Blvd. Arlington, VA 22203-1954				10. SPONSOR/MONITOR'S ACRONYM(S) AFOSR	
				11. SPONSOR/MONITOR'S REPORT NUMBER(S)	
12. DISTRIBUTION / AVAILABILITY STATEMENT Approved for public release, distribution unlimited					
13. SUPPLEMENTARY NOTES					
14. ABSTRACT Flight demonstration of modern stealthy aircraft with an active flow control system is an important, complex, and challenging problem. The probability of success in the current program was maximized by a progressive plan in which complexity was introduced gradually. Active flow control systems for stealthy maneuvering were advanced on several fronts in this Phase I STTR program. A simple closed-loop control system that integrates active flow control (suction) actuators and sensors was developed and demonstrated in laboratory experiments. Feedback control of flow separation using unsteady blowing/suction was investigated using theory and computational fluid dynamic simulations. Finally, pulsed-jet active flow control actuators were developed and demonstrated in flight tests using a modified radio-controlled model plane (88 inch wingspan and 60 mph flight speed). The active flow control actuators were employed in specially designed wing tip regions of the model plane. The flight tests demonstrated high authority roll control using these stealthy active flow control actuators.					
15. SUBJECT TERMS Active Flow Control, Actuators, Sensors, Closed-Loop Control, Flight Demonstration					
16. SECURITY CLASSIFICATION OF:			17. LIMITATION OF ABSTRACT	18. NUMBER OF PAGES	19a. NAME OF RESPONSIBLE PERSON Alan B. Cain
a. REPORT	b. ABSTRACT	c. THIS PAGE			19b. TELEPHONE NUMBER (include area code) (314) 576-1639

1122 142

Final Report
Flight Demonstration of Stealthy Closed-Loop Attitude
Control

A. B. Cain, T. T. Ng, E. J. Kerschen, H. F. Fasel, E. D. Fasse and D. M. Israel

October 12, 2002

20021122 142

Contents

1	Introduction	3
1.1	Background	3
1.2	Phase I Technical Objectives	3
1.3	Final Report Overview	4
2	Theory and Simulations for Feedback Control of Flow Separation	5
2.1	Introduction	5
2.2	Transfer functions	6
2.2.1	Instability wave transfer function	6
2.2.2	Actuator transfer function	7
2.2.3	Generalization to arbitrary time dependence	8
2.3	System response in the presence of feedback	9
2.3.1	System response in the absence of incident instability waves	10
2.3.2	System response in the presence of incident instability waves	11
2.4	Implications for closed-loop control of separation	13
2.4.1	General considerations	13
2.4.2	Characteristics of $A(\omega)$ and $G(\omega)$, and implications for $R(\omega)$	15
2.5	Schemes for Feedback Control of Flow Separation	17
2.5.1	Phase control feedback scheme	18
2.5.2	Frequency/Amplitude control feedback scheme	19
2.6	CFD simulations of reactive flow control	21
2.7	Reduced Order Modeling of Actuator/Flow system	23
2.7.1	Phase Control Feedback Scheme Simulations	26
2.7.2	Frequency/Amplitude Control Feedback Scheme Simulations	34
2.8	Summary	36
3	Experimental Investigation of Sensor Triggered Vortex Generators	37
3.1	Airfoil Geometry	37
3.2	Experimental Evaluation Tools	39
3.3	Control Methods	39
3.4	Airfoil No. 1 Results	39
3.5	Airfoil No. 2 Results	40
3.6	Airfoil No. 3 Results	40
3.6.1	Pressure Data	42
3.6.2	Simple Control Schemes	43
3.7	Summary	49
4	Flight test program	50
4.1	Development of actuators for flight demonstration airplane	51
4.2	Development and construction of flight models (UA-1)	51
4.3	Flight Testing	52

4.4	Summary	53
5	Conclusions	54
5.1	Experimental Investigation of Sensor Triggered Vortex Generators	54
5.2	Flight test program	54
A	Initial Computational Fluid Dynamic (CFD) Simulations	57
B	Sliding-Mode Control Applied to Aircraft Attitude Control	63
B.1	Introduction	63
B.1.1	Motivation	63
B.1.2	Objectives	64
B.2	Technical Details	65
B.2.1	Control Problem	65
B.2.2	Tracking Error	65
B.2.3	General Case: Attitude Control of Spatial Mechanical Systems	67
B.2.4	Attitude Control of Aircraft	70
B.3	Simulation Results	74

1 Introduction

1.1 Background

Active flow control has been a major area of research in fluid mechanics during the past decade. Active flow control is aimed at controlling phenomena such as boundary layer separation, fluid mixing, and flow related noise. Applications in the aerospace industry include: improved combustors, reduced drag, enhanced vehicle maneuvering, forebody yaw control, and reduction of cavity acoustic resonance levels. Another application of increasing importance is the maneuvering of a stealthy air vehicle that has no hinged control surfaces. It is this last application that we wish to focus our attention on, though the advances developed in our program should have payoffs for all the above applications.

A variety of active flow control actuators have been developed, including synthetic jets, steady and pulsed vortex generator jets, etc. These actuators typically introduce longitudinal vortices, or stimulate the naturally occurring spanwise vortices associated with the Kelvin-Helmholtz instability of an inflectional mean-flow profile. For both approaches, demonstrations have shown that these techniques can eliminate or reduce the occurrence of flow separation, which has obvious benefits for aircraft flight performance. Most of the research in active flow control systems has been of an open-loop nature, in which the control input was determined based on an a priori consideration of the instability features of the specific flow field, and feedback was not utilized in adjusting the control input.

Applications such as flight control require closed-loop control systems. Closed-loop control methods have been developed extensively, with much work on nonlinear methods in the last decade. Advances in control system theory have contributed greatly to the maneuvering performance of military aircraft. The integration of active flow actuators with a closed-loop control system would provide a number of benefits. Since flow separation at high angles of attack limits aircraft maneuvers, the use of active control actuators to eliminate or reduce separation could significantly expand maneuvering performance. Another application of active flow control actuators to aircraft maneuvering is as a stealthy replacement for conventional hinged control surfaces. In the present program, we focus on the latter application as a test bed for the integration of active flow actuators into a closed-loop control system.

The integration of active flow control actuators with flight control systems offers the potential for a breakthrough in aircraft maneuvering and stealth performance. The development of such an integrated system is not without risk, however. Stealthy aircraft, which have planforms exhibiting marginal stability characteristics and minimal or no hinged control surfaces, tend to have challenging flight characteristics. Thus, in order to minimize risk in this important but challenging opportunity, we followed an approach in which complexity was introduced gradually.

1.2 Phase I Technical Objectives

Implementation of active flow control actuators in a closed-loop flight control system is the basic advance that was proposed in this Phase I STTR program. A number of programs have focused

on development of active flow control actuators, and modern control theory is one of the great successes of the past forty years. However, only a few projects have combined active flow control actuators with a feedback control system to truly demonstrate closed-loop active flow control. Our program focused on the simpler case of aircraft roll control in Phase I, with the intention to extend this to three-axis control in follow-on work. The original objectives as stated in the proposal were:

1. Use modern control theory to achieve robust closed-loop control
2. Develop a reduced-order model for the aerodynamic response to the active flow actuators
3. Perform a flight demonstration of closed-loop roll control employing active flow actuators
4. Develop a Phase II plan for demonstration of multi-axis closed-loop attitude control of a stealthy vehicle, employing active flow actuators

This Phase I program began September 15, 2001. In December, we presented our initial efforts to Air Force personnel at a meeting in Dayton, and received suggestions regarding the program focus. Based on the feedback from this meeting, we decided to increase the emphasis on “inner-loop” feedback control of flow separation, and to de-emphasize the “outer-loop” feedback control of aircraft attitude by sliding-mode methods. For the sake of completeness, the work performed on attitude control and sliding-mode methods is included as Appendix B of this report.

1.3 Final Report Overview

Sections 1.1 and 1.2 provide a context in which this STTR Phase I work was done. The outline of the remainder of this report is as follows. Section 2 presents theory and computational fluid dynamic simulations for feedback control of flow separation, which were developed in response to government suggestions received at the December 2001 meeting. Section 3 presents wind tunnel experiments on the implementation of sensors, vortex-generator actuators, and primitive feedback control. Section 4 discusses our successful flight demonstration program, in which open-loop active flow control actuators were utilized to achieve high-authority roll control of a modified scale-model radio controlled aircraft. Appendices A and B describe computational fluid dynamic simulations and work on sliding mode control, which was done prior to the December 2001 government review, and was focused on “outer loop” attitude control as described in our original proposal.

2 Theory and Simulations for Feedback Control of Flow Separation

2.1 Introduction

In this section, we present theoretical considerations relating to the use of feedback to enhance the control of flow separation by active flow control actuators. The separation control strategy that we pursue is the excitation of strong instability waves on the separated or marginally separated flow, in order to increase the mixing and entrainment and thereby cause the flow to reattach. This effect has been well demonstrated (e. g. Greenblatt and Wygnanski, 2000) in open-loop active flow control schemes, where an actuator is driven by a time-harmonic input to generate an instability wave in the (pre-determined) unstable frequency range.

In the open-loop approach, the forcing is applied without any feedback concerning the instantaneous state of the flow field, so that forcing must be applied at sufficient amplitudes to dominate the pre-existing field. The open-loop approach does take advantage of the exponential amplification of flow instabilities, so that modest forcing levels can produce very strong effects. However, forcing that reinforces the pre-existing instability wave field should be even more advantageous in effecting flow control. In order to achieve this, a feedback scheme must be introduced into the approach.

Previous work has shown that open-loop active flow control by instability wave excitation is quite robust. Therefore, it seems reasonable to anticipate that system behavior in the presence of feedback would also be quite robust. Note that we are considering the introduction of a feedback scheme to *enhance*, rather than *suppress* a flow instability. In order to *suppress* an exponentially growing instability, the amplitude and phase of the feedback signal must be determined very precisely. In contrast, much less precision is required in order to *enhance* an existing instability.

Our objective then, is to devise a simple feedback system for enhancing the naturally occurring instabilities on a separated or marginally separated boundary layer. Essentially, the actuator input must be chosen so that the instability waves it produces are in phase with the existing instability wave field, thereby enhancing rather than suppressing the existing instability wave field. In this section, we develop a linear model for the response of the system in the presence of feedback. We recognize, of course, that the final state of the system will involve large amplitude instability waves, and hence contain nonlinear effects. However, the linear analysis provides crucial guidance on the phase and amplitude relationships necessary for initial enhancement of the instability waves. The level of system modelling that is attempted here is similar to a recent study of feedback control of acoustic cavity resonances by the Caltech team of Rowley, Murray and their co-investigators (Rowley et al., 2002).

In order to utilize feedback enhancement of the instability wave field, some quantity related to the instability waves must be measured. Since our goal is the control of separation, it might seem most attractive to measure a quantity directly related to flow separation, such as the local wall shear stress. However, the wall shear becomes very small in the separated region, so that is is not directly useful as a feedback signal. Therefore, we will consider the use of wall unsteady pressure as a feedback signal. As adverse-pressure-gradient boundary layers approach separation

or separate completely, strong two-dimensional instabilities arise on the inflectional profile. These two-dimensional instabilities have a strong pressure field, which convects downstream at the phase speed of the instability wave. As long as the separated shear layer remains reasonably close to the surface, a strong unsteady pressure field will be present on the surface. Our approach uses measurements of this unsteady pressure field to determine the appropriate frequency, phase and amplitude at which to drive the upstream actuator. More generally, we require a feedback law that converts the output signal from a downstream sensor to an appropriate input signal for the upstream actuator.

In Section 2.2, we discuss the transfer functions for the generation of the instability wave by the upstream actuator, and for the propagation of the instability wave to the location of the downstream sensor. In Section 2.3, we use these transfer functions to analyze the linear response of a closed-loop system incorporating feedback from a downstream sensor. In Section 2.4, we discuss the implications of the analysis for the design of a feedback scheme. In Section 2.5, two feedback schemes for enhancing flow instability wave amplitudes to control flow separation are presented. In § 6, CFD simulations that will be used to develop, evaluate and refine these initial feedback schemes are discussed. ****LAST SENTENCE NEEDS TO BE MODIFIED****

2.2 Transfer functions

We first consider transfer functions for time-harmonic disturbances. After developing the results for harmonic time dependence, Fourier transforms will be used to generalize the results to arbitrary time dependence. For time-harmonic disturbances, we adopt the notation

$$f(x, y, t) = F(x, y)e^{-i\omega t}. \quad (1)$$

We generally consider real functions $f(x, y, t)$. This requirement may be satisfied either by taking the real part of the right-hand side of (1), or by adding the complex conjugate to the right-hand side of (1).

2.2.1 Instability wave transfer function

First consider the transfer function related to downstream propagation of a time-harmonic instability wave. In the simplest case of a parallel mean flow whose characteristics are independent of the streamwise position, the linear stability theory for a disturbance of fixed (real) frequency ω is an eigenvalue problem with solution

$$F(x, y) = \phi(y)e^{i\alpha x}. \quad (2)$$

Here the streamwise wavenumber α is the eigenvalue. In general, $\alpha = \alpha_r + i\alpha_i$ is complex, with real part α_r and imaginary part α_i . If $\alpha_i < 0$, the wave is unstable and grows exponentially with downstream distance. The mode shape $\phi(y)$ is the eigenfunction. The theory can be formulated in terms of any physical quantity of interest. Here, we consider $F(x, y)$ to be the pressure distribution. Then, the wall pressure is given by $\phi(0)$.

To formulate a system model, consider an actuator located on the wall at $x = x_0$ and a pressure sensor located on the wall at $x = x_1$, where $x_1 > x_0$. In the following, we will only consider

quantities at the surface ($y = 0$), and the dependence on y will be suppressed. For the simple case of a parallel mean flow, the transfer function relating the wall pressure for the instability wave at the sensor location, $p(x_1, t)$, to that at the actuator location, $p(x_0, t)$, is simply

$$\frac{P(x_1)}{P(x_0)} = G(\omega) = e^{i\alpha(x_1-x_0)}. \quad (3)$$

The magnitude and phase of the transfer function are then

$$|G(\omega)| = e^{-\alpha_i(x_1-x_0)}, \quad \text{Arg}[G(\omega)] = \alpha_r(x_1 - x_0). \quad (4)$$

The transfer function $G(\omega)$ is a function of frequency, because the Orr-Sommerfeld eigenvalue α depends on frequency.

In the more general case of a mean flow that varies slowly in the downstream direction, the eigenvalue α would be a 'slow' function of x , and the argument of the exponential in (2) would involve an integral with respect to x . The mode shape function $\phi(y)$ would also be a slow function of x . Similar modifications would appear in the transfer function (3). A mathematical description of this feature would require use of the method of multiple scales.

2.2.2 Actuator transfer function

Next consider the transfer function for the actuator. The actuator model we consider involves blowing/suction through the wall, as is often employed in open-loop active flow control (e. g. Israel and Fasel, 2001). The blowing/suction is concentrated over a streamwise region on the order of half an instability wavelength or shorter. The streamwise distribution of the blowing/suction velocity is antisymmetric about the center of the actuator, so that no net mass is injected into the boundary layer. For present purposes, we may consider the mean flow characteristics and the spatial distribution of the blowing/suction velocity as fixed. Then, the actuator input can be specified in terms of the overall amplitude and phase of the blowing/suction velocity, say

$$v_A(t) = V_A e^{-i\omega t}, \quad (5)$$

Note that V_A is complex; the magnitude of the actuator input is $|V_A|$ and the phase is $\text{Arg}[V_A]$. For a specified time-harmonic actuator input, the amplitude and phase of the resulting instability wave can be determined. Representing the output in terms of the wall pressure of the instability wave at $x = x_0$, the transfer function for the actuator is given by

$$A(\omega) = \frac{P(x_0)}{V_A}. \quad (6)$$

As before, $|A(\omega)|$ is the magnitude of the actuator transfer function, while $\text{Arg}[A(\omega)]$ is the phase. Note that the numerator in the definition (6) is the wall pressure of the instability wave at $x = x_0$, not the wall pressure of the total unsteady field at that point. The actuator transfer function $A(\omega)$ is a function of frequency. It could be obtained analytically by triple-deck theory (Kerschen, 1989), semi-numerically by Orr-Sommerfeld theory, or fully numerically from a CFD code. In this research, the transfer function will be extracted from CFD results.

2.2.3 Generalization to arbitrary time dependence

The basic stability properties of fluid flows are usually developed in terms of time-harmonic disturbances, as considered in the previous subsections. Similarly, the analysis of convective, absolute and global instability of fluid systems (Huerre and Monkewitz, 1990) is most often carried out in terms of Fourier transforms. In contrast, Laplace transforms are commonly employed in linear control theory. Because the fluid mechanics plays a central role in the present discussion, we will analyze the case of arbitrary time dependence using Fourier transforms. The relation of the Fourier transform results to the corresponding Laplace transform results will be noted in the discussion below.

Consider the Fourier transform pair

$$F(\omega) = \int_{-\infty}^{\infty} f(t)e^{i\omega t} dt, \quad f(t) = (2\pi)^{-1} \int_{-\infty}^{\infty} F(\omega)e^{-i\omega t} d\omega. \quad (7)$$

Here, the frequency ω is in general complex. The Fourier transform pair could be converted to the Laplace transform pair by assuming that $f(t) = 0$ for $t < 0$, and substituting $\omega = is$. Thus, behavior found in the right-half of the complex s -plane in Laplace transform analysis, appears in the upper-half of the complex ω -plane in Fourier transform analysis.

Note that, for a function $f(t)$ which is zero for $t < 0$, the transform $F(\omega)$ is analytic in the upper half of the complex ω -plane. More generally, physical behavior for negative values of t is related to singularities above the inversion contour in the complex ω -plane, while physical behavior for positive values of t is related to singularities of $F(\omega)$ below the inversion contour. In the formal definition of the Fourier transform, the inversion contour is nominally the real ω -axis. In the presence of temporal instabilities, however, the inversion contour must be shifted to pass above the corresponding pole in the complex ω -plane.

When the Laplace transform is utilized in control theory, the system is stable if all poles lie in the left half of the complex s -plane. A pole that lies in the right half of the complex s -plane ($\text{Re}[s] > 0$) corresponds to an exponentially growing instability. In the presence of such a pole, the inversion contour of the Laplace transform must be shifted to the right, say from $c - i\infty$ to $c + i\infty$ where $c > 0$. Similarly, when Fourier transforms are utilized, a pole that lies in $\text{Im}[\omega] > 0$ corresponds to an exponentially growing instability. Here also, the inversion contour must be shifted to pass above this pole.

In the case of general time dependence, the pressure at the location of the downstream sensor ($x = x_1$) is given by

$$p(x_1, t) = (2\pi)^{-1} \int_{-\infty}^{\infty} P(x_1, \omega)e^{-i\omega t} d\omega. \quad (8)$$

Note that, apart from the factor $(2\pi)^{-1}$, this integral representation for $p(x_1, t)$ is simply a superposition of the time-harmonic disturbances considered in the previous subsections. Thus, the expressions for the transfer functions discussed in the previous subsections can be used directly. Combining (3) and (6), the wall pressure field at the location of the downstream sensor generated by a specified actuator velocity $V_A(\omega)$ is given in Fourier space by

$$P(x_1, \omega) = A(\omega)G(\omega)V_A(\omega). \quad (9)$$

To return to physical space, we substitute into (8) to obtain

$$p(x_1, t) = (2\pi)^{-1} \int_{-\infty}^{\infty} A(\omega) G(\omega) V_A(\omega) e^{-i\omega t} d\omega. \quad (10)$$

Next, we apply the convolution theorem to (10). Substituting

$$V_A(\omega) = \int_{-\infty}^{\infty} v_A(t') e^{i\omega t'} dt' \quad (11)$$

and reversing the order of integration, we obtain

$$p(x_1, t) = \int_{-\infty}^t T_{AG}(t - t') v_A(t') dt' \quad (12)$$

where

$$T_{AG}(t) = (2\pi)^{-1} \int_{-\infty}^{\infty} A(\omega) G(\omega) e^{-i\omega t} d\omega. \quad (13)$$

The transfer function $T_{AG}(t)$ combines the fluid dynamic effects of the ‘receptivity’ of the actuator and the subsequent instability wave growth. Note that the physical system is causal, so that an actuator input at time t' produces no response for $t < t'$. This feature is reflected in the transform plane by the fact that $A(\omega)$ and $G(\omega)$ are analytic in the upper half plane. Accordingly, $T_{AG}(t)$ is zero for $t < 0$ and this fact is reflected in the upper limit of the integral in (12).

2.3 System response in the presence of feedback

Next, we introduce feedback into the system, in which a feedback law is applied to the output $p(x_1, t)$ of the wall pressure sensor, and the result is fed back as the actuator input $v_A(t)$. Consider a linear feedback relation of the general form

$$v_A(t) = \int_{-\infty}^t r(t - t') p(x_1, t') dt'. \quad (14)$$

Applying the convolution theorem in reverse, this can be represented by

$$V_A(\omega) = R(\omega) P(x_1, \omega), \quad (15)$$

where $R(\omega)$ is the Fourier transform of $r(t)$. Again, to satisfy causality, $R(\omega)$ must be analytic in the upper half of the ω -plane.

Recall that our objective is to use feedback to increase the amplitudes of the instability waves. Two situations are of interest. First, we examine the natural response of the system in the presence of feedback, neglecting any pre-existing instability waves that enter our region of interest across the upstream boundary ($x = x_0$). Second, we consider the response of the closed-loop system in the presence of instability waves incident from the upstream region.

2.3.1 System response in the absence of incident instability waves

In this subsection, we consider the system response in the absence of instability waves incident from the upstream region ($x < x_0$). Thus, the actuator is the only source of instability waves. Since the input to the actuator is linearly related to the instability wave amplitude at the sensor location $x = x_1$ (see (14)), the system response in the absence of an initial disturbance is simply $v_A(t) = 0$, $p(x, t) = 0$. Therefore, in order to deduce the characteristics of the system, we must examine the response of the system to some small input disturbance.

In the Laplace transform approach, we would examine the stability of the system by determining the solution for the case of inhomogeneous initial conditions at $t = 0$. In the Fourier transform approach, we can examine the stability of the system by determining the solution for an impulsive input at $t = 0$.

Adding an impulsive input to the actuator velocity, assume an actuator input of the form

$$v_A(t) = c_\delta \delta(t) + \int_{-\infty}^t r_c(t-t') p(x_1, t') dt' \quad (16)$$

where $\delta(t)$ is the Dirac delta function and c_δ is an arbitrary constant. The Fourier transform of (16) is

$$V_A(\omega) = c_\delta + R(\omega) P(x_1, \omega). \quad (17)$$

Then, substituting (17) into (9), we can solve for $P(x_1, \omega)$, leading to

$$P(x_1, \omega) = \frac{c_\delta A(\omega) G(\omega)}{1 - A(\omega) G(\omega) R(\omega)}. \quad (18)$$

Equation (18) is the representation of the system response in Fourier space. To obtain the system response in physical space, we apply the inverse Fourier transform (7) to obtain

$$p(x_1, t) = (2\pi)^{-1} \int_{-\infty}^{\infty} \frac{c_\delta A(\omega) G(\omega)}{1 - A(\omega) G(\omega) R(\omega)} e^{-i\omega t} d\omega. \quad (19)$$

The inversion contour in (19) is taken above all the singularities in the complex ω -plane. Note that, by causality arguments, the integrand is analytic for $\text{Im}[\omega]$ sufficiently large. By complex variable theory, the value of the integral is related to the singularities of the integrand. We have particular interest in poles of the integrand, which correspond to points where the denominator has a simple zero. Consider such a point, say $\omega = \omega_j$. By residue theory, the pole produces a contribution to the integral of the form

$$p_j(x_1, t) = -iC_j e^{-i\omega_j t} \quad (20)$$

where

$$C_j = \lim_{\omega \rightarrow \omega_j} (\omega - \omega_j) P(x_1, \omega). \quad (21)$$

Hence, the behavior of the closed-loop system depends on the location of the singularities of $P(x_1, \omega)$. If all poles of this function lie in the lower half of the complex ω -plane, the system is stable and the free response of the system to an arbitrary initial condition involves exponential

decay in time. It is important to note that this does not necessarily mean that the instability waves are damped. They may very well be amplified, growing exponentially with downstream distance. However, in this situation the instability waves are at most convectively unstable, and any temporally growing disturbances will wash downstream. For finite values of x , the long-time behavior of the system will decay to zero.

On the other hand, if any pole $\omega = \omega_j$ of $P(x_1, \omega)$ lies in the upper half of the complex ω -plane, then the system exhibits an instability that grows exponentially with respect to time. (Exponential growth with respect to x is also present, if $\text{Im}[\alpha] < 0$.) In the fluid mechanics parlance of convective, absolute and global instabilities, the closed-loop system effectively exhibits a global instability. Hence, in this case, the feedback has modified the nature of the instability.

For a closed-loop system that exhibits a global instability, any small disturbances that are initially present will be amplified exponentially with respect to time, leading to a strong instability wave field. Thus, a feedback law that produces a globally unstable closed-loop system may be an attractive approach for generating a strong instability wave field, and thereby controlling flow separation. This will be discussed further in Section 2.4.

2.3.2 System response in the presence of incident instability waves

Next consider the response of the system in the presence of a pre-existing instability wave field that enters our region of interest through the upstream boundary at $x = x_0$. We denote this incident instability wave field by $p_{\text{inc}}(x, t)$. Since our analysis is linear, the principle of superposition is applicable. Hence, the total instability wave field is the sum of the incident instability wave field and the instability wave field generated by the actuator at $x = x_0$. For the moment, we denote the latter field by $p_A(x, t)$. Thus, the total instability wave pressure field is

$$p(x, t) = p_{\text{inc}}(x, t) + p_A(x, t). \quad (22)$$

The input to the actuator at $x = x_0$ is then given by (14), with $p(x_1, t)$ given by (22) evaluated at $x = x_1$. Applying the Fourier transform to this result, we have

$$V_A(\omega) = R(\omega) [P_{\text{inc}}(x_1, \omega) + P_A(x_1, \omega)]. \quad (23)$$

Substituting this expression into (9), the instability wave field produced by the actuator has the value

$$P_A(x_1, \omega) = A(\omega)G(\omega)R(\omega) [P_{\text{inc}}(x_1, \omega) + P_A(x_1, \omega)] \quad (24)$$

at the location x_1 of the downstream sensor. Equation (24) can be rearranged to provide an expression for the instability wave field produced by the actuator,

$$P_A(x_1, \omega) = \frac{A(\omega)G(\omega)R(\omega)P_{\text{inc}}(x_1, \omega)}{1 - A(\omega)G(\omega)R(\omega)}. \quad (25)$$

Substituting this result into (22), the total instability wave field produced by the response of the closed-loop system to the incident instability wave field $p_{\text{inc}}(x, t)$ is, in Fourier space,

$$P(x, \omega) = \frac{P_{\text{inc}}(x, \omega)}{1 - A(\omega)G(\omega)R(\omega)}. \quad (26)$$

Applying the inverse transform, we have the total field in physical space,

$$p(x, t) = (2\pi)^{-1} \int_{-\infty}^{\infty} \frac{P_{\text{inc}}(x, \omega)}{1 - A(\omega)G(\omega)R(\omega)} e^{-i\omega t} d\omega, \quad (27)$$

valid downstream of the actuator ($x > x_0$). The inversion contour in (27) is again taken above all the singularities of the integrand in the complex ω -plane.

Again, the singularities of the integrand are of interest. Note that the denominator in (27) is identical to that in the solution (19) for the case of an impulsive input in the absence of an incident instability field. This is as expected—the denominator is a representation of the characteristics of the closed-loop system.

First consider the case where all zeros of the denominator lie in the lower half plane. In this case the closed-loop system is globally stable, and the free response of the system decays exponentially to zero. In the presence of forcing by an incident instability wave field, however, the feedback may produce a significant increase in the amplitude of the instability wave field. A convenient way to illustrate this is to consider the inversion contour in (27) as the real ω -axis. At each value of ω along the real axis, the factor

$$M(\omega) = \left| \frac{1}{1 - A(\omega)G(\omega)R(\omega)} \right| \quad (28)$$

is the magnification of the incident instability wave field produced by the feedback system. In the absence of feedback ($R(\omega) = 0$), the magnification factor reduces to unity. However, when $R(\omega)$ is non-zero, a significant magnification of the incident instability wave field is possible, for values of ω such that the denominator of (28) is small. Note that small values of feedback ($|R(\omega)| \ll 1$) may produce significant amplification of the incident instability wave field, when sufficient instability wave growth is present between the actuator and sensor locations ($|G(\omega)| \gg 1$).

Next consider the case where a zero of the denominator of (27) lies in the upper half plane, say at $\omega = \omega_j$. In this case, causality requires that the inversion contour in (27) be shifted into the upper half-plane to pass above this pole. Consider the case where the only singularity in the upper half-plane is the pole at $\omega = \omega_j$. The causal contour, which passes above this pole, can be deformed to lie along the real ω -axis, with an isolated loop extending upward and circling the pole at $\omega = \omega_j$. The complete solution then consists of (27) evaluated along the real axis, plus the residue associated with the pole at $\omega = \omega_j$,

$$p_j(x, t) = -iC_j e^{-i\omega_j t} \quad (29)$$

where

$$C_j = \lim_{\omega \rightarrow \omega_j} \frac{(\omega - \omega_j) P_{\text{inc}}(x, \omega)}{1 - A(\omega)G(\omega)R(\omega)}. \quad (30)$$

Note that the component (29) becomes unbounded as $t \rightarrow \infty$. In contrast, the rest of the solution (27) is bounded for large t . Thus, in this case the long-time behavior of the linear system is dominated by the single exponentially growing component (29), associated with the global instability of the closed-loop system.

2.4 Implications for closed-loop control of separation

In this section, we examine the implications of the above analysis for the control of flow separation by feedback enhancement of the instability wave field. In subsection 2.4.1, we discuss general considerations related to the above analysis and to observations from separation control by open-loop excitation of instability waves. In subsection 2.4.2, we discuss characteristics of the actuator transfer function $A(\omega)$, and the transfer function $G(\omega)$ for instability wave growth between the actuator and sensor, and the implications of these characteristics for feedback law design.

2.4.1 General considerations

The analysis of Section 3 has shown that proper choices of the feedback transfer function $r(t)$ (or $R(\omega)$) can produce a global system instability, or strong amplification of pre-existing instability waves. The crucial feature that must be considered is the behavior of the denominator,

$$[1 - A(\omega)G(\omega)R(\omega)],$$

which appears in the solutions (19) and (27) for the instability wave fields, and in the magnification factor (28). The denominator contains three transfer functions. These are the actuator transfer function $A(\omega)$, the transfer function $G(\omega)$ for instability wave growth between the actuator and downstream sensor, and the transfer function $R(\omega)$ for the feedback.

The transfer function $A(\omega)$ is determined by the type of actuator, and by the boundary layer characteristics at the location of the actuator. The transfer function $G(\omega)$ for the instability wave growth is determined by the boundary layer characteristics between the actuator and the downstream sensor. Our ability to tailor the characteristics of $A(\omega)$ and $G(\omega)$ is limited mainly to selection of the type of actuator and the relative locations of the actuator and downstream sensor. In contrast, we have complete freedom to choose the feedback transfer function $r(t)$ (or $R(\omega)$), subject only to the causality requirement and practical considerations related to its physical implementation.

Let's consider the feedback system characteristics that would be desirable for instability wave enhancement for separation control. Open-loop studies have shown that the most effective frequency for the forcing depends strongly on the flow situation. In general, it is most effective to excite instability waves that have the most potential for further growth with downstream distance.

Crudely speaking, the most unstable frequency for an inflectional boundary- or shear-layer profile scales as $\omega_{\max} \propto U/\delta$, where U is the speed of the stream and δ is the thickness of the vorticity layer. For similar values of U and δ , proximity to the wall produces a modest increase in the value of ω_{\max} . Thus, the value of ω_{\max} for an adverse pressure gradient boundary layer will be higher than the corresponding value for a shear layer far from the wall.

Typically, the boundary- or shear-layer thickness increases with downstream distance, leading to a shift of the unstable frequency band to lower frequencies with downstream distance. Therefore, it is usually most effective to excite waves within the unstable band at the location of the actuator, but at frequencies below that for the peak growth rate at this location, because these waves have the most potential for further growth with downstream distance.

Next consider a boundary layer that has fully separated, leading to a downstream flow that could be described as a shear layer in close proximity to a wall. The shear layer supports inflectional instabilities with relatively large growth rates, and it is possible to cause the shear layer to reattach by forcing within this unstable band. However, once an attached boundary layer state has been achieved, the most effective excitation frequency for keeping the boundary layer attached shifts to a higher frequency (Israel and Fasel, 2001). This observation from open-loop studies is consistent with the general picture presented above.

The above discussion suggests that it may be important to ‘allow the flow to choose the frequency’, rather than to impose a specific excitation frequency through the feedback system design. While a specific frequency chosen by the feedback system design could be very effective in controlling flow separation for some conditions, it might be much less effective in other conditions. A system in which the frequencies amplified by the feedback are based on the strongest naturally occurring instabilities would appear to have more promise for controlling flow separation over a wide range of conditions.

This leads to the suggestion that a feedback system which does not exhibit a global instability mode may be more attractive than one that has a global instability mode. If the linear system has a global instability mode, the frequency ω_j of the global mode would be expected to experience preferential amplification in the linear stage. However, the amplitude of this instability wave will not increase indefinitely as predicted by (20) and (29). At sufficiently large amplitudes, nonlinear effects become important in the unsteady fluid mechanics and the system will typically evolve to a limit cycle involving a saturated nonlinear instability wave. Further development depends on whether this saturated primary state is stable or unstable to secondary instabilities. This would likely depend on the location in parameter space. However, there are situations in which the development of a saturated nonlinear wave field inhibits the growth of disturbances at other frequencies. In such a situation, the presence of a global instability mode could be detrimental to our objective of enhancing the most amplified frequencies of the unforced flow.

A feedback system design that does not have a global instability mode, but has a large magnification factor $M(\omega)$ over a relatively wide frequency band, might be more effective in enhancing instability waves for separation control. The frequency band of interest would be the range of unstable frequencies, for all flow conditions of interest. If $M(\omega)$ is large but relatively flat over this frequency band, the dominant frequencies would be determined by the natural field incident on the sensor location $x = x_1$. In this situation, the excitation frequency would effectively be ‘chosen by the flow’. This might lead to a feedback system that was effective in enhancing instability wave motion, and thereby controlling flow separation, over a wide range of conditions.

The above discussion is speculative in nature. Further investigation is required in order to determine whether a feedback scheme with a global instability mode, or without such a mode, is preferable for separation control. Full assessment of the situation is complicated by the presence of nonlinear effects, which will clearly be important at high amplitudes, and by the fact that enhancement of instability waves is only an intermediate step to our actual goal of controlling flow separation.

A preliminary investigation of the characteristics of the transfer functions $A(\omega)$ and $G(\omega)$, and the implications of these transfer functions for design of a feedback transfer function $R(\omega)$, is

presented in the following subsection.

2.4.2 Characteristics of $A(\omega)$ and $G(\omega)$, and implications for $R(\omega)$

In order to design an appropriate feedback transfer function $R(\omega)$, information about the transfer functions $A(\omega)$ and $G(\omega)$ is required. Note that, in both (19) and (27), these functions appear only in the combination $A(\omega)G(\omega)$. It is the combined influence of actuator receptivity and subsequent instability wave growth that must be considered in designing the feedback law $R(\omega)$.

The actuator transfer function $A(\omega)$ could be determined analytically from triple-deck theory, semi-numerically from Orr–Sommerfeld theory, or extracted from CFD simulations. The following are observations concerning $A(\omega)$ that come from triple-deck theory (Choudhari and Kerschen, 1990) and references therein). The amplitude $|A(\omega)|$ is linearly proportional to the wall shear stress at the actuator location, suggesting that the forcing should be applied upstream of the point of flow separation. The variation of the phase $\text{Arg}[A(\omega)]$ with frequency is monotonic and relatively modest (a variation on the order of π) over the full frequency range of interest. Therefore, the phase of the total system response will be controlled mainly by the instability wave development ($G(\omega)$). As a caution concerning these conclusions, it should be noted that triple-deck theory applies to the generation of Tollmien–Schlichting waves, which are a viscous instability. The excitation of the inviscid instabilities of an inflectional profile is more relevant for the control of flow separation. The behavior in this case might be somewhat different than that found in the triple-deck analyses of T–S wave generation.

We can deduce some basic information concerning the behavior of $G(\omega)$ as follows. The phase speeds of instability waves vary only modestly across the range of unstable frequencies. Let's approximate the phase speed as $c_p = 0.5U$. We can then approximate the real part of the instability wavenumber as $\alpha_r \approx 2\omega/U$. Assuming a parallel mean flow, the expression (3) is applicable, so that

$$|G(\omega)| \approx \exp[-\alpha_i(x_1 - x_0)], \quad \text{Arg}[G(\omega)] \approx \gamma\omega, \quad (31)$$

where $\gamma = 2(x_1 - x_0)/U$. Note that the phase of the transfer function increases linearly with frequency, and the coefficient γ increases linearly with the sensor–actuator separation distance. This is an important consideration when designing the phase dependence of the feedback relation $R(\omega)$. The frequency dependence of $|G(\omega)|$ enters through α_i , which is negative in the unstable frequency range, say $\omega_l < \omega < \omega_u$. The magnitude $|G(\omega)|$ has a maximum at $\omega = \omega_{\max}$, and this maximum increases exponentially with increasing sensor–actuator separation distance. Thus, the transfer function $G(\omega)$ becomes increasingly frequency selective with increasing sensor–actuator separation distance. The peak of $|G(\omega)|$ corresponds to the frequency of the instability wave that has experienced the most growth in propagating from x_0 to x_1 .

Earlier, we suggested that a feedback law which produces a large magnification factor $M(\omega)$ over a wide frequency range might be most attractive. From the definition (28) of $M(\omega)$, we see that large values of $M(\omega)$ are obtained by choosing the feedback law such that the product $A(\omega)G(\omega)R(\omega)$ has a magnitude near one, and a phase near zero. Note that, when $|A(\omega)G(\omega)R(\omega)| \approx 1$, a change in the phase of this product from 0 to π would decrease $M(\omega)$ from a very large value to the value $M \approx 1/2$. In the latter case, the feedback has effectively suppressed rather than enhanced

the instability wave field. Thus, it is important to keep the phase of the product $A(\omega)G(\omega)R(\omega)$ near zero, or near an integer multiple of 2π . Note also, however, that the magnification factor $M(\omega)$ is quadratic in the deviation of the phase about $n2\pi$. Thus, small deviations from perfect phase matching in the feedback are not extremely detrimental. For example, a deviation from perfect phase matching of 0.3 rad (or 17°) produces only a 5% change in the real part of $A(\omega)G(\omega)R(\omega)$.

First, consider the implications of the characteristics of the transfer functions $A(\omega)$ and $G(\omega)$ for the phase of the feedback relation $R(\omega)$. We see that $G(\omega)$ has a strong phase variation with frequency, particularly for large values of the sensor-actuator separation distance. In contrast, the phase variation of $A(\omega)$ as a function of frequency is much milder. Let's examine the phase variation with frequency that would be required for the feedback law, in order to compensate for the phase variation with frequency of $G(\omega)$. One possibility would be to set

$$\text{Arg}[R(\omega)] = -\gamma\omega,$$

where $\gamma = 2(x_1 - x_0)/U$. To examine the corresponding behavior in the time domain, consider the case $|R(\omega)| = R_0$ where R_0 is a constant, so that

$$r(t) = (2\pi)^{-1} \int_{-\infty}^{\infty} R_0 e^{-i\gamma\omega} e^{-i\omega t} d\omega = R_0 \delta(t + \gamma).$$

Hence, this particular choice corresponds to a feedback signal that is shifted *forward* in time, by precisely the amount of time it has taken the instability wave to propagate from the actuator to the sensor. While this leads to an actuator output that is exactly in phase with the pre-existing field, the feedback law violates causality and therefore is not physically realizable. Mathematically, the difficulty could have been recognized in the transform plane by noting that $e^{-i\gamma\omega}$ grows exponentially in the complex ω -plane as $\text{Im}[\omega] \rightarrow +\infty$, whereas causality requires $R(\omega)$ to be analytic as $\text{Im}[\omega] \rightarrow +\infty$.

In order to obtain a physically realizable feedback law $R(\omega)$, the 'time delay' must be positive. At each frequency, the feedback law must introduce an effective time delay such that the actuator output is delayed by an integer number of periods relative to the pre-existing field, and is therefore 'in phase' with the pre-existing field. This can be achieved by setting

$$\text{Arg}[R(\omega)] = n2\pi - \gamma\omega - \text{Arg}[A(\omega)], \quad (32)$$

where the integer n is chosen large enough that $\text{Arg}[R(\omega)]$ is positive for the range of ω of interest. Note that the slope γ of this function increases linearly with the sensor-actuator separation distance, and the need to limit the range of frequencies considered in the feedback transfer function. The introduction of time delays in digital signal processing, by cyclic shifting of indices in the discrete Fourier transform, is discussed in Chapter 12 of Press et al. (1986).

Next, we examine the implications of the characteristics of the transfer functions $A(\omega)$ and $G(\omega)$ for determining the feedback amplitude $|R(\omega)|$. Again, $|G(\omega)|$ has strong frequency dependence, while the variation of $|A(\omega)|$ with frequency is much milder. As we have stated above, our objective is to enhance the naturally most amplified instability waves. The behavior of $|G(\omega)|$ appears quite attractive for this purpose. Note also that the variation of $|G(\omega)|$ with frequency

becomes stronger as the sensor-actuator spacing is increased. This may be a positive feature, since the flow itself becomes more frequency selective.

The influence of the feedback amplitude can be deduced by considering the magnification factor $M(\omega_0)$ for a fixed real frequency ω_0 , as a function of the feedback amplitude $|R(\omega_0)|$. Assume that the phase $\text{Arg}[A(\omega_0)G(\omega_0)R(\omega_0)]$ is held constant near an integer multiple of 2π . The magnification factor $M(\omega_0)$ then has a maximum at $|R(\omega_0)| = |A(\omega_0)G(\omega_0)|^{-1}$. In fact, when the argument of the product $A(\omega_0)G(\omega_0)R(\omega_0)$ is precisely $n2\pi$, $M(\omega_0)$ is singular for this value of $|R(\omega_0)|$. In applications, the maximum would be limited by the phase error or nonlinear effects or a combination of these.

To calculate the optimum value of the feedback amplitude $|R(\omega)|$, the value of $|G(\omega)|$ must be determined. Direct calculation of this factor from the stability properties of the flow is subject to inaccuracies, due to the exponential dependence of the amplitude $|G(\omega)|$ on the growth rate $-\alpha_i$. Thus, small changes in $-\alpha_i$ will translate to significant changes in $|G(\omega)|$, especially for larger values of sensor-actuator spacing. Effects due to variation of the mean flow with streamwise position x would also enter here. Thus, for an actual flow, it may be difficult to determine the appropriate value for the magnitude $|R(\omega)|$.

Therefore, it seems worthwhile to explore what happens if the feedback amplitude is increased beyond the value $|R(\omega)| = |A(\omega)G(\omega)|^{-1}$. From the definition (28) of $M(\omega)$, it would appear that increasing the feedback amplitude beyond this value is detrimental, leading to a decrease in the magnification factor. Intuitively however, it would seem that feeding back a stronger signal that was precisely in phase with the pre-existing field would *increase* the amplitude of the instability wave field. The correct explanation is that, by feeding back a stronger signal, we produce a temporally growing global instability that corresponds to a zero of the denominator in the upper half of the complex ω -plane. This would suggest that stronger forcing is not necessarily disadvantageous, and that in fact we may desire a situation in which we create a globally unstable mode, but with a frequency determined by the selectivity characteristic of $|G(\omega)|$. Note that the selectivity characteristic of $|G(\omega)|$ is enhanced by greater sensor-actuator spacings.

In summary, it appears that an increase in the sensor-actuator spacing has two effects, one advantageous and the other disadvantageous. The increase in the frequency selectivity of $|G(\omega)|$ that is produced by increasing the sensor-actuator spacing appears to be highly advantageous. However, when the sensor-actuator spacing is increased, $\text{Arg}[G(\omega)]$ becomes a more rapidly varying function of frequency, so that determination of the proper phase shift for the feedback transfer function becomes more difficult.

2.5 Schemes for Feedback Control of Flow Separation

In this section, two approaches for feedback control of flow separation are discussed. The first approach, which we refer to as 'phase control', builds directly on the preceding discussion and depends crucially on control of the phase of the actuator input signal. In this approach, we attempt to sense the time-dependent instability wave motion, and introduce direct feedback of a suitably conditioned time-dependent sensor signal in order to further destabilize the system, increasing the instability wave amplitude. This approach takes advantage of the pre-existing instability wave field

in a fairly optimum way. However, a difficulty is the need to determine the correct phase shift for the feedback relation, which may change significantly as a function of global flow conditions and the system state.

In the second approach, which we refer to as 'frequency/amplitude control', the frequency and amplitude of the forcing are controlled, but no attempt is made to control the phase of the actuator input. This approach has much in common with the open-loop approach to flow control. The main feature added here is a feedback scheme, in which the optimum frequency and amplitude of the forcing is determined based on feedback from downstream pressure measurements.

2.5.1 Phase control feedback scheme

The actual flows of interest involve separated boundary layers or boundary layers on the verge of separation. These flows are quite sensitive to small changes in the global conditions. Complications such as strong dependence of the mean flow on streamwise position x , and nonlinear effects on the instability wave behavior are also present. For such flows, it seems desirable to deduce required information concerning the feedback law directly from measured quantities.

The above discussion has identified the phase dependence as crucial to success in enhancing the instability wave field through feedback. One way to deduce the required phase shift for the feedback law is to examine the phase variation as a function of distance downstream from the actuator. This could be done using a series of wall pressure transducers, say at $x = x_k$, $k = 1, 2, \dots, n$. Due to the frequency selectivity of $G(\omega)$, the wall pressure spectra $P(x_k, \omega)$ at positions farther downstream should exhibit increasing amplitudes, and increasingly peaked spectral shapes. However, for a separated flow, the free-shear layer downstream of the separation point may move away from the wall with downstream distance, leading to an attenuation of the instability pressure field on the wall. In this case, sensors far downstream of the separation point may have lower values for the spectral peak associated with the instability wave field.

It seems reasonable to take the wall pressure sensor that has the maximum spectral peak as our source for the feedback signal. Denote the sensor corresponding to the maximum spectral peak as k_{\max} , and the peak frequency in the spectrum $P(x_{k_{\max}}, \omega)$ as ω_{\max} . We need to deduce the proper phase for $R(\omega)$ in order to enhance this spectral peak.

The first step is to extrapolate the phase variation for the dominant component back upstream. The relative phase for the frequency $\omega = \omega_{\max}$ at each of the sensor locations upstream of $x_{k_{\max}}$ can be determined from the arguments of the wall pressure cross spectra, $C_{k, k_{\max}}(\omega_{\max})$, for $k < k_{\max}$. Note that the use of $P(x_{k_{\max}}, \omega)$ in these cross spectra should improve the fidelity of the extraction, since $P(x_{k_{\max}}, \omega)$ has a strong peak at ω_{\max} . With the phase dependence defined on the set of points x_k , $k = 1, 2, \dots, k_{\max}$, it should be possible to extract the phase of this component to the actuator location x_0 , and thereby determine the phase of $G(\omega_{\max})$.

The correct phase for the feedback transfer function is then given by

$$\text{Arg}[R(\omega_{\max})] = n2\pi - \text{Arg}[G(\omega_{\max})] - \text{Arg}[A(\omega_{\max})], \quad (33)$$

where n is the smallest positive integer that leads to a positive value for $\text{Arg}[R(\omega_{\max})]$. Thus, the phase of $A(\omega_{\max})$ must also be determined. Results from receptivity calculations (triple-deck,

Orr–Sommerfeld, or CFD) may be sufficiently accurate for this purpose. Alternatively, it may be possible to ‘interrogate’ the actuator and the flow in some way. For example, we could force the actuator with a short wavetrain of center frequency ω_{\max} . Cross correlations such as those discussed above, but using the actuator input as the reference field, could then be used to deduce the phase of $A(\omega_{\max})$ (and also $G(\omega_{\max})$, if desired).

Next, we must consider the appropriate amplitude for the feedback, $|R(\omega_{\max})|$. A good starting point would seem to be the value

$$|R(\omega_{\max})| = |A(\omega_{\max})G(\omega_{\max})|^{-1}, \quad (34)$$

discussed in the previous subsection. Here, we need the magnitudes $|G(\omega_{\max})|$ and $|A(\omega_{\max})|$. The value of $|G(\omega_{\max})|$ can be determined by extrapolation of the results from the cross spectra $C_{k,k_{\max}}(\omega_{\max})$ discussed above, but using the magnitudes rather than the phases. Again, it may be sufficient to determine $|A(\omega_{\max})|$ from receptivity calculations, or it could be extracted using an approach similar to that discussed in the previous paragraph.

Finally, we consider specific forms of the feedback transfer function. One of the simplest functions would be

$$r(t) = K\delta(t - \tau), \quad \text{or} \quad R(\omega) = Ke^{i\omega\tau} \quad (35)$$

where we set $|R(\omega_{\max})| = K$ and the time delay τ is chosen as the smallest positive number for which

$$\text{Arg}[A(\omega_{\max})G(\omega_{\max})R(\omega_{\max})] = n2\pi. \quad (36)$$

A somewhat more sophisticated approach to the feedback transfer function would be to make the time delay (or phase shift) frequency dependent, in order to account for the local variation of $\text{Arg}[G(\omega)]$ in the vicinity of $\omega = \omega_{\max}$. The local variation of $\text{Arg}[G(\omega)]$ in the vicinity of ω_{\max} could be determined by applying the scheme discussed above to frequencies slightly above and below ω_{\max} . In comparison to the variation of $\text{Arg}[G(\omega)]$ with frequency, the variation of $\text{Arg}[A(\omega)]$ is much less significant and can probably be ignored. Since the phase matching is the most crucial aspect of the instability enhancement scheme, it would probably be adequate to adjust only the phase of $R(\omega)$, and utilize an amplitude $|R(\omega_{\max})|$ that is independent of frequency. However, it might be beneficial to remove extraneous low and high frequency components, by introducing a global window function on the amplitude $|R(\omega)|$.

In Section 2.7.1, CFD simulations are used to examine the performance of a simple Phase Control feedback scheme, which employs a time-delayed proportional feedback amplitude that is independent of frequency. We find that the Phase Control feedback scheme is able to achieve reductions in separation bubble length which are unattainable with open loop forcing at any frequency or amplitude we tested.

2.5.2 Frequency/Amplitude control feedback scheme

A somewhat less ambitious approach to feedback enhancement of active-flow separation control is to develop a feedback system that controls only the frequency and amplitude of the actuator input, but not the phase. This is a natural extension of the previous work on open-loop flow control,

and builds on the success and robustness of this previous work. In open-loop flow control, the frequency and amplitude of the forcing are determined off line, often on the basis of detailed flow field measurements and stability calculations, or of extensive experimental parametric studies. We envision a scheme in which the frequency and amplitude of the forcing are determined in real time by an adaptive control method, based on downstream surface pressure measurements as described in the following paragraph.

Pressure sensors on the suction surface of the wing would be used to measure both the mean pressure and the spectrum of the time-dependent component. The occurrence of flow separation on the suction surface of a wing would be detected by a sudden rise in mean pressure on the surface. A sudden rise in the amplitude of the unsteady component would be a further indication of flow separation. When separation was detected, the actuator would be driven with a time-harmonic signal to excite strong instability waves. The initial frequency of the forcing would be determined by an algorithm that considered the flow speed and flight conditions in order to provide a reasonable estimate of the unstable frequency band.

The response of the flow field to this initial forcing frequency, and also to perturbations in frequency about the initial frequency, would be measured by the downstream pressure sensors. Again, both the mean pressure levels and the spectra of the unsteady components provide useful information. The mean pressure levels indicate the lift force generated by the wing, while the spectra of the unsteady components indicate the frequencies that are most highly amplified (in other words, the frequencies that the flow is most receptive to). Based on the response to perturbations in the forcing frequency, the forcing frequency would be adjusted to maximize desirable characteristics of the downstream field. Similarly, the response to perturbations in the forcing amplitude would be used to determine the optimum forcing amplitude.

Hence, this alternative approach uses feedback from downstream sensors to determine the optimum frequency and amplitude for the actuator input, but makes no attempt to control the phase of the actuator input. Therefore, as in open-loop flow control, the unsteady field produced by the actuator must overpower the pre-existing field, rather than combining constructively with it. However, since we are exciting the natural instabilities of the system, significant instability wave amplitudes can be produced by relatively small input signals. Effectively, the instability extracts energy from the mean flow, so that the energy supplied by the actuator is relatively small.

The strong instability wave motion that produces flow reattachment involves nonlinear interactions between instabilities of different frequencies. Thus, it may be beneficial to include both a primary frequency and its subharmonic in the actuator input. Again, the frequencies, amplitudes and relative phases of the two components could be determined and adjusted reactively based on measurements of the pressure field on the downstream surface.

It is important to note that this approach significantly reduces the 'frequency response' requirements for the control system, relative to the Phase Control feedback scheme. While the pressure sensors and associated spectral processing equipment must resolve the relatively high frequencies of the instability waves, adjustments to the frequency and amplitude of the forcing can be carried out on a time scale that is one or even several orders of magnitude longer than the period of the forcing frequency.

The general approach of controlling the frequency and/or amplitude of the actuator input (but

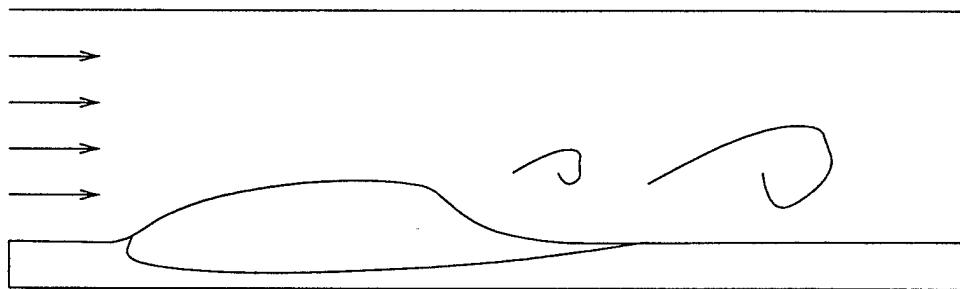


Figure 2.1: Experimental geometry of Seifert and Pack (1999).

not the phase), based on a feedback quantity related to the field, can be extended to achieve a variety of flow behaviors. An example based on CFD simulations is presented in subsection 2.7.2, where the the actuator input amplitude is determined by a feedback control system in order to achieve a specified ramps-up, hold, then ramps down temporal variation in lift coefficient.

2.6 CFD simulations of reactive flow control

Computational Fluid Dynamic (CFD) simulations were utilized to investigate the feedback control schemes discussed above. The simulations utilize the code of Israel and Fasel (2001), who investigated active control of flow separation by open-loop forcing. For the simulations of feedback control schemes, the boundary conditions were modified to incorporate the closed-loop controller.

The geometry chosen for these simulations is the ‘hump’ of Seifert and Pack (1999), shown in Fig. 2.1. The geometry consists of the upper surface of a modified Glauert Glas II airfoil, mounted in the side wall of a wind tunnel, with the leading and trailing edges feathered. This configuration was specifically designed for CFD validation of Active Flow Control (AFC), and it has been extensively investigated. Open loop AFC data is available from both experiments (Seifert and Pack, 1999, 2000; Pack and Seifert, 2000) and simulations (Israel and Fasel, 2001, 2002), which makes it ideal for comparing the effectiveness of open and closed loop control strategies.

The numerical method of Israel & Fasel solves the compressible Navier–Stokes equations in conservative form, on an orthogonal body-fitted grid with stretching functions to concentrate points near the surface of the airfoil and its downstream wake. A buffer region is used to minimize the upstream feedback of pressure disturbances from the outflow boundary treatment. The viscous no-slip condition is applied on the lower wall of the wind tunnel (i.e. the upper surface of the airfoil), while a slip boundary condition is applied on the upper wall of the wind tunnel. A high accuracy finite-difference method is employed, using split differences which sum to fourth-order accuracy in space, and fourth-order Runge-Kutta integration in time. The code is parallelized using domain decomposition with the Message Passing Interface (MPI).

Due to the CFL restriction for a compressible code running at low Mach number, the timestep required by the CFD code is much smaller than that required by the closed-loop controllers. Consequently, the controller ODEs were integrated using a forward Euler time integrator. The one exception was for the Pole Placement and LQG controllers discussed in Section 2.7, for which

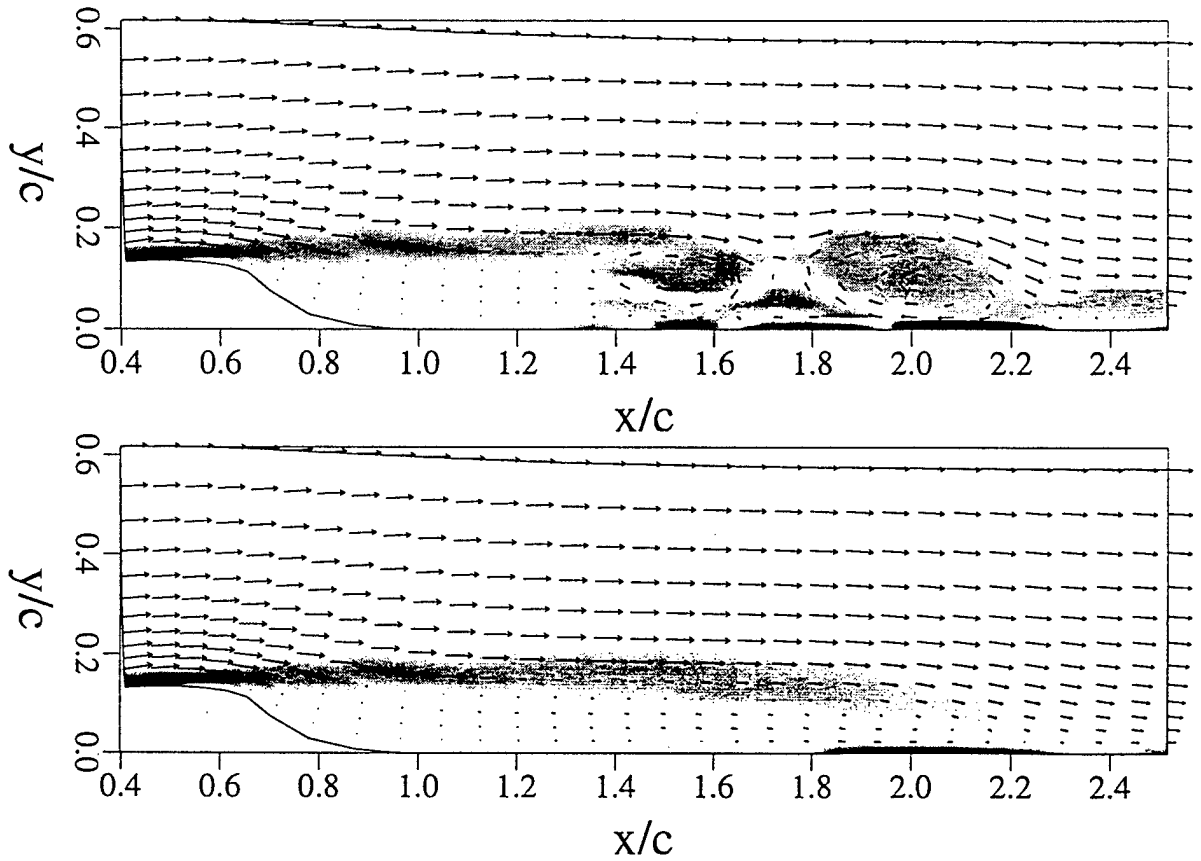


Figure 2.2: Contours of vorticity and velocity vectors for the unforced flow: instantaneous (top) and time averaged (bottom). $Re_c = 10^4$, $Ma = 0.25$. (Israel and Fasel, 2001)

the A matrix has one very unstable eigenvalue, and therefore a backward Euler integrator was employed.

The modified Glauert Glas II airfoil has a fairly thick profile, with a relatively sharp corner on the upper surface at approximately $x/c = 0.6$, followed by a concave ramp to the trailing edge ($x/c = 1.0$). For this profile, the flow will separate at the sharp corner if no flow control is applied. Numerical simulations (Israel and Fasel, 2001) have been performed to obtain data for laminar flows ($Re_c = 10^4$, $Ma = 0.25 - 0.6$). Instantaneous and time-averaged vorticity contours and velocity vectors for a typical case without forcing are shown in Fig. 2.2. The unforced flow contains a long separation bubble, with strong unsteady vortices forming at about $x/c = 1.4$, and reattachment of the mean flow at $x/c = 2.4$.

Numerical simulations of open-loop forcing of the laminar flow were also carried out. The amplitude of the forcing is expressed in terms of the oscillatory blowing momentum coefficient, $\langle c_\mu \rangle = \langle \rho V^2 h \rangle / \rho_\infty U_\infty^2 c$, V is the oscillatory blowing amplitude, h is the forcing slot width and c is the chord of the hypothetical airfoil. Significant reductions in the separation length were obtained with forcing of the order $\langle c_\mu \rangle = 0.05\%$. The most effective frequency for the open-

loop forcing was slightly higher than the natural shedding frequency of the unforced case. For higher forcing frequencies, and $\langle c_\mu \rangle \sim 0.01\%$, vortex merging was observed.

2.7 Reduced Order Modeling of Actuator/Flow system

In order to apply feedback control law design methods to the active flow control problem, a model for the frequency response of the actuator/flow system is required. Specifically, from the analysis of Section 2.3 (see Eq. 9), the wall pressure field $P(x_1, \omega)$ at a downstream sensor location x_1 is related to the actuator velocity $V_A(\omega)$ by the product $A(\omega)G(\omega)$, where $A(\omega)$ is the transfer function for the actuator and $G(\omega)$ is the transfer function for the instability wave development from the actuator to the location x_1 of the downstream wall pressure sensor.

The Bode diagram for the combined transfer function $A(\omega)G(\omega)$ was determined from frequency response data generated using CFD simulations ((Israel and Fasel, 2001). Input frequencies ranged approximately from one decade below to one decade above the natural shedding frequency. Outside this frequency range, the flow was not responsive to forcing. Several models for the transfer function were fit to this data, and it was found that the system could be represented reasonably well by a sixth-order model. The sixth-order model for the transfer function is compared to the CFD data in Fig. 2.3.

The equivalent state-space model in a canonical form was then determined for implementation in CFD simulations of closed-loop control. The target chosen for the feedback control system was specified values of the mean and first harmonic components of the downstream pressure field at $x/c = 0.8$, with levels chosen consistent with the results from open-loop forcing. Given a linear system model, one can apply any linear design technique. We tried two well-known methods: (1) pole placement using full state feedback and a Luenberger observer, and (2) linear quadratic Gaussian (LQG) control, which is a steady-state, optimal, linear quadratic regulator (LQR) and a steady-state Kalman filter.

The appeal of the pole placement method is that it is very intuitive from a design point of view. Specification of desired eigenvalues is intuitive for non-control-specialists. Our sixth-order model has five stable eigenvalues and one unstable eigenvalue. One can choose five of the closed-loop eigenvalues to be near the stable open-loop eigenvalues. This seems particularly appropriate given that one does not expect to be able to change significantly the eigenvalues associated with natural vortex shedding. The remaining eigenvalue is chosen to be stable. This specifies six of the twelve closed-loop eigenvalues. (The Luenberger observer has an order equal to the order of the system.) The feedback gain matrix is determined by these six eigenvalues. The remaining six eigenvalues are chosen to be five to ten times faster than the first six eigenvalues. The observer gain matrix is determined by these six eigenvalues.

The appeal of the LQG method is that the state error weighting matrix Q and the input magnitude weighting matrix R can be chosen to trade off output error and control effort. Unfortunately, design of the Kalman filter is difficult in that it requires estimates of error spectral density matrices. In the single-input single-output case considered here this is greatly simplified, because the spectral density matrices are scalars. Even so, determining appropriate orders of magnitude is difficult.

Controllers were designed using each method and were evaluated using CFD simulations. For

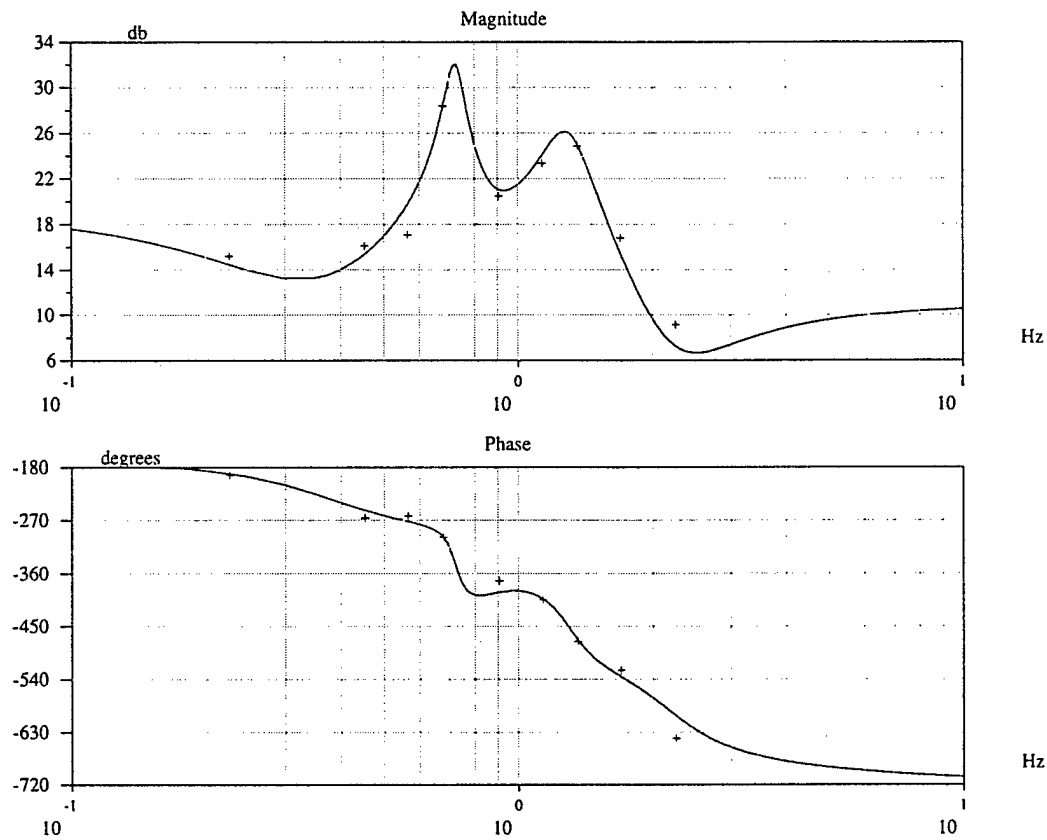


Figure 2.3: Bode diagram showing the frequency response of the pressure at 80% chord and $c_\mu \geq 2 \times 10^{-5}$. (+) Open loop data, (—) sixth-order model transfer function

both methods the controller requested unrealistically high forcing velocities, higher than predicted by the linear model. There are a number of possible explanations for this behavior. The transfer function model fitted to the frequency response data has as many zeros as poles. Such a model is 'proper', but not 'strictly proper', and will have discontinuous step responses, which is certainly not true of the actual flow system. Note also that the sixth-order model exhibits some deviations from the CFD data in the vicinity of the maximum response, both for the amplitude and the phase. An improvement in the fidelity of the system model could lead to improved behavior for the control system. Finally, specification of the mean pressure level at the downstream location as a target for the control system raises questions concerning the adequacy of linear modeling, since it is the mixing and entrainment produced by the instability wave (or vortex structures) that is responsible for the modification of the mean pressure level.

Proper Orthogonal Decomposition (POD) offers an alternative for reduced order modeling of the flow system. POD is expected to be most effective when the dynamics of the system is controlled by a small number of modes. For example, POD has proved quite useful in examining the nonlinear three-dimensional breakdown of a laminar boundary layer flow (see Rempfer and

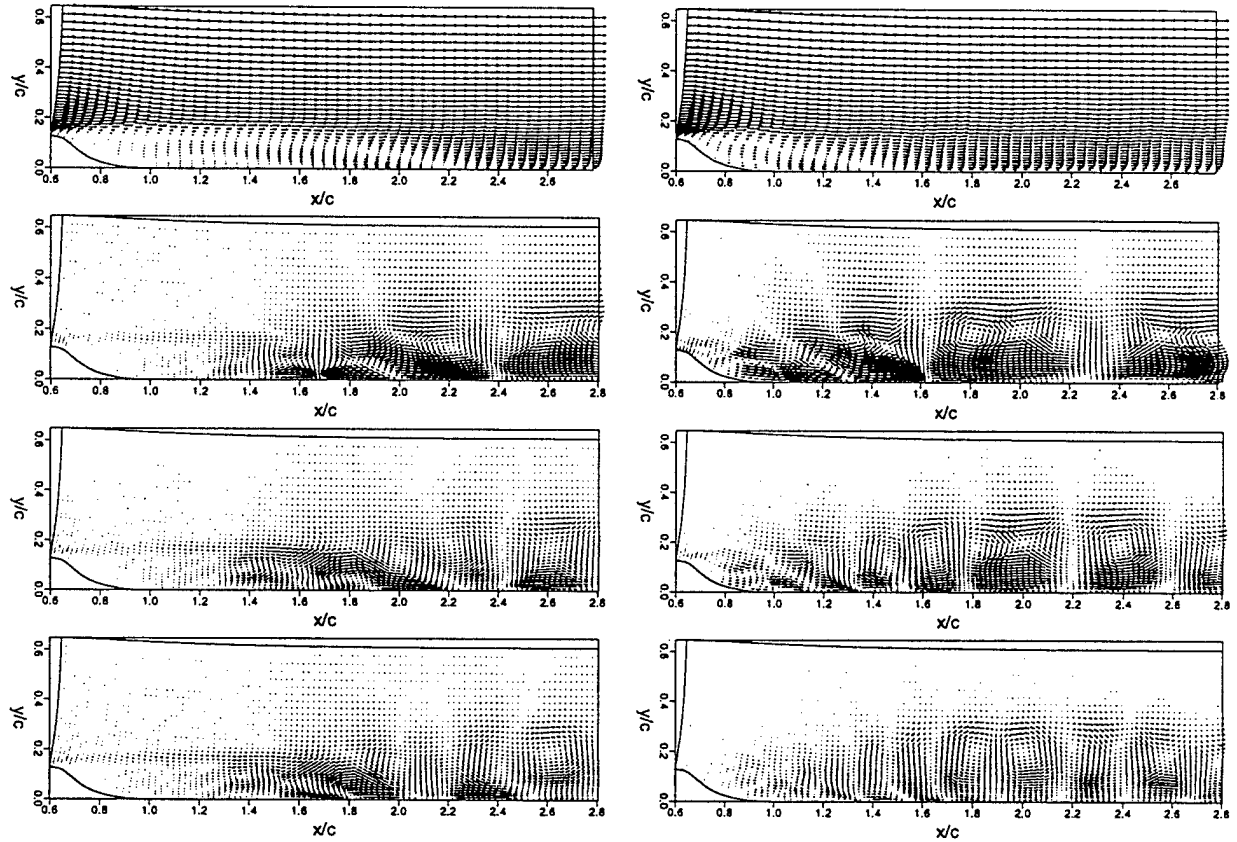


Figure 2.4: The first four POD modes for the unforced (left) and open loop forced (right) cases.

Fasel 1994a, 1994b). POD has also been used with success in certain controls related applications. For example, Gillies (1998) used a low-order POD representation coupled with (empirical) neural network modeling to control the behavior of the wake of a circular cylinder at low Reynolds numbers.

We have investigated the use of POD for describing our separated flow system by applying the technique to time-dependent CFD data. Results from the POD analysis of two cases are presented in Fig. 2.4. The POD modes for the uncontrolled case are shown in the left column, while the corresponding modes in the presence of open-loop control are shown in the right column. The first POD mode is dominated by the mean flow. Note the significant reduction in the size of the separated region when open-loop control is applied. The size of the 'large structures' seen in the second mode is characteristic of the spacing between the vortices in the actual flow field. Downstream of the flow reattachment point ($x/c = 2.2$ for the uncontrolled case, $x/c = 1.2$ with feedback control), we can see that the POD modes are qualitatively similar for the two cases. However, in the separated region farther upstream which is of crucial interest, the modes are qualitatively different for the two cases.

The use of POD modes for a reduced order model of the flow field involves truncation of the

modal expansion at low order. The fact that there are significant differences between the low-order modes for the cases with no control and with open-loop control presents a fundamental difficulty in utilizing POD modes for a reduced order model. One approach to dealing with this problem would be to construct the POD modes for a mixture of flow field snapshots from the two cases. The lowest modes would then be an average of sorts, intermediate between the flows for the unforced and forced cases. However, the value of this representation is not clear. Note also that the POD modes are based on maximizing the flow kinetic energy. It is not evident that kinetic energy is the most important physical characteristic of the flow field in the present application, since the free-stream flow contains most of the kinetic energy, while the most important dynamics are associated with the lower speed flow near the airfoil surface.

One feature which the POD analysis confirms, however, is that the most important dynamical feature of the flow is the instability waves (or large-scale structures) in the separated region. The analysis of the previous sections addressed the issue of using feedback to enhance the instability wave amplitudes. Note that this is a non-standard control paradigm—control theory is typically aimed at minimizing some disturbance quantity, rather than maximizing it. However, the linear theory developed in previous sections of this report provides very useful guidance for design of a feedback law to enhance instability wave amplitudes. Thus, it seems reasonable to take advantage of the guidance from linear theory in devising feedback schemes to enhance the instability wave amplitudes. Note that this strategy relies on the flow dynamics to set a saturation level for the amplitude of the large structures.

In the following sections, CFD simulations are used to investigate the suppression of flow separation using the Phase Control and Frequency/Amplitude Control feedback schemes.

2.7.1 Phase Control Feedback Scheme Simulations

We first investigate the use of a phase control feedback scheme, in which the output velocity $v_A(t)$ of the actuator is determined by applying a feedback transfer function $R(\omega)$ to the signal $p(x_1, t)$ from a downstream wall pressure sensor. The sensor signal is first bandpass filtered ($p(x_1, t) \rightarrow \bar{p}(x_1, t)$) to remove the mean value (which is unknown *a priori*) and to restrict frequencies to a well-modeled band. We use a standard second order filter of the form

$$\begin{aligned} \dot{x} &= Ax + Bp \\ \bar{p} &= Cx + Dp, \end{aligned}$$

where p is the unfiltered pressure, and x is an internal state variable for the filter. The coefficients matrices are derived using Matlab to impose the desired low and high frequency cutoffs. For the filter used in this work, $D = 0$.

Our objective is to enhance the naturally occurring instability wave field, in order to increase the mixing and entrainment and suppress flow separation. The simplest possible feedback is a variable gain proportional controller,

$$v_A = K\bar{p}, \tag{37}$$

where the gain K could be adjusted to control the degree of suppression of flow separation. A more effective feedback scheme might be achieved by choosing a more complex feedback function

which adjusts the phase relationship between the input and output. This could be done by adding time derivative terms, i.e.,

$$v_A = K_1 \bar{p} + K_2 \dot{\bar{p}} + K_3 \ddot{\bar{p}} + \dots \quad (38)$$

This would require storing a short time sequence of pressure measurements so that digital calculation of the time derivatives could be obtained. A significant drawback of this approach is that the derivative operator amplifies high frequency components, so that the signal produced needs to be strongly filtered to remove high frequency noise. Another approach would be to use a higher order filter operator and specify additional constraints on the filter amplitude and phase relation. Preliminary attempts to derive such filters in Matlab showed that the high order filters tend to have very stiff transfer functions, and are therefore not well behaved for off design frequencies.

A third approach to adjusting the phase of the feedback signal is to add a constant time lag τ to the feedback loop, τ is chosen according to (36). The relationships (14) and (35) then lead to

$$v_A(t) = K \bar{p}(t - \tau). \quad (39)$$

This was the approach used in our CFD simulations.

We first applied the feedback law (39) for $\tau = 0$ and a range of values for the gain, K . Figure 2.5 shows the reattachment length plotted against the gain for simulations with the feedback pressure sensor at two different locations, $x/c = 0.8$ and 1.4 . For the sensor location at $x/c = 0.8$, we observe that the reattachment length depends strongly on the feedback gain K , decreasing with increasing gain. This is consistent with our expectations concerning the effect of the gain ($K = |R(\omega)|$) on the magnification of instability wave amplitudes (see (28)). For the cases shown here, $K < |A(\omega)G(\omega)|^{-1}$. Due to the CFL numerical stability constraint associated with the forcing slot, it was not practical to perform simulations with $K > 0.48$.

Much shorter reattachment lengths are obtained for feedback from the sensor at $x/c = 1.4$, even at relatively small values of the gain. The fact that lower gains are required for sensor locations farther downstream is consistent with our expectations, since the total feedback amplification is a combination of the amplification due to the gain parameter, K , and that due to the natural growth of the instability, $G(\omega)$, the latter of which is larger for a sensor placed farther downstream. Physically this can be understood by noting that a sensor sufficiently far downstream detects the pressure footprints of the shed vortices, whereas a sensor located farther upstream detects only the much weaker instability wave precursor to the shed vortices.

Further insight into the physical behavior can be obtained by examining the spectra of the forcing signal $v_A(t)$, which are presented in Fig. 2.6. Results for the sensor location $x/c = 0.8$ are shown on the left, while the corresponding results for the sensor location $x/c = 1.4$ are shown on the right.

For $x/c = 0.8$, the spectra for the three lowest values of gain are relatively broadband, while the spectra for $K = 0.36$ and 0.48 are strongly peaked, indicating a locking onto strongly coherent vortex shedding. Note from Fig. 2.5 that a substantial decrease in the separation length occurs for these two latter values of gain.

In contrast, for the pressure sensor at $x/c = 1.4$, the spectra are strongly peaked for all values of the gain, indicating that the system is locking onto strongly coherent vortex shedding even at

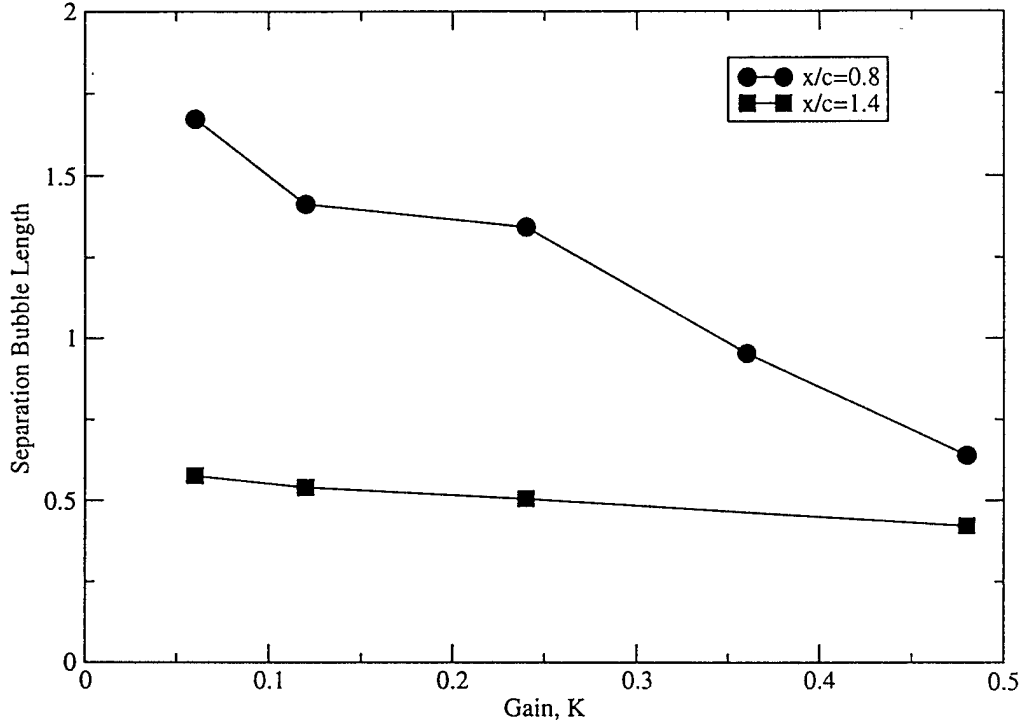


Figure 2.5: Reattachment length as a function of the feedback gain, K , for two different locations of the pressure sensor.

low values of K . For this sensor location, the effectiveness of the feedback at the lower values of gain is enhanced by the additional natural amplification of the feedback signal due to the increased instability wave growth $G(\omega)$. Note that, for $x/c = 1.4$, the actual forcing amplitudes $V_A(\omega)$ are quite high even for small values of K . In contrast, the forcing amplitudes $V_A(\omega)$ at small values of gain were much lower for the sensor location $x/c = 0.8$.

It is interesting to compare the amplitudes of the higher harmonics in $V_A(\omega)$ to the amplitude of the fundamental, for cases of strongly coherent vortex shedding. For the sensor location $x/c = 1.4$, the higher harmonics have amplitudes close to the amplitude for the fundamental frequency, while for $x/c = 0.8$, the higher harmonics in $V_A(\omega)$ are weaker than the fundamental frequency. The larger relative amplitudes of the higher harmonics for $x/c = 1.4$ arises from nonlinearities associated with the roll-up process by which the concentrated vortices are formed.

The additional nonlinearity which occurs at higher forcing amplitudes also provides an explanation for the observation that the reattachment length is a stronger function of gain K for the

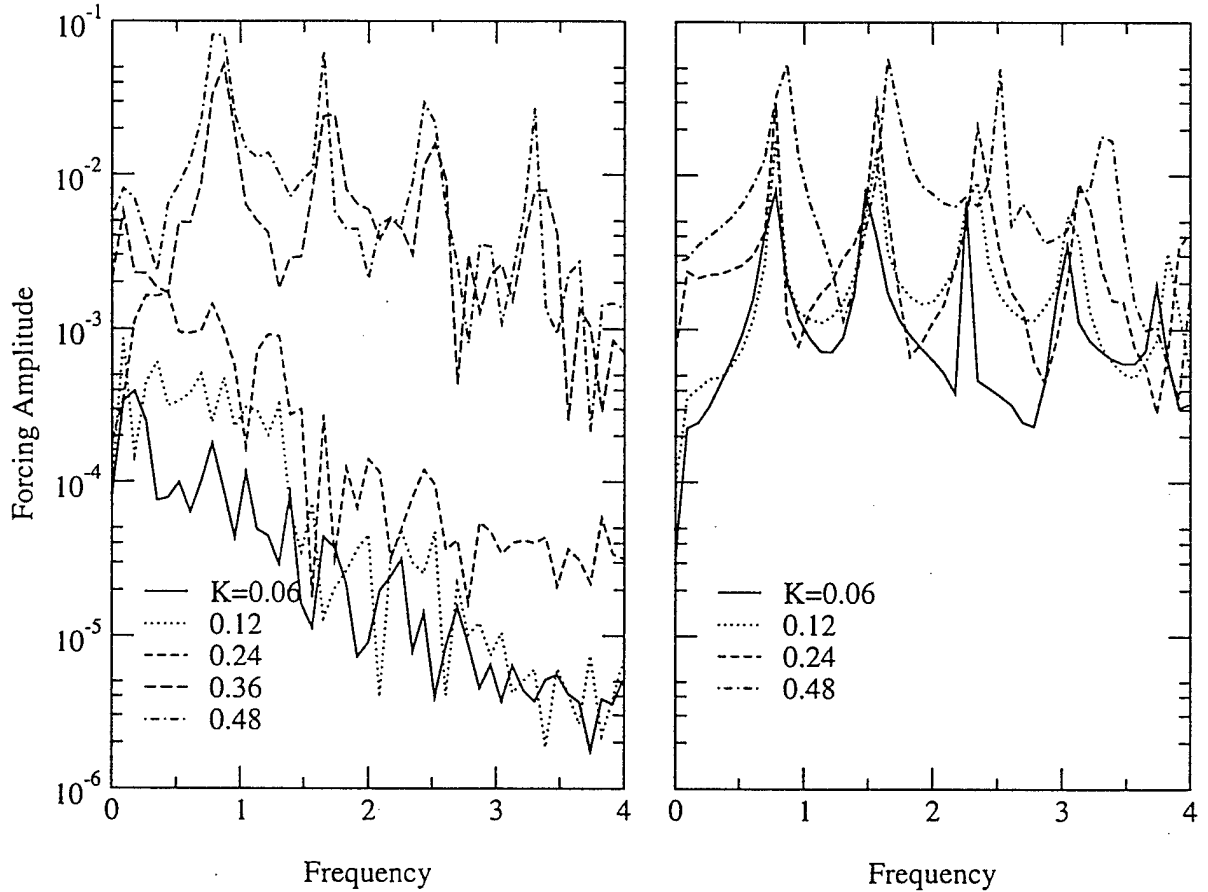


Figure 2.6: Spectra of the proportional feedback forcing with pressure sensor at $x/c = 0.8$ (left) and $x/c = 1.4$ (right).

sensor location $x/c = 0.8$ than for the sensor location $x/c = 1.4$ (see Fig. 2.5). For $x/c = 1.4$, the forcing amplitudes are high enough that nonlinear saturation sets in quite early in the vortex roll-up process. Essentially, even at $K = 0.06$ the actuator forcing amplitude is large enough to excite strongly coherent vortices, leading to a substantial reduction in the separation length. At higher gains (or forcing amplitudes), nonlinear saturation sets in earlier in the vortex roll-up process and the further decreases in reattachment length are relatively modest. This effect has also been observed in open-loop active control studies. Effective control of flow separation requires forcing amplitudes that are sufficient to produce strongly coherent vortices. However, once strongly coherent vortex motion is obtained, further increases in forcing amplitude produce only modest improvements—the effect of the increased initial amplitudes of the instability waves is negated to a significant extent by the earlier onset of nonlinear saturation.

Next, consider the behavior of the control system as a function of the feedback sensor location, for a fixed feedback time delay $\tau = 0$. Changing the location of the feedback sensor has two effects. First, for a sensor location farther downstream, the natural instability mechanisms of the

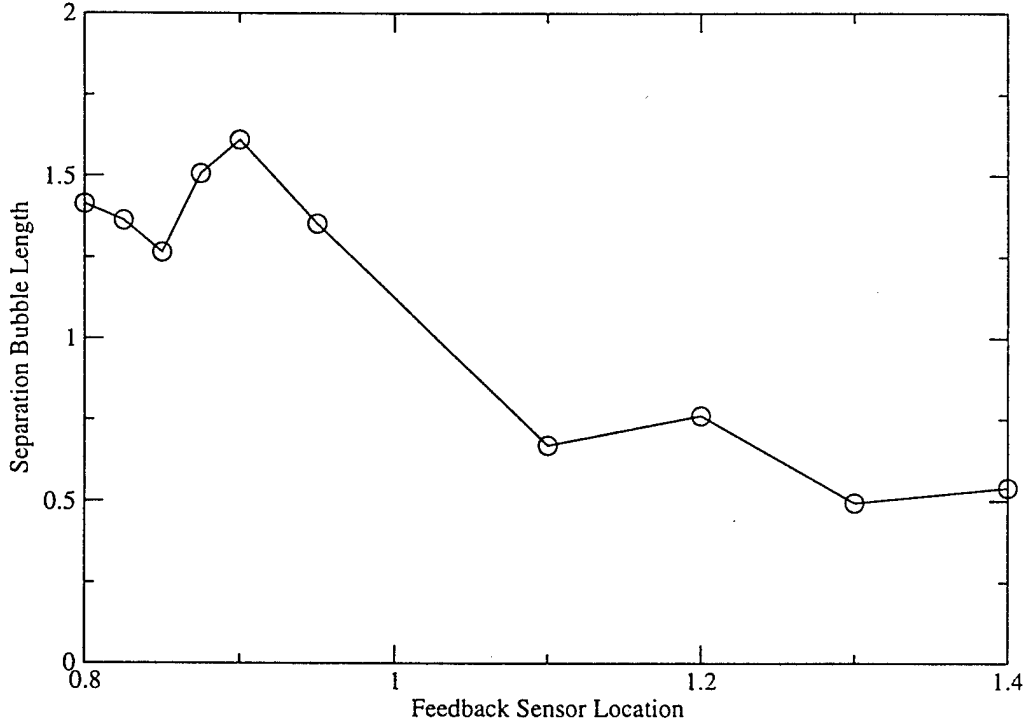


Figure 2.7: Reattachment length as a function of sensor location.

flow have had a greater distance over which to amplify the disturbance waves. Second, the phase relationship between the flow field at the actuator and at the sensor goes through one cycle for every wavelength that the sensor is moved downstream.

Figure 2.7 shows the separation length plotted against the feedback sensor location, for a constant gain $K = 0.12$. Distinctly different behavior is observed for $x/c < 1.0$ and $x/c > 1.0$. As expected, the controller is more effective when it is placed further downstream (for a fixed value of K). However, in both the upstream and downstream regions (say, $0.8 \leq x/c \leq 0.95$ and $1.1 \leq x/c \leq 1.4$), the separation length exhibits an oscillatory dependence on feedback sensor location. The oscillatory dependence appears to be related to the effects of sensor location on the phase of the feedback to the actuator.

Next consider the behavior of the control system as a function of the feedback time delay, τ . The feedback law (39) was implemented in the CFD code by the addition of a ring buffer to store the intermediate time data. Typical results can be seen in figure 2.8. As expected, the reattachment length is an oscillatory function of the time lag τ . The separation bubble is shortened by a time lag

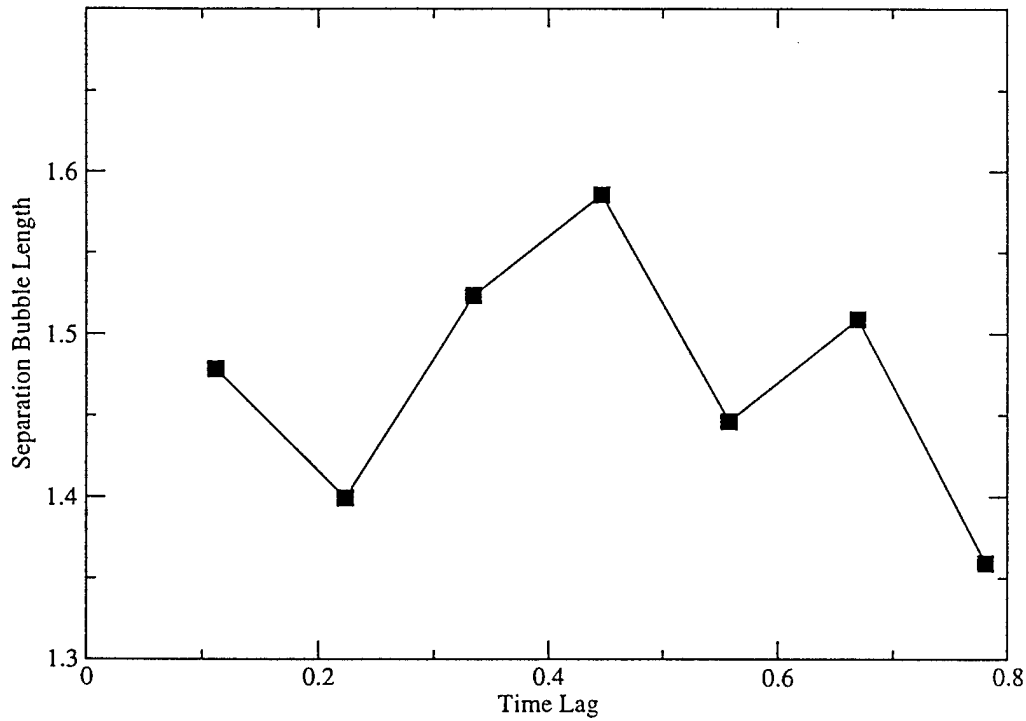


Figure 2.8: Reattachment length as a function of time lag.

that leads to reinforcement of the naturally occurring instability waves (or vortex structures). The behavior is not perfectly sinusoidal because there are nonlinear interactions that provide multiple frequency paths to exciting the vortex structures, and the phase speeds of the instability waves are a function of frequency.

The above discussion has focused on the influences of the feedback gain and the time lag on the performance of the closed-loop system in reducing flow separation. It is also important to examine the relative efficiency of the different closed-loop systems. To do this, we need to consider the magnitude of the oscillatory blowing momentum coefficient, $\langle c_\mu \rangle = \langle \rho V^2 h \rangle / \rho_\infty U_\infty^2 c$. In Fig. 2.9, the results from Fig. 2.5 are replotted to show the reattachment length as a function of $\langle c_\mu \rangle$. Each data point is annotated with the corresponding value of the feedback gain, K . For reference, the curve for open loop forcing at the natural shedding frequency is also shown. We can see that with the pressure feedback sensor located at $x/c = 0.8$, the efficiency for the closed-loop controller is somewhat lower than the corresponding results for open loop forcing. This is not surprising, for two reasons. First, no attempt has been made to optimize the time

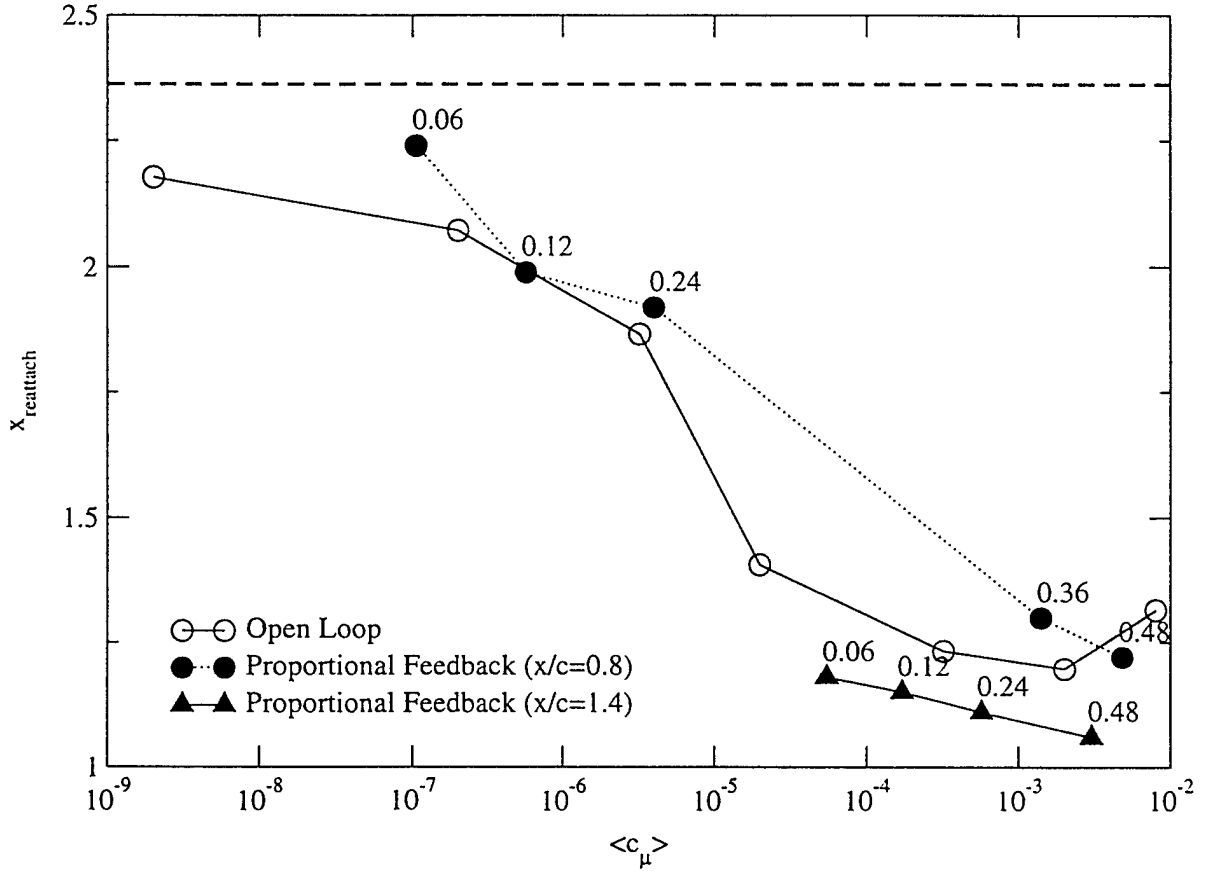


Figure 2.9: Reattachment length versus momentum coefficient for open and closed loop forcing. Annotations are gain values.

lag and gain in these results. In contrast, the forcing frequency for the open-loop control has been optimized. Second, the downstream pressure field, and hence the feedback to the actuator, contains extraneous random elements that raise the value of $\langle c_\mu \rangle$ without contributing to the coherent vortex structure that is responsible for suppressing the flow separation.

For $x/c = 1.4$, we see that all the closed-loop data corresponds to $\langle c_\mu \rangle > 10^{-4}$, despite the fact that gains as small as $K = 0.06$ were considered. This is consistent with our earlier discussion concerning the behavior of the closed-loop system and the importance of the instability wave growth function $G(\omega)$. It is interesting to note that the closed-loop data for $x/c = 1.4$ lies slightly below the corresponding data. Thus, in this case the feedback control has an efficiency which is slightly better than that for open-loop control, despite the fact that the closed-loop control system has not been optimized. This suggests that closed-loop feedback control may have considerable promise.

In Fig. 2.10, the results for separation length as a function of sensor location, for fixed gain $K = 0.12$, that were presented in Fig. 2.7 are replotted to show separation length as a function

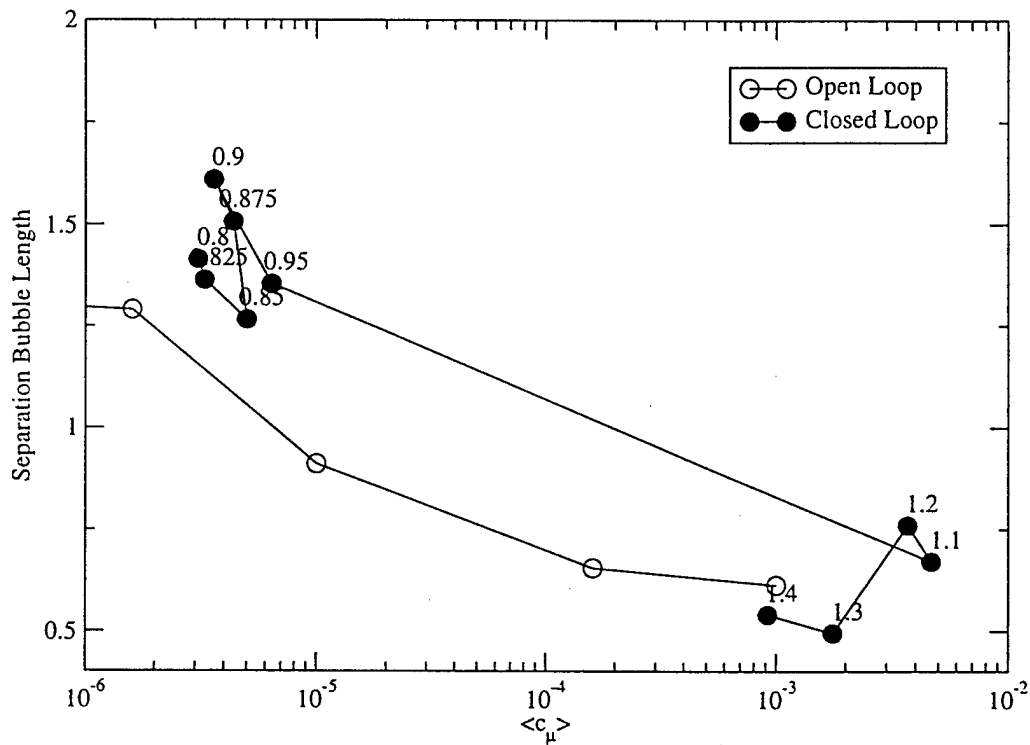


Figure 2.10: Reattachment length versus momentum coefficient various forcing locations. Annotations are sensor location.

of $\langle c_\mu \rangle$. Each closed-loop data point is annotated with the corresponding sensor location x/c . Here, the dramatic difference in behavior between sensor locations $0.8 \leq x/c \leq 0.95$ and $1.1 \leq x/c \leq 1.4$ is readily apparent. For sensor locations in the first group, the values of $\langle c_\mu \rangle$ are less than 10^{-5} , while $\langle c_\mu \rangle \geq 9 \times 10^{-3}$ for sensor locations in the second group. In the first group, the feedback is too weak to produce strong coherence of the vortex shedding, while in the second group the feedback loop has led to strongly coherent vortex shedding, and therefore significant reductions in the separation length. Note that, within each group, the separation length exhibits an oscillatory behavior as a function of sensor location. This appears to be related to the variations in the phase relationship as a function of sensor location, suggesting that any sensor location may be used efficiently, if the phase shift is optimized by introducing that appropriate time lag τ .

2.7.2 Frequency/Amplitude Control Feedback Scheme Simulations

As discussed in Section 2.5.2, as an alternative to feedback of the actual time-varying waveform of the downstream pressure field, one may consider feedback schemes which consider the frequency and amplitude of the downstream pressure field, but ignore the phase. This leads to considerable simplification of the control system hardware and processing requirements. One could also consider a multi-level control system design, involving an 'inner loop' of the type discussed in the previous section, and an 'outer loop' which adjusts the gain and/or time lag to achieve a desired degree of suppression of flow separation.

In order to investigate frequency/amplitude control, or equivalently, outer loop behavior in the case of a multi-level system, the following model problem was considered. A relevant aerodynamic quantity was created by averaging the instantaneous pressure at six equidistant downstream stations. We designate this C_L since it would correspond to a lift coefficient for a free flight configuration. Due to the vortex shedding, C_L oscillates in time, however, these oscillations are at frequencies that are much higher than those for the time scales that are relevant for flight control. Therefore C_L can be low pass filtered, yielding a relatively slowly varying temporal mean lift, which is what we would like to control. This time dependent 'lift' directly corresponds to the quantities we would use for flight control.

The low-pass filter chosen is a linear filter with cutoff frequency $1/\tau_c$. Denoting the filtered lift coefficient as \overline{C}_L the filter is then defined by

$$\frac{\partial \overline{C}_L}{\partial t} = \frac{1}{\tau_c} (C_L - \overline{C}_L).$$

Let C_L^* denote the desired mean pressure. The goal of control is to have the filtered lift coefficient \overline{C}_L follow a specified desired time history, $C_L^*(t)$, consisting of ramps up, holds, and ramps down. The current controller assumes amplitude modulation of a quasi-sinusoidal forcing signal at a forcing frequency determined by open-loop experiments. That is, $v_A(t) = A(t) \sin(\omega t)$ is the instantaneous blowing velocity, where $A(t)$ is the instantaneous quasi-sinusoidal magnitude and ω is the forcing frequency.

A simple model of the filtered mean pressure dynamics used for control design purposes is

$$\frac{\partial \overline{C}_L}{\partial t} = \frac{1}{\tau} (-\overline{C}_L + C_{L_0} + \alpha |A|),$$

where τ is a characteristic time, C_{L_0} is the lift coefficient for the unforced flow, and α is a coefficient of the static response. The coefficients α and C_{L_0} were determined by a linear fit to the open loop static response data. The characteristic time, τ , was estimated from open loop step response data. This equation is linear except for the absolute value function of A . A simple feedback control law for this system is

$$A(t) = K \overline{C}_L + K_r C_L^*, \quad (40)$$

where K and K_r are constants. Increasing K decreases the response time and reduces error. K_r is chosen to ensure that the steady-state gain is one. Equation 40 is only valid if A is nonnegative. If the amplitude thus computed is negative, A is set to be zero.

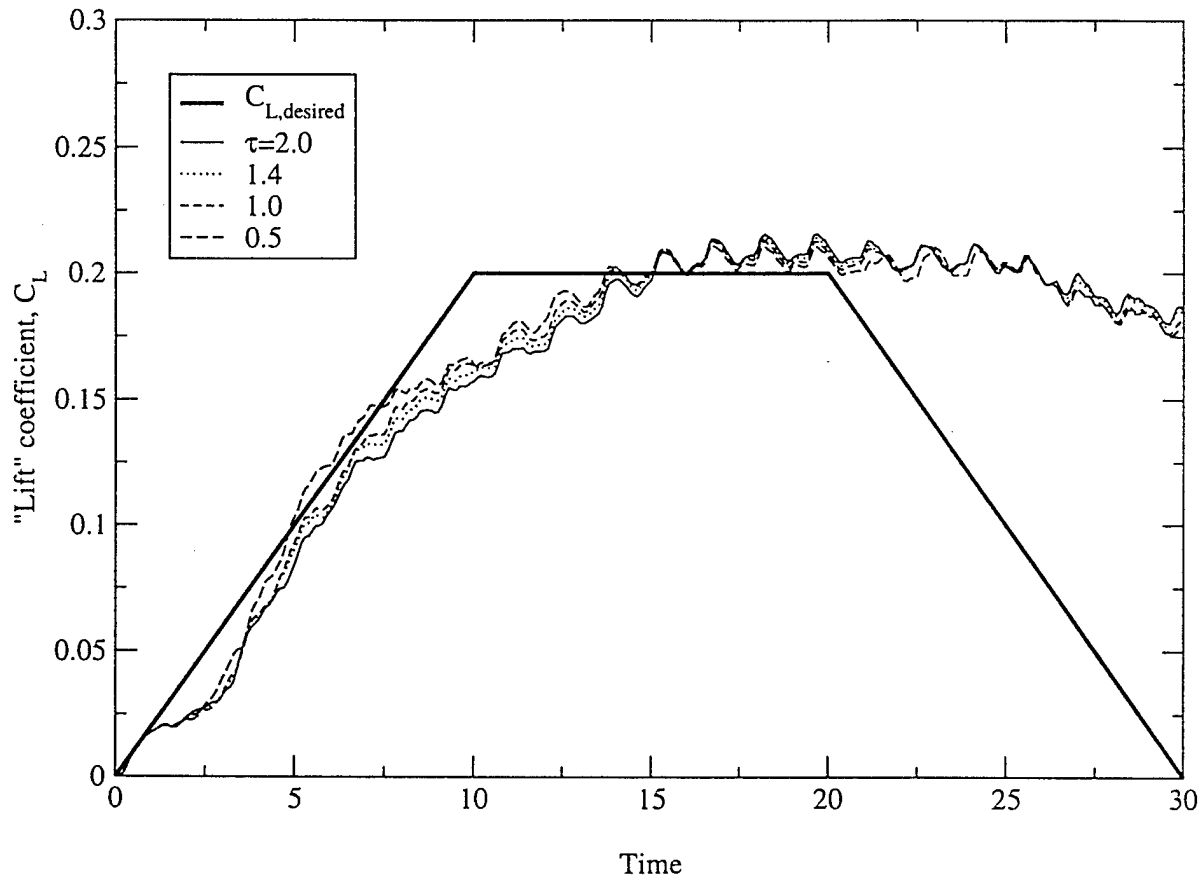


Figure 2.11: Dynamic trajectory. Thick black line is the requested trajectory.

The CFD simulation results for the actual and target trajectories are plotted in Fig. 2.11. The system lift coefficient is seen to follow the desired trajectory of the ramp up with reasonable accuracy, and to level out at the desired hold condition. In spite of the significant hysteresis effects associated with separated flows, control is established in approximately ten excitation periods in this simulation. Note that typical excitation frequencies for a flight vehicle are of the order 100-200 Hz, so that a response time on the order of 10 periods is a small fraction of a second.

For the the ramp down period ($t > 20$), the response time is much slower. This is a flow hysteresis effect, rather than a controller issue, as can be seen from the fact that soon after $t = 20$, the controller ramps off the forcing completely. The behavior is therefore consistent with the observation that for open loop forcing, when the excitation is removed, the flow remains attached for a significant number of shedding cycles. One reason that the hysteresis effect is so much more pronounced for a ramp down as compared to a ramp up, is that the initial transient associated with a quick change of the forcing input is associated with a single very strong structure which is extremely effective at mixing the flow and reattaching the bubble. For a ramp up, the controller can take advantage of this initial transient to quickly establish control. For the ramp down, however,

there is no corresponding effect: even when stopping the actuation completely, a slow recovery time is observed.

2.8 Summary

A theoretical and computational study of closed-loop feedback control of flow separation has been carried out. This work builds on previous open-loop investigations of active flow control, by focusing on separation control through the enhancement of the vortex shedding which occurs naturally in separated flows. Two different approaches to feedback control have been examined. These are phase control schemes, which involve feedback of the time-varying output from a downstream pressure sensor, and frequency/amplitude control schemes, which involves feedback related only to the frequency and amplitude of the downstream pressure signal, but not the phase. The latter approach leads to a significant reduction in the hardware and processing requirements for the control system.

For phase control schemes, we have shown that it is advantageous to place the sensor farther downstream, in order to reduce the sensitivity of the gain and to increase the efficiency of the system. However, when the sensor is placed farther downstream, we also introduce a larger time lag into the system, so that selection of the feedback transfer function phase (or time lag) becomes more crucial. The work presented here was rather preliminary in nature and did not involve a systematic optimization study. It is encouraging that, even in the absence of optimization, a simple phase control feedback scheme was shown to be as efficient as optimized open-loop AFC forcing. Thus, it appears that phase control methods have considerable promise.

For frequency/amplitude control schemes, we have demonstrated that even a simple scheme of this type can provide very good tracking for the ramp up (suppression of an existing flow separation bubble). However, the ramp down exhibits a significantly longer transient. This response time asymmetry must be considered when designing closed-loop attitude controls using AFC, and could be compensated for in a variety of ways. For example, in a full attitude stealthy control system, actuators would be paired on both the top and bottom surface of the wing. These actuators would act in opposing senses and the asymmetry of the control response could be compensated for, since one of the two controllers would always be in a ramp up mode, and able to take advantage of the corresponding short time constants.

Despite the fact that the closed-loop controllers used in this study were relatively simple, significant suppression of flow separation was achieved. The introduction of more sophisticated control laws would likely lead to improved performance. However, from a practical standpoint, there is merit in simplified approaches that are easily implemented. Both the phase control scheme and the frequency/amplitude control scheme would be relatively easy to implement in hardware, such as the radio control model flight demonstration program discussed in the following section.

3 Experimental Investigation of Sensor Triggered Vortex Generators

Main objectives of the effort are to identify control methods and provide realistic aerodynamic data to support the eventual control development. The following tasks were performed:

- Identify airfoil section amenable to flow control at low AoAs.
- Quantify effectiveness of different controls.
- Selected best combination of airfoil configuration and control among the ones tested.
- Design and evaluation of a simple hardware based system for control demonstration.
- Design and evaluation of a simple computer-based system for control demonstration.

Results of the effort are summarized below.

3.1 Airfoil Geometry Development

Three types of airfoil design, sketched in Fig. 3.1, were considered. In all cases, the design incorporated a natural separation zone (NSZ) at low angles of attack. By controlling the extent of separation in this region, forces and moment can potentially be generated. In design no. 1, the NSZ consisted of a backward facing ramp near the leading edge. The basic idea was to control the separation on the ramp, which then directly influenced the flow and thus pressure distribution over a large portion of the airfoil. In design no. 2, the NSZ was a "flap" with a large but fixed deflection. By controlling the flow over the flap, the equivalence of a movable flap deflection could be achieved. Design no. 3 incorporated a form of circulation control. A ramp was placed near the trailing edge of the airfoil to produce an NSZ. Though the airfoil area influenced directly by flow control was small, the state of separation at the trailing edge has a strong effect on the overall circulation. As such, large control forces could be generated.

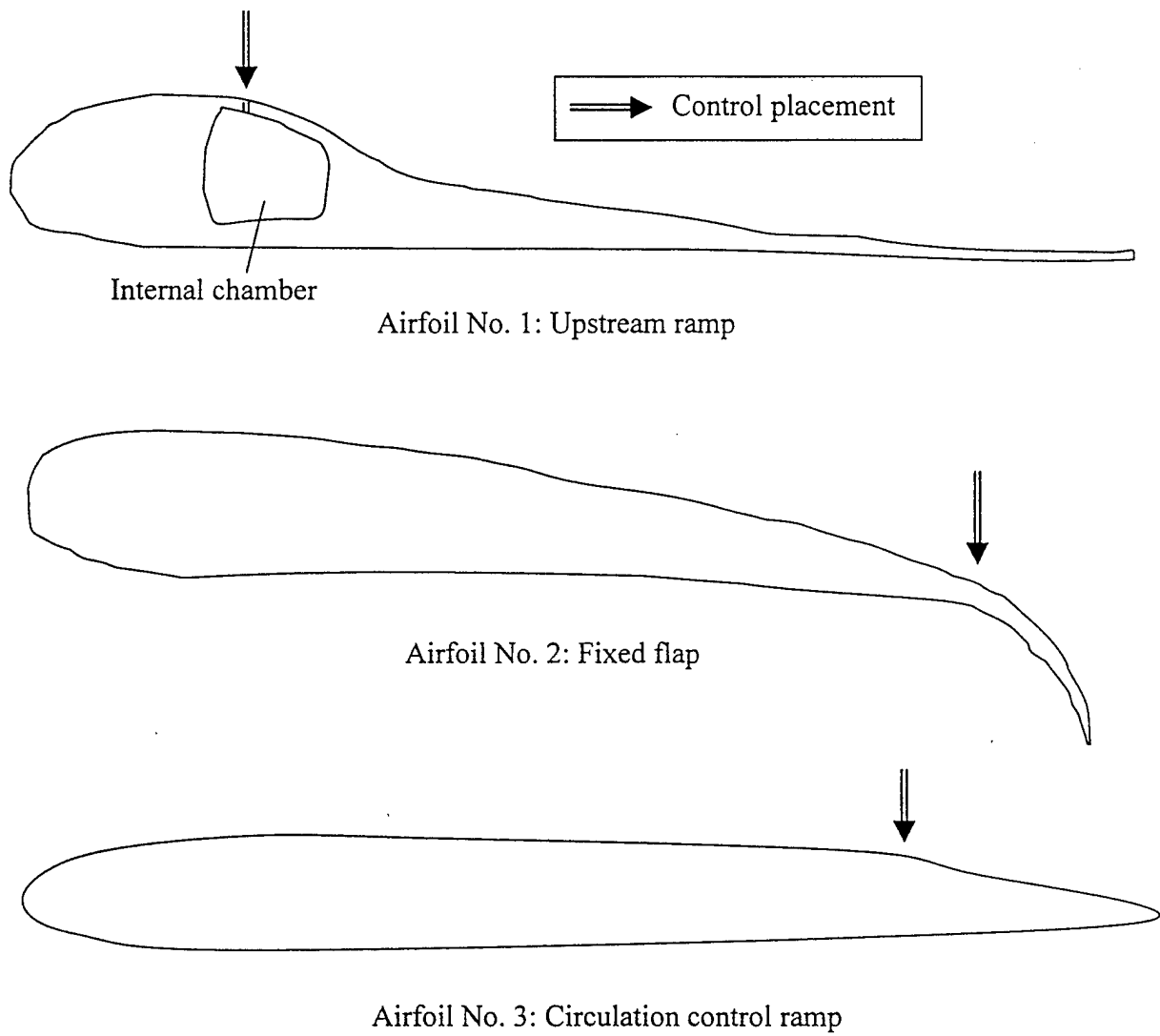


Figure: 3.1 Sketches of the airfoil designs

3.2 Experimental Evaluation Tools

The experiment was conducted at the University of Toledo 3-ft x 3-ft low-speed wind tunnel. The closed-loop tunnel was capable of speed up to 200 mph, and has a free-stream turbulence level of less than 0.5%. Testing for the present investigation was conducted at dynamic pressures ranging from 5 psf to 10 psf.

For each airfoil design, the effectiveness of different controls was investigated using one or more of the following standard testing methods:

- Surface flow visualization was obtained using thin threads glued to the upper airfoil surface.
- Aerodynamic forces and moments were obtained using a strain gage force balance.
- Surface pressure distributions were obtained using PSI pressure scanners.

3.3 Control Methods

The different methods of control investigated for each airfoil are listed in the following Table.

Airfoil Design	Blowing	Suction	Periodic Forcing	Acoustic Forcing
No. 1: Upstream ramp	X	X		
No. 2: Fixed Flap	X	X		
No. 3: Circulation control ramp		X	X	X

With the exception of blowing, all methods functioned by delaying separation. Depending on the direction of blowing, blowing could be used to delay or promote separation.

Of the three airfoils investigated, design no. 3 was found to be most amenable to control. Following discussions will therefore mainly be on airfoil no. 3, and results of designs no. 1 and 2 will be discussed only briefly. All investigations were focused on low angles of attack, ranging from 0° to at most 10° .

3.4 Airfoil No. 1 Results

For airfoil design no. 1, flow visualization results show that flow separation occurred shortly downstream of the beginning of the downward ramp. Based on previous studies, an effective location for implementing flow control would be a short distance upstream of the ramp. The eventual control design is shown in Fig. 3.1. A chamber was placed directly beneath the ramp surface, with a series of small discrete holes slightly upstream of the ramp allowing surface suction. Surface flow visualization revealed however that the holes alone caused a reattachment of the flow even without suction. It could be reasoned that the holes functioned as small vortex generators, which effectively delayed separation in a relatively modest adverse pressure.

Based on the observation, a reversed form of the original control scheme was devised. In this scheme, the holes would maintain flow attachment downstream of the ramp during normal operation. When a control force was needed, blowing would be applied through the holes to

induce separation. Though the flow behavior was subsequently confirmed using surface flow visualization, force balance data revealed that the flow changes failed to provide any significant control forces. The airfoil design and associated control thus either did not result in a large change in the surface pressure distribution, or that the control caused pressure to increase in one area but reduce in another. In both cases, no large net control force was generated.

3.5 Airfoil No. 2 Results

A wind tunnel model of the trainer wing with a fixed deflected flap was constructed. Discrete, spanwise suction was incorporated along the "hinge-line" as a mean of separation control. A differential pressure switch, normally opened but closed at 0.002 psi, was used as a simple sense-and-actuate unit. The low-pressure end of the switch was connected to a position slightly downstream of the discrete suction holes, and the high-pressure end to a position farther downstream. The positions were chosen such that when the flow was attached a sufficiently large pressure difference existed between the two positions, thereby closing the switch. When the flow became separated upstream of the forward position, however, the pressure difference diminished and the pressure switch opened. The switching thus reacted automatically to the separation state. The switch was then used to actuate a normally opened electric valve in the suction supply line. Results indicated that the pressure switch would response to changes in the state of separation, brought on by either changing angle of attack or imposition of flow control, and actuate the valve accordingly. Flow visualization revealed that the control caused the flow to reattach over a portion of the flap. Similar to the case of airfoil no. 1, however, force balance data revealed that the flow changes failed to provide a significant control force. Limited pressure data around the flap indicated that pressure increased in some areas but reduced in others. They also revealed that the control caused the flow to reattach only for a portion of the flap.

3.6 Airfoil No. 3 Results

A sketch of the airfoil section is shown in Fig. 3.1. The design incorporates a region of trailing edge flow separation at low angles of attack. The flow state at this region can significantly impact the circulation around the airfoil. Several flow controls were evaluated including:

1. harmonic forcing using a speaker coil,
2. harmonic forcing using a rotating, slotted cylinder, and
3. discrete steady suction.

Schematics of the controls are shown in Fig. 3.2. Of the three controls, discrete suction was found to be the most effective and shall be discussed in more detail.

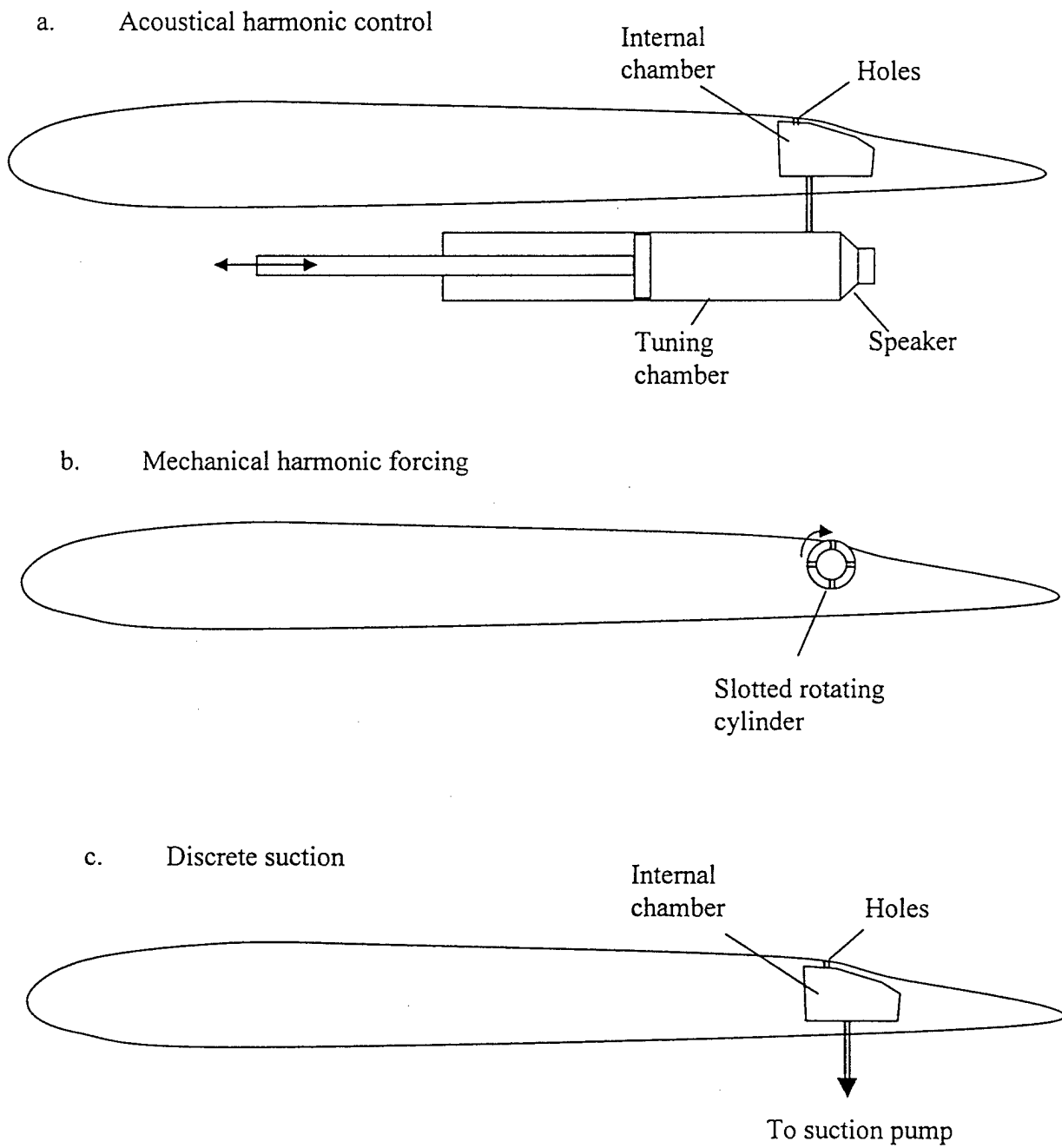


Figure: 3.2 Schematics of the three controls for airfoil no. 3

3.6.1 Experimental setup

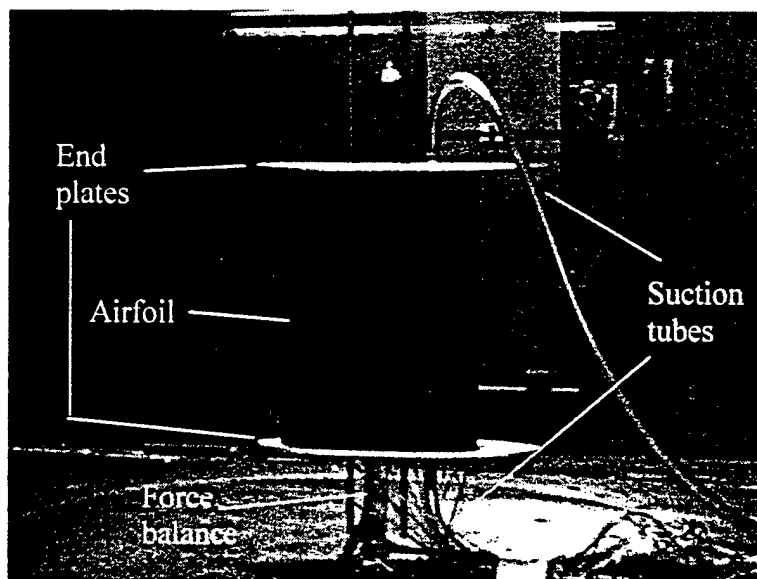


Figure: 3.3 Airfoil no. 3 mounted in the wind tunnel

Figure 3.3 shows a photo of airfoil no. 3 in the Toledo 3-ft x 3-ft wind tunnel. Surface flow visualization, strain gage force balance, and PSI pressure scanners were used in the investigation. Due to capacity limitation of the suction pump, only the middle 20% of the airfoil span was controlled when suction was used. Subsequently the change in the control force, though readily measurable, was relatively modest. Nevertheless, the control force was observed to directly relate to the change in surface pressure. Our discussions will therefore focus mainly on the pressure.

3.6.2 Pressure Data

A sketch of the airfoil section, with the approximate locations of the pressure ports, is shown in Fig. 3.4. The basic airfoil pressure distributions from zero to 10 degrees angle-of-attack are shown in Figs. 3.5 through 3.10.

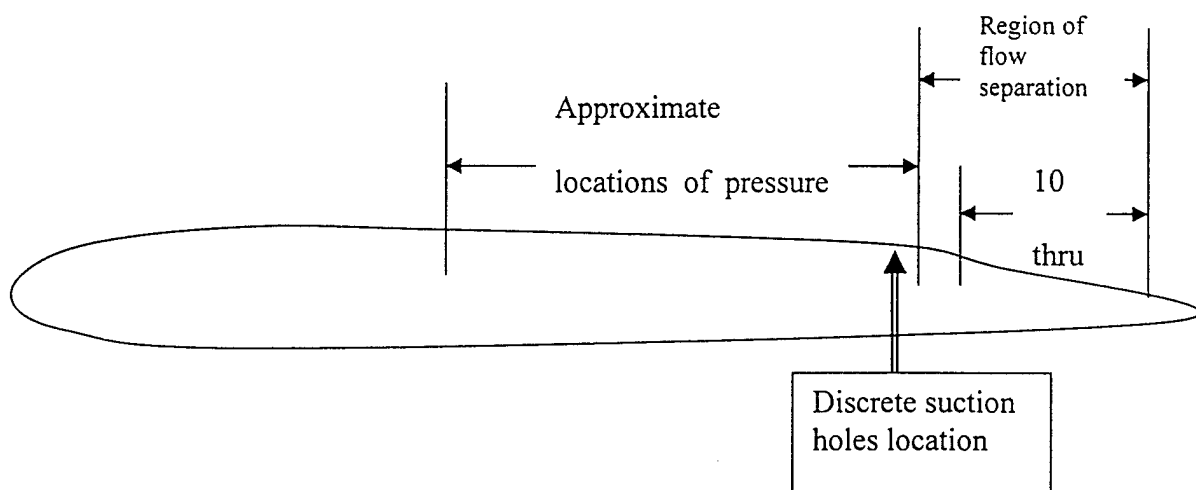


Figure: 3.4 Sketch of the airfoil cross-section and pressure port locations

The suction rate was controlled using a proportional electric valve. The control was imposed slightly upstream of the naturally separated region. The controlled airfoil pressure distributions from zero to 10 degrees angle of attack are shown in Figs. 3.5 through 3.10. The results indicated that substantial changes in the surface pressure could be induced using relatively small suction (in the order of 10^{-4} based on the airfoil area.) Changes were not confined to the trailing edge, but extended over most of the airfoil. This was due apparently to the effect of the trailing edge control on the overall airfoil circulation.

3.6.3 Simple Control Schemes

Two simple control demonstrations, based on the circulation control concept, were performed. The first was based on hardware that would be suitable for flight demonstration on the model aircraft, while the second used a multi-functional computer board to provide more flexibility in the control.

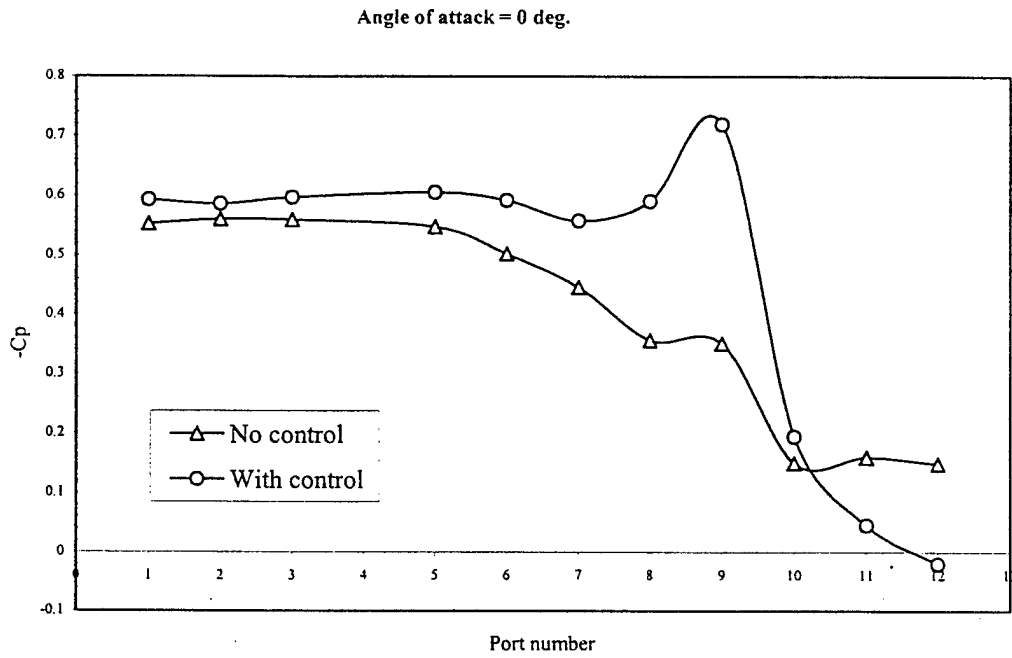


Figure: 3.5 Effect of control on pressure distribution

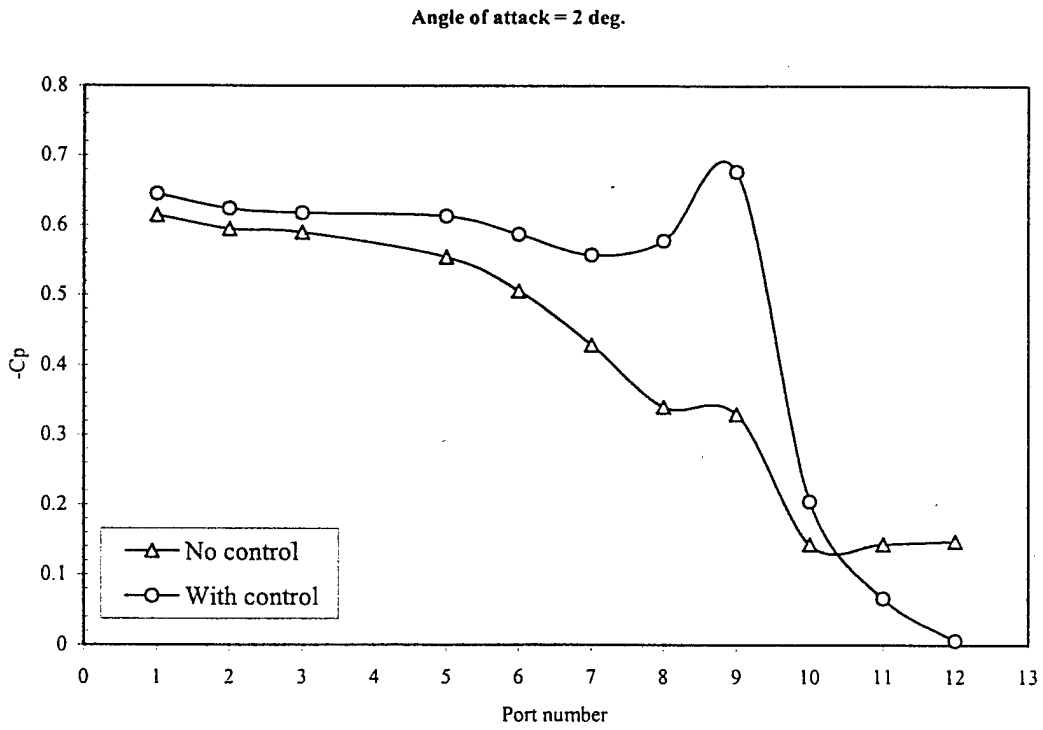


Figure: 3.6 Effect of control on pressure distribution

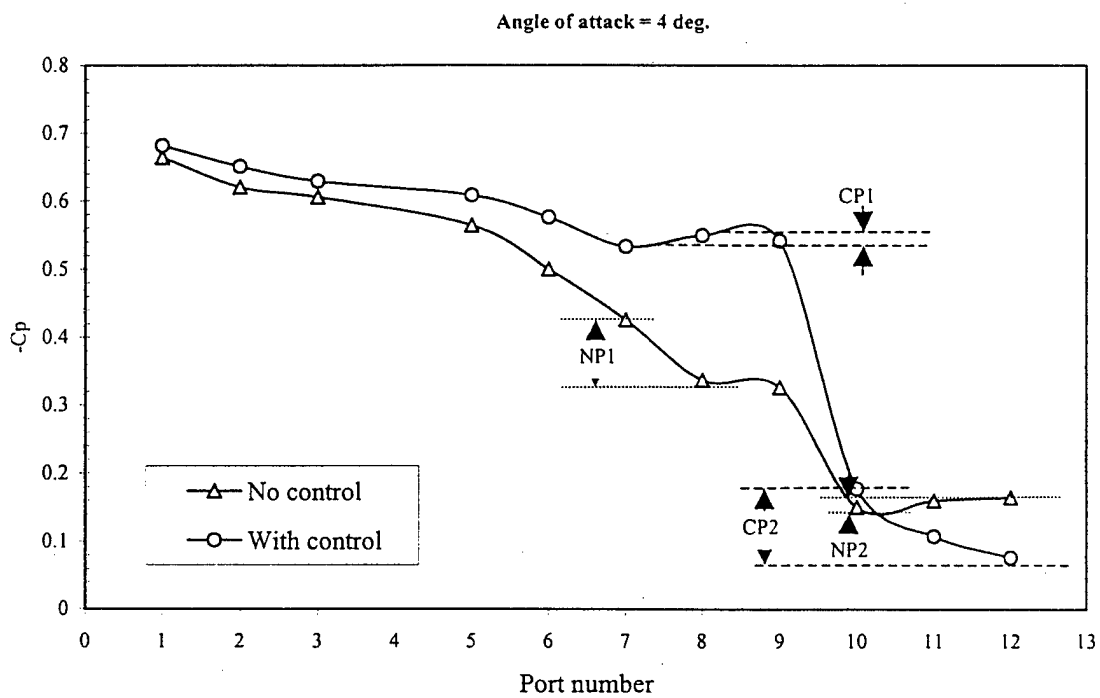


Figure: 3.7 Effect of control on pressure distribution

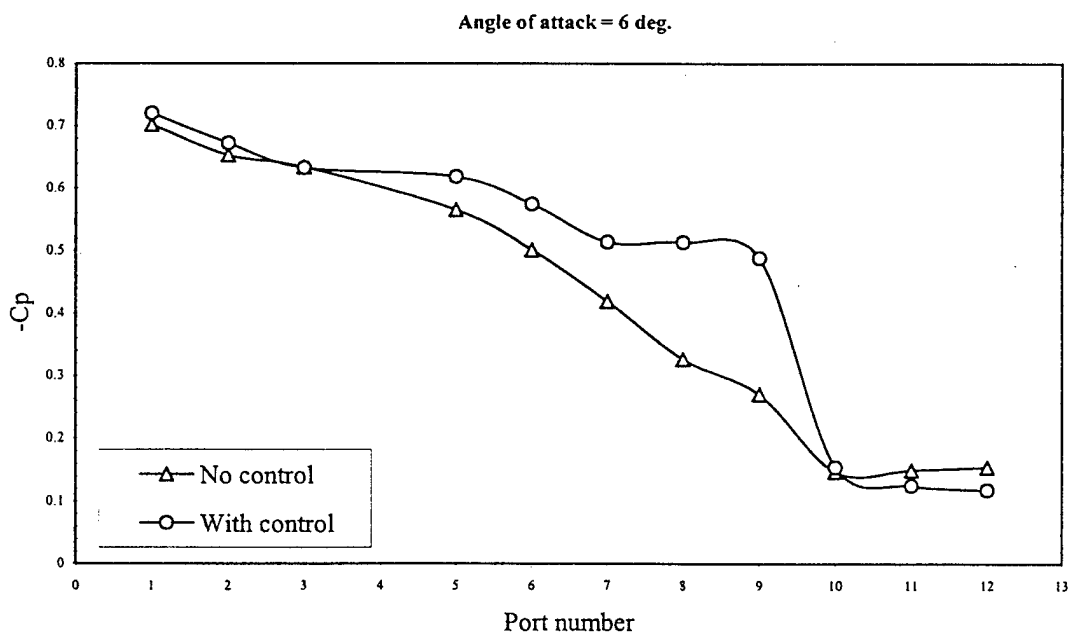


Figure: 3.8 Effect of control on pressure

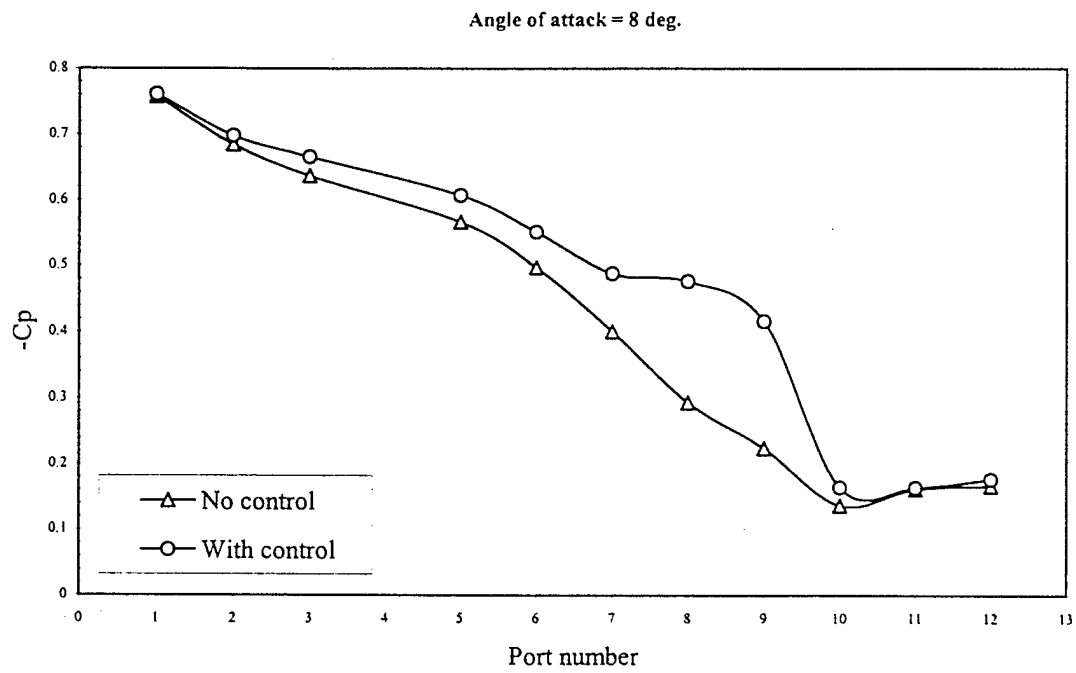


Figure: 3.9 Effect of control on pressure distribution

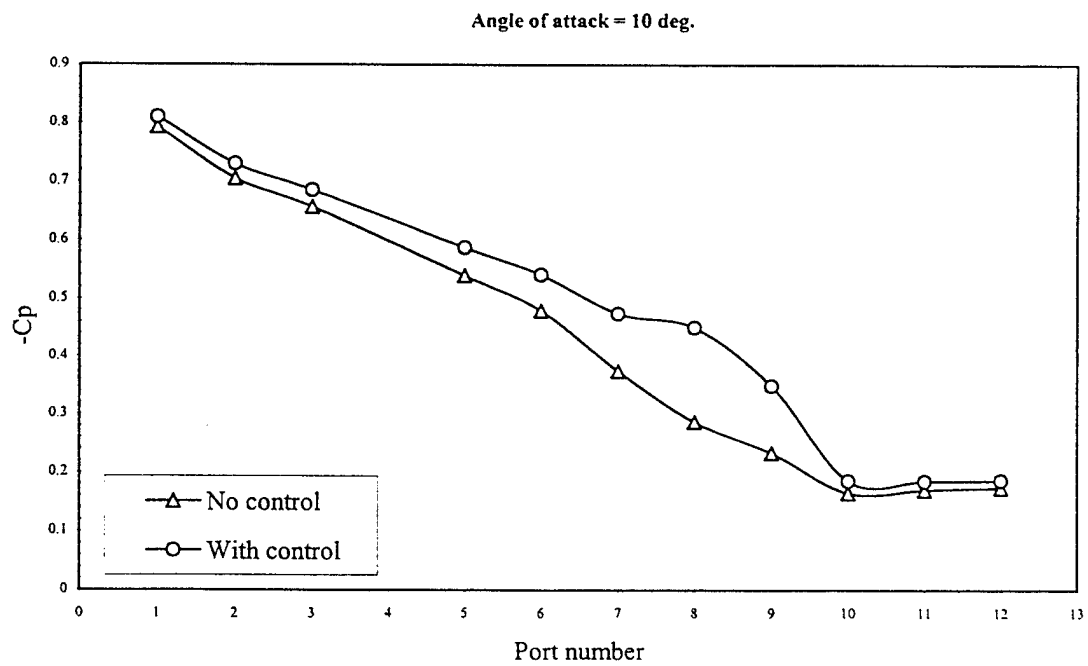


Figure: 3.10 Effect of control on pressure

Control Scheme No. 1

Figure 3.11 shows a schematic of the first control setup. For flight demo on a model airplane, low weight and power requirement were the main concerns. Flow separation sensing and flow control activation were achieved using a set of passive pressure sensing switches. The switches were normally open, and would close when the pressure differential rose above a certain preset threshold.

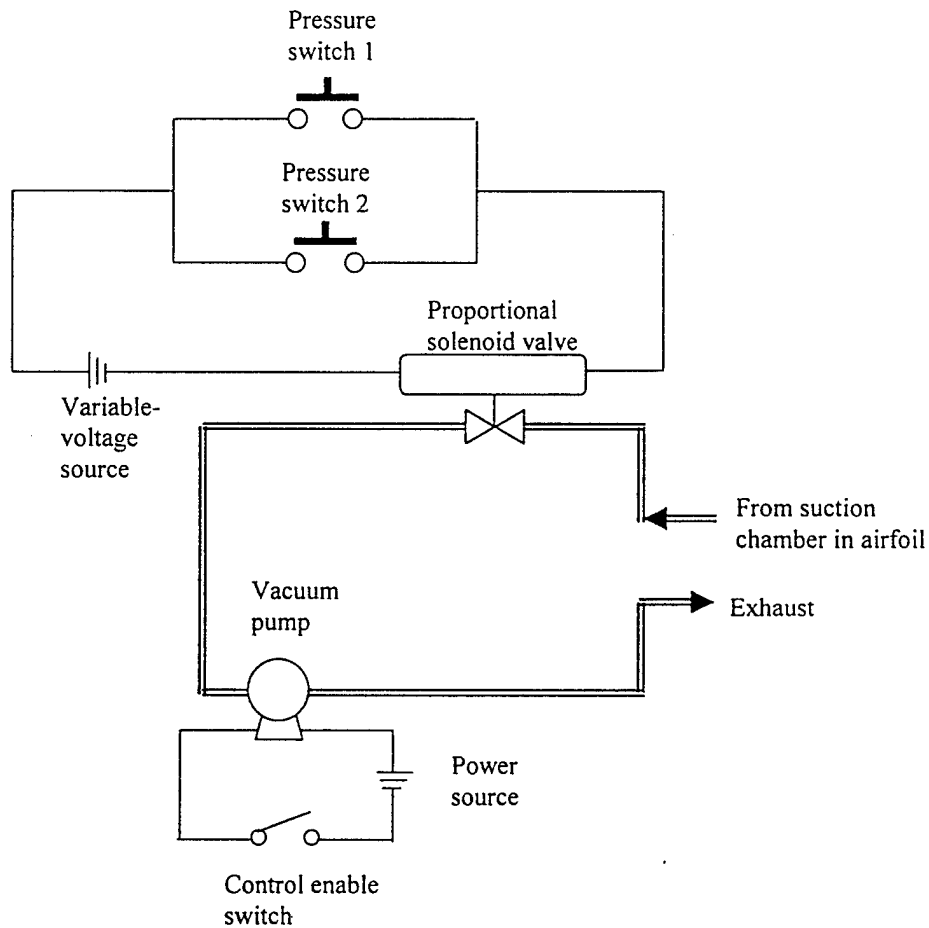


Figure: 3.11 Control scheme no. 1

The control scheme was based on the pressure signature of the airfoil. An example can be illustrated using the result at 4-degrees angle of attack shown in Fig. 3.7. Pressure ports 7 and 8 were connected to the vacuum and pressure inlets of switch no. 1 respectively, while ports 10 and 12 were connected to the vacuum and pressure inlets of switch no. 2 respectively. During the natural (uncontrolled) flow state, a large pressure differential existed between ports 7 and 8, thereby closing switch no. 1. Switch no. 2 remained closed due to the relatively small pressure differential in the separated flow region. When control was activated, however, the opposite

happened. A large pressure differential now existed between ports 10 and 12 due to flow reattachment, thereby activating switch no. 2. On the other hand, the pressure differential between ports 7 and 8 became relatively small, with the pressure at port 8 actually a little higher than at 7. Switch no. 1 was thereby open.

Flow state sensing and control were subsequently demonstrated successfully in a series of wind tunnel experiments. Brief report and videotape on the experiments are available upon request.

Control Scheme No. 2

A computer-based control system was developed. Figure 3.12 shows a schematic of the control setup. The output from either the pressure (or force) sensor was to sense the flow state. The control would then compare the sensor output to the desired level of pressure, and activate or deactivate the suction accordingly. The control force was typically minimal when suction was off and maximum when suction was on, signifying the two extreme flow states. Due to the lag in flow response to the control, any intermediate flow state between the extremes could be sustained by rapidly turning the suction on and off.

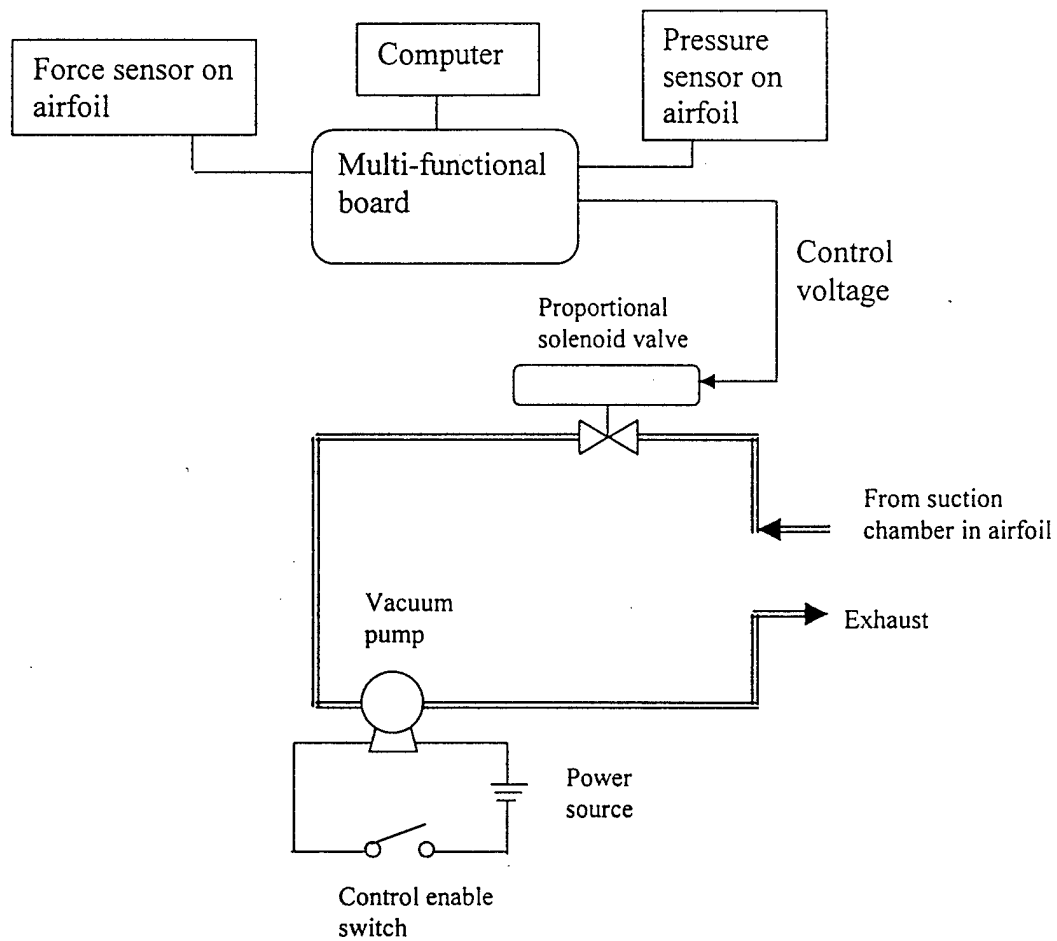


Figure: 3.12 Control scheme No. 2

Flow state sensing and control were demonstrated successfully in a series of wind tunnel experiments. The control was able to provide a desired pressure or force curve using the simple feedback scheme.

3.7 Summary

The above represents an initial step towards a complete control system. The concept can be applied to various parts of an airframe such as the wings and tails to provide different components of control force.

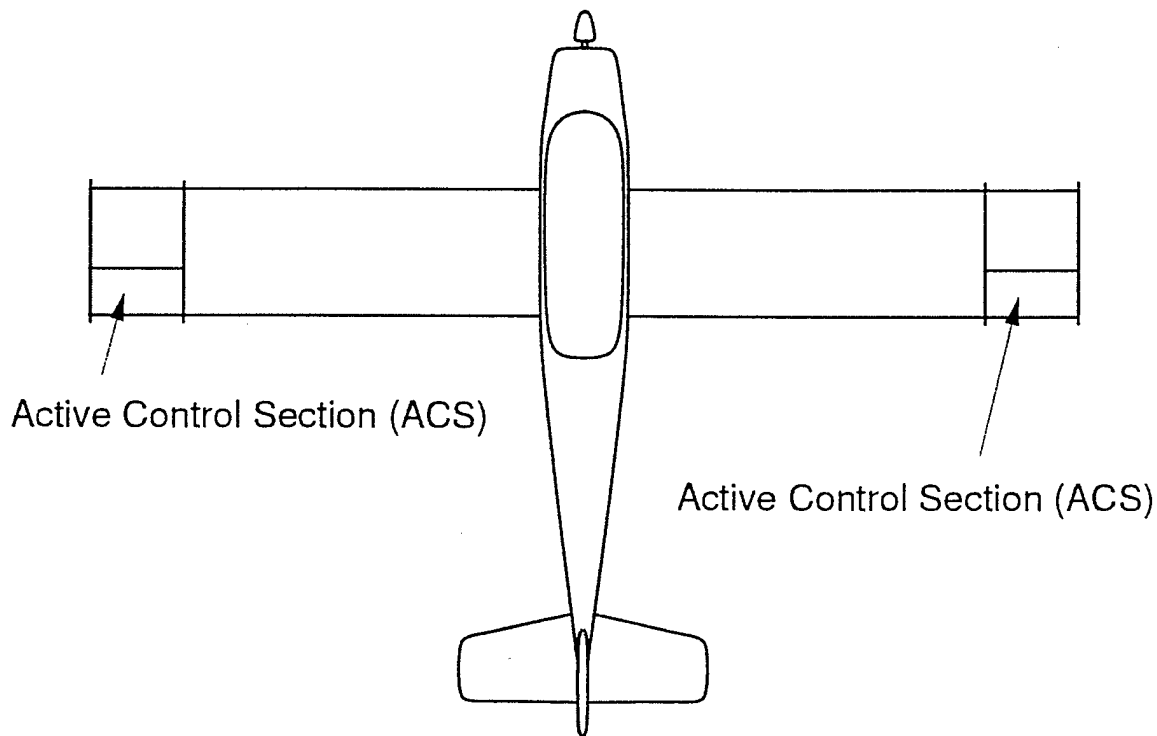


Figure 4.1: Schematic of Airplane with Active Control Sections (ACS)

4 Flight test program

In phase one of this project we have promised to control only one axis of the flying model, namely the roll axis. For the actual flying model, we used a modified airfoil shape in an Active Control Section (ACS) near each wing tip, of size approximately 10-15% of the span (figure 4). The airfoil in the ACS is designed such that separated flow occurs over a designated region of the airfoil on the upper surface in level flight (see figure 4). For roll maneuvering, active control actuators will be energized to produce flow reattachment in the ACS region of one wing, thereby increasing the lift of that wing and producing a roll moment. An alternate control strategy would be to use active flow control to keep the flow attached in the ACS regions during level flight. A roll moment could then be generated by turning off the active flow control actuators on one wing, thereby allowing the boundary layer to separate and creating an unbalance in the lift forces. This approach would have the advantage of less drag during level flight, but would require a continuous energy input for the active control actuators.

4.1 Development of actuators for flight demonstration airplane

We had considered numerous candidates for actuators to be employed in the flying model. After initial evaluations, we have designed an actuator system based on one which was successfully

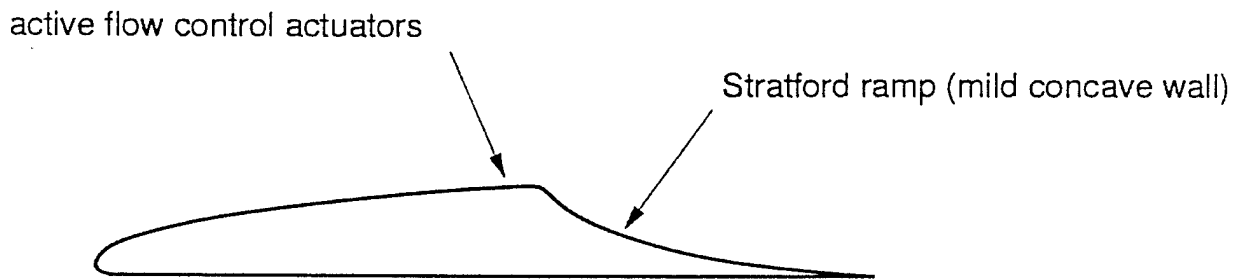


Figure 4.2: Airfoil section with actuators and Stratford ramp locations identified.

tested experimentally for low pressure turbine blades by (Rivir et al., 2000, WPAFB). In our system, pulsed zero-mass jets (pulsed vortex generator jets, PVGJs) emanate from a row of very small holes (1mm diameter and 10 mm apart) which are directed in the spanwise direction and angled at 30 degrees from the surface. These actuators generate longitudinal vortices that cause an exchange of low momentum fluid near the wall with high momentum fluid farther from the wall, so that the boundary layer, which would separate in the absence of control, remains attached. In both schemes, streamwise vorticity is generated by the distortion of vortex lines of the mean boundary layer, producing energetic disturbances with relatively small control inputs. Variation in the strength of the control can be produced by simply varying the actuator pulse rate or frequency. For the actuator development we have relied extensively on experimental investigations using wind and water tunnels as well as on Direct Numerical Simulations (DNS).

The PVGJ actuators can be driven various systems. For our flight model we developed and tested two entirely different driver systems. One driver is a mechanical system which uses a reciprocating piston pump that is driven by a speed controllable electric motor. This design allows for constant amplitude, variable frequency actuation. The second driver uses an off the shelf loudspeaker in combination with a signal generator and an amplifier. This system allows for an arbitrary signal and amplitude for the actuation and is well suited for closed loop feedback control.

The air oscillations produced by either the piston pump or the speaker system are ducted directly to the row of holes of the PVGJ actuators in the ACS by a flexible plastic hose. Both driver systems were tested extensively in the wind tunnel prior to implementation into the flying model.

4.2 Development and construction of flight models (UA-1)

The flying model is based on a modified model airplane trainer with a wing span of 87.5 inches including the two ACS's (span of each ACS is 11 inches). We are using a modified Liebeck (1978) type airfoil (see figure 4) for the ACS region of the wing. The Liebeck design is a high lift / low drag configuration, employing a Stratford (1959) ramp wall geometry downstream of the location of maximum airfoil thickness. The airfoil shape in the ACS region will be chosen such that it is "off-design" in level flight conditions; with the boundary layer separating immediately downstream of the start of the ramp. Active control actuators can then be used to reattach the flow, generating a control force. A photographs of the flight model are given in figure 4.2. Due to it's high-wing configuration and due to the driver system being mounted under the fuselage (hidden

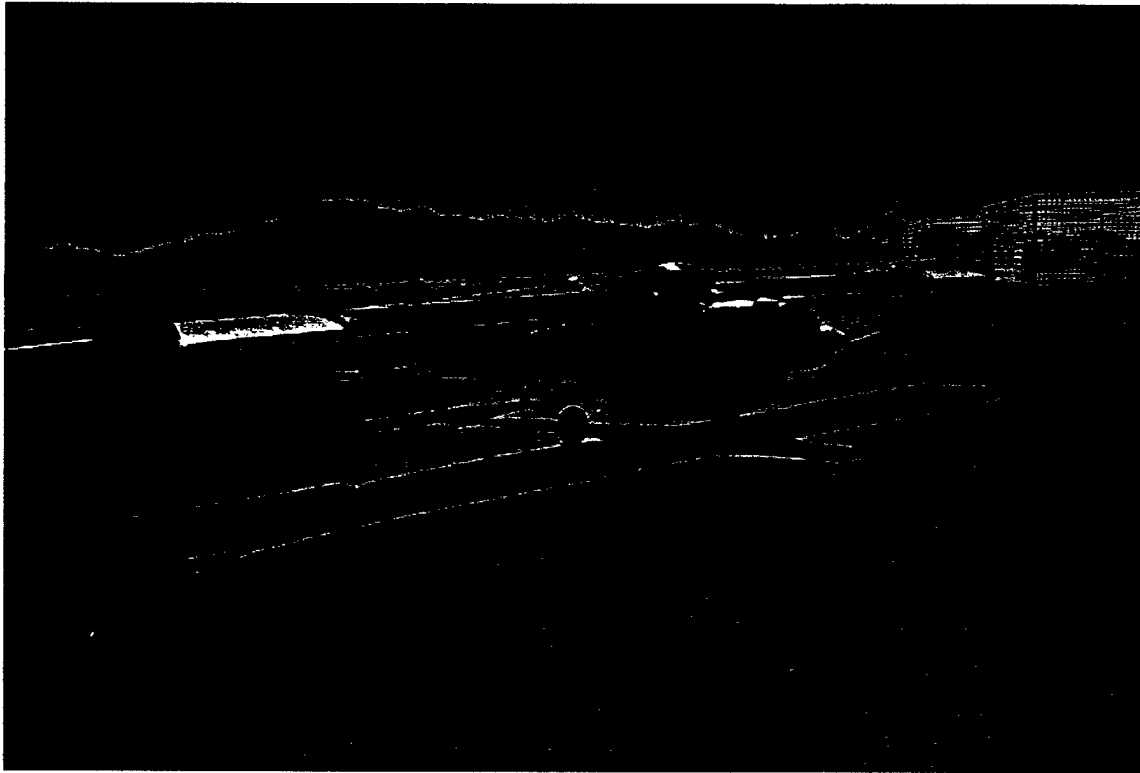


Figure 4.3: Photographs of Flight Model

by the cowling in figure 4) this airplane is actually very stable with respect to the roll axis. As a consequence, demonstrating roll maneuvering using AFC is considerably more challenging than with more typical airplane configurations. For the Flight model the Active Control Sections (ACS) with the embedded actuators were added to the wings as extensions, increasing the span from 65.5 inches to 87.5 inches. Shorter ACS's were also developed and flight tested. Two Planes were constructed. One with the mechanical pump system and one with speaker system

4.3 Flight Testing

Both airplanes and actuator/driver systems were flight tested extensively. The airplanes and actuator systems performed beyond expectations: Very high roll moments could be achieved. Even "aileron-rolls" (without any aileron action whatsoever) could be performed although for AFC at this point was only active on one wing and considering the high resistance to roll of the flight model (see comments above)!

The functionality of both airplanes and actuator/driver systems was demonstrated successfully in a series of flights on June 11, 2002, with Dr. James Myatt, WPAFB, observing.

4.4 Summary

With respect to the development of the flight model and flight testing we have at least fulfilled and possibly exceeded all that was promised in the proposal. The actuator effectiveness and the roll moment that we achieved in the flight model was far beyond what had been anticipated. The actuator system was specifically developed so that it is suitable for AFC with feedback control in combination with closed loop attitude control; specifically it allows for variable amplitude and flexibility in waveform. This system functioned extremely well in the wind tunnel and as well as in flight tests.

With this system the proportional feedback control demonstrated numerically in section 2.7.1 will be relatively easy to implement in the flight model. The actuators currently being used can be driven by a simple digital controller linked to a pressure sensor on the airfoil surface. By adding several pressure sensors downstream of the nominal separation point we can achieve true attitude control of the type demonstrated in section 2.7.2.

5 Conclusions

5.1 Theory and Simulations for Feedback Control of Flow Separation

The objectives of the investigation of feedback control of flow separation were to develop simple approaches to enhancing separation control through the introduction of feedback, and to demonstrate the effectiveness of these approaches using computational fluid dynamic simulations.

The separation control strategy we have pursued is the excitation of strong instability waves on the separated or marginally separated flow, in order to increase the mixing and entrainment and thereby cause the flow to reattach. The effectiveness of this approach has been well demonstrated in open-loop active flow control schemes, where an actuator is driven by a time-harmonic input to generate an instability wave in the (pre-determined) unstable frequency range. In our investigation of closed-loop control, one goal was to develop a feedback system that would automatically enhance the naturally occurring instability wave field, without the need to preselect the appropriate frequency and amplitude of the forcing. A second goal was to develop a system whereby the amplitude and frequency of the forcing could be controlled to obtain a desired result, such as a specified time variation of airfoil lift.

Enhancement of the naturally occurring instability wave field is a non-standard problem from the controls viewpoint, since our objective is to enhance rather than suppress a disturbance field. Linear theory provides useful guidance for the amplitude and phase relationships required to reinforce the naturally occurring instability wave field. The eventual saturation of the wave (vorticity) field downstream of the actuator involves nonlinear effects, which fortunately do not need to be modelled in detail for the present application.

Two types of linear feedback control schemes were explored. The phase control scheme involves suitable conditioning and feedback of the time-varying pressure field from a downstream wall pressure sensor. This scheme requires proper determination of the phase of the feedback, in order to reinforce the pre-existing instability wave field. In the frequency/amplitude feedback scheme, the actuator input is based on measurements of the frequency and amplitude characteristics of the downstream pressure field—no attempt is made to determine or utilize the phase information from the downstream pressure field. This leads to a significant simplification of the controls system hardware and processing requirement. In this case, the unsteady field produced by the actuator must overwhelm the naturally occurring instability wave field (as is the case for open-loop approaches). This requirement is satisfied even with small-amplitude actuator outputs, since these are exponentially amplified due to the unstable nature of the mean flow in the separated region.

Computational fluid dynamic simulations were carried out for a simple phase control feedback scheme, and for a simple amplitude control feedback scheme. For the phase control scheme, it was demonstrated that levels of flow separation suppression comparable to, and in some cases better than, previous open-loop investigations could be obtained. For the amplitude control feedback scheme, a simple nonlinear controller was designed, in order to use amplitude control to achieve a desired temporal trajectory for the airfoil lift force. The simulations demonstrated that a desired change in airfoil lift could be achieved on a time scale on the order of 10 periods of the active control forcing. This is a relatively short time period relative to the time scale of interest in air

vehicle maneuvering. Overall, the results that were achieved are encouraging, considering the relatively simple nature of the feedback laws employed. The performance of the control systems could undoubtedly be improved by optimization studies and by introducing more sophisticated control schemes. However, there is merit in simple approaches that are easily implemented, such as those developed here.

5.2 Experimental Investigation of Sensor Triggered Vortex Generators

The main objectives of the Experimental Investigation of Sensor Triggered Vortex Generators were to identify control methods and provide realistic aerodynamic data to support the eventual control development. Three types of airfoil design were considered. In all cases, the design incorporated a natural separation zone (NSZ) at low angles of attack. By controlling the extent of separation in this region, forces and moments can be controlled. Design no. 3 incorporated a form of circulation control using a ramp placed near the trailing edge of the airfoil to produce a NSZ. Though the area of the airfoil influenced directly by flow control was small, the state of separation at the trailing edge has a strong effect on the overall circulation. Thus large control forces could be generated. Of the three airfoils investigated, design no. 3 (related to the Stratford ramp) was found to be most amenable to control. All investigations were focused on low angles of attack, ranging from 0° to at most 10° . Several flow actuators were evaluated including: harmonic forcing using a speaker coil, harmonic forcing using a rotating, slotted cylinder, and discrete steady suction. Of the three actuators, discrete suction was found to be the most effective.

The control force was observed to directly relate to the change in surface pressure. The control was imposed slightly upstream of the naturally separated region. The results indicated that substantial changes in the surface pressure could be induced using relatively small amounts of suction. Changes were not confined to the trailing edge, but extended over most of the airfoil. This was due apparently to the effect of the trailing edge control on the overall circulation of the airfoil.

Two simple control demonstrations, using design no. 3, were performed. The first was based on hardware that would be suitable for flight demonstration on the model aircraft, while the second used a multi-functional computer board to provide more flexibility in the control. Flow separation sensing and flow control activation were achieved using a set of passive pressure sensing switches. Flow state sensing and control were subsequently demonstrated successfully in a series of wind tunnel experiments. A brief report and videotape on the experiments are available upon request. A computer-based control system was also developed. The control force was typically minimal when suction was off and maximum when suction was on, signifying the two extreme flow states. Due to the lag in flow response to the control, any intermediate flow state between the extremes could be sustained by rapidly turning the suction on and off. Flow state sensing and control again were demonstrated successfully in a series of wind tunnel experiments. The control was able to follow a desired target curve (pressure or force) using the simple feedback scheme. The above represents an initial step towards a complete control system. The concept can be used with different control schemes.

5.3 Flight test program

In Phase I of this project we have promised to control the roll axis of the flying model. For the actual flying model, we used a modified airfoil shape in an Active Control Section (ACS) near each wing tip, of size approximately 10-15% of the span. The airfoil in the ACS is designed such that separated flow occurs over a designated region of the airfoil on the upper surface in level flight. A Liebeck design (high lift / low drag configuration) employing a Stratford ramp wall geometry downstream of the location of maximum airfoil thickness has proven ideal. For roll maneuvering, actuators are energized to produce flow reattachment in the ACS region of one wing, thereby increasing the lift of that wing and producing a roll moment. The choice for a flight actuation system is based on a system that was successfully tested experimentally for a different application (low-pressure turbine blades by Rivir et al., 2000, WPAFB). System features include proportional control and allow for implementation of local feedback control for the actuator system, in addition to the global feedback associated with the attitude control system.

The actuators generate longitudinal vortices that cause an exchange of low momentum fluid near the wall with high momentum fluid farther from the wall, causing boundary layers that would separate in the absence of control to remain attached. Streamwise vorticity is generated by the distortion of vortex lines of the mean boundary layer, producing energetic disturbances with relatively small control inputs. Proportional control was achieved by varying the actuator pulse rate or frequency. The actuator development relied extensively on experimental investigations using wind and water tunnels as well as on Direct Numerical Simulations (DNS).

The flight model was developed and tested with two different driver systems:

- i. a mechanical system using a reciprocating piston pump that is driven by a speed controllable electric motor. This system allows for constant amplitude, variable frequency actuation.
- ii. a speaker system using an off-the-shelf loudspeaker in combination with a signal generator and an amplifier. This system allows for arbitrary wave form actuation and is well suited for closed-loop feedback control.

Due to the high-wing configuration of the flight model and the location of its driver system under the fuselage, this airplane is actually very stable with respect to the roll axis. As a consequence, demonstrating roll maneuvering using AFC is considerably more challenging than with more typical airplane configurations. Two planes were constructed, one with the mechanical pump system and one with the speaker actuator system.

Both airplanes and actuator/driver systems were flight tested extensively. The airplanes and actuator systems performed beyond expectation. Very high roll moments could be achieved. In spite of the high resistance to roll of the flight model, 'aileron rolls' (without active control replading the aileron deflection) could be performed even with AFC active on only one wing!

A Initial Computational Fluid Dynamic (CFD) Simulations

Basic guidance on design parameters for vortex generator jets, such as hole size, spanwise spacing, jet velocities, pitch and skew angles, etc., is provided by the experimental studies of Johnston and his co-workers, while the studies of Ng and his co-workers provide similar information for the case of discrete vortex generating suction. However, as with all experimental studies, the level of detail regarding spatial variations of the flow field and its evolution as the physical parameters are varied is necessarily limited. Thus, computational fluid dynamic simulations can play an essential role in more fully describing the interaction of the actuator flow with the base flow field past the wing, the downstream development of the flow field and its dependence on parameters of interest. This information is helpful for effective design of the actuators and active control sections, and for development of the reduced-order models that are required in order to incorporate the influences of the active flow actuators into the control system.

The Wind CFD tools suite were used in the present study. Many of these tools are available in the public domain through the NPARC Alliance led jointly by AEDC and NASA Glenn Research Center. The primary feature is the flow solver Wind. Wind is a general purpose Euler and Navier-Stokes solver. Wind operates in two or three dimensions with structured (patched and overlapping) and unstructured grids. Any valid grid can be utilized, Wind places no restrictions on the point or slope discontinuities at zone interfaces. A mature zone coupling technique, in production since 1985, ensures continuity of the solution across zone boundaries. Wind has a library of boundary condition routines available on a point-by-point basis.

Wind incorporates a number of user-selectable (by zone) solution algorithms. Explicit Runge-Kutta time integration options of up to third order are also available for time accurate calculations. Grid sequencing is available to speed convergence on large grids. The spatial operator may be switched to various first through fifth order spatial schemes, also total variation diminishing (TVD) limiters may be activated. Other available schemes include standard second order and fourth order central differencing with added numerical dissipation. Much of the basis for the time accurate algorithms, and the default spatial scheme, are based on the analysis of Cain and Bush (1994) that includes analysis of wave propagation on stretched grids.

The primary focus of the initial computational simulations in Phase I were the investigation of the formation and evolution of longitudinal vortices and their effects on boundary layer separation. The approach was to create a geometric representation of the Extra 300 LX wing, including the actuators and active control system. The simulations include blowing and suction capabilities, with control of the actuator spanwise array characteristics, chordwise location and blowing or suction levels. The simulations are clearly sensitive to the treatment of boundary layer transition and separation. It is possible in the Wind code to explicitly specify a separation location or a region over which separation occurs. To achieve consistency with the wind tunnel experiments and the flight test, a boundary layer tripping strip was considered to ensure transition at a specific location in the experiment and flight-testing. A dense grid was utilized in the outboard active control section regions, in order to accurately represent the longitudinal vortices. The Wind code allows distinct zones for the dense grid outer region abutted to a coarser grid for the Extra 300 wing without active flow control.

The initial reference computations were obtained using the steady state turbulent WIND option with a 2nd order physical space computational scheme, a freestream Mach = 0.1 and flow at a 4 degree angle of attack. The grid was constructed in 4 zones (161x65x41, 81x65x33, 81x17x41, 41x17x33) with 682,268 points total for the base wing and additional points for the control section. The farfield grid extends approximately 20 chord length from the wing to limit issues with imperfect boundary conditions. Below, in fig. A-1, the wing surface and root surface grids are shown. Figure A-2 shows the root airfoil grid. Figure A-3 shows the Mach contours at the root cross-section for flow over this wing. Figure A-4 shows the dimensionless pressure coefficient C_p contours on the upper surface of the wing. Figure A-5 shows the dimensionless pressure coefficient C_p contours on the lower surface of the wing.

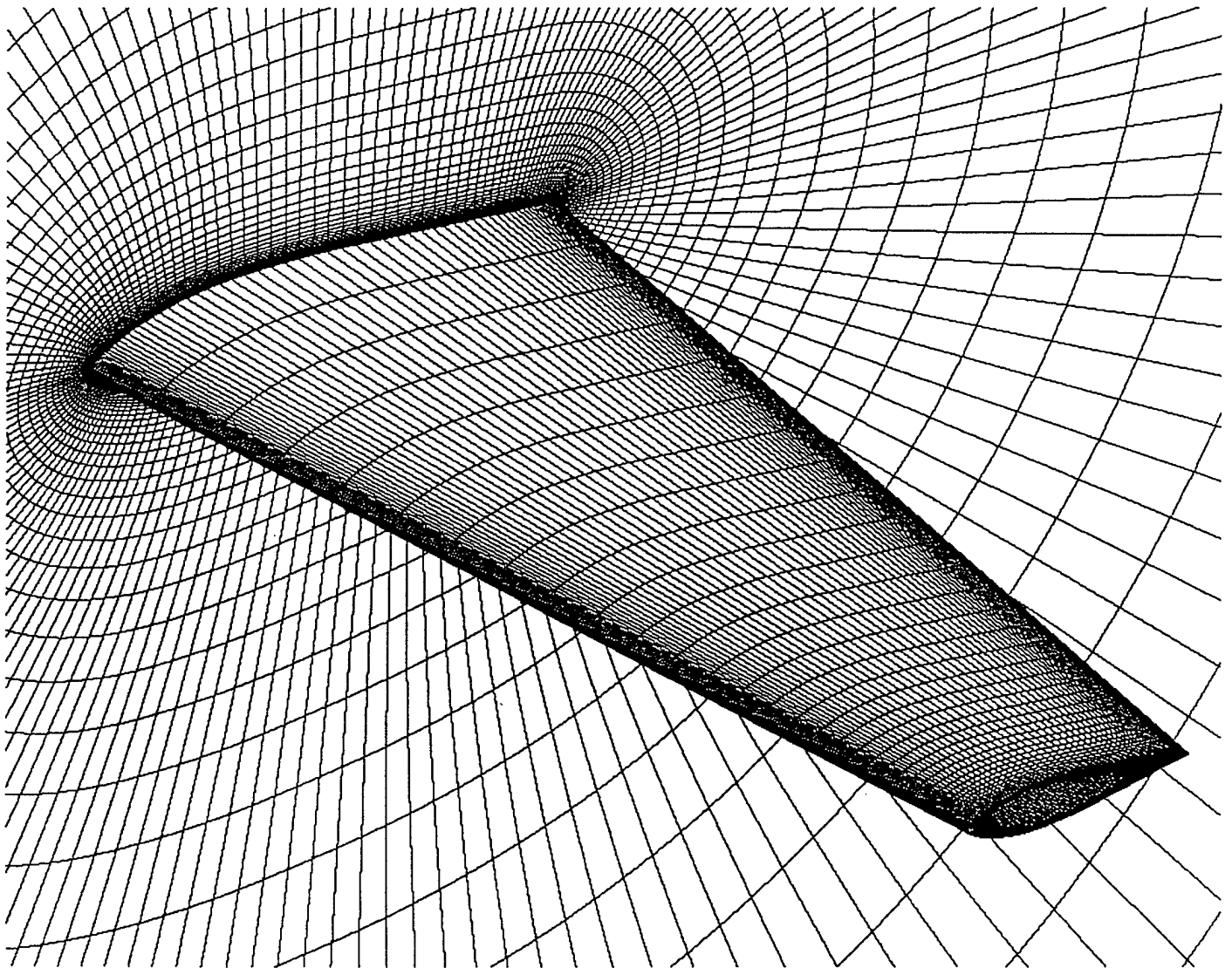
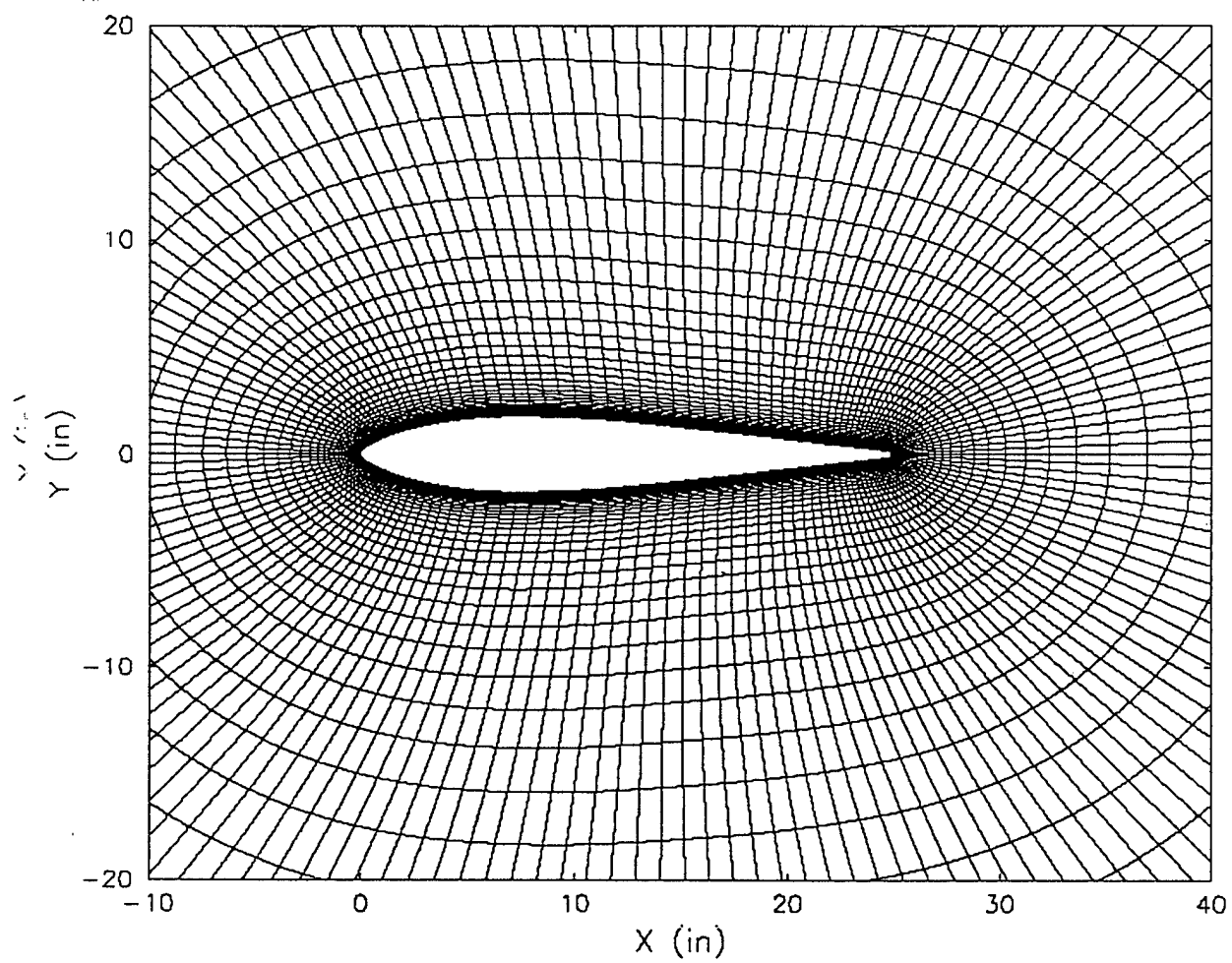
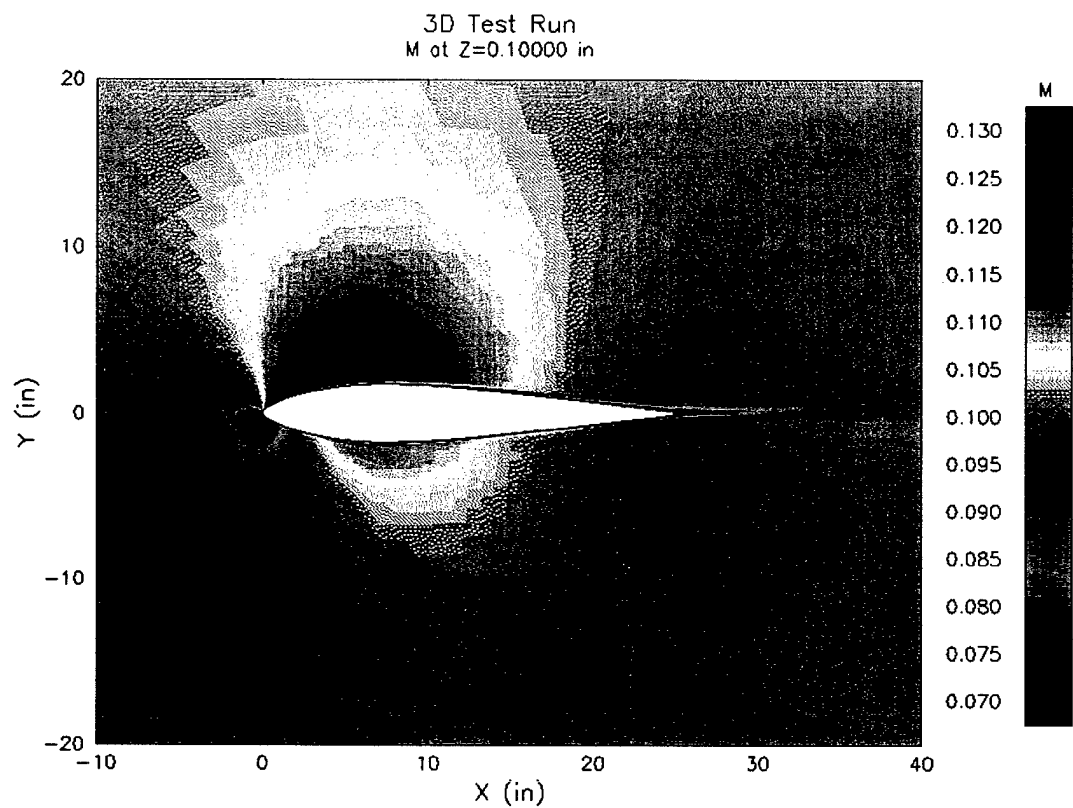


Figure: A-1 The grids for the wing surface and wing root are shown.



04-Dec-2001 17

Figure: A-2 Example of the grid for an airfoil cross-section. This particular airfoil cross-section is at the wing root.



04-Dec-2001 17:55:06

Figure: A-3 An example the Mach contours for a Mach 0.1 case with an angle of attack of 4 degrees. This cross section view is at the wing root.

Upper Surface C_p ; Mach 0.10; Alpha 4.0
+x Downstream; +y Vertical; +z Spanwise

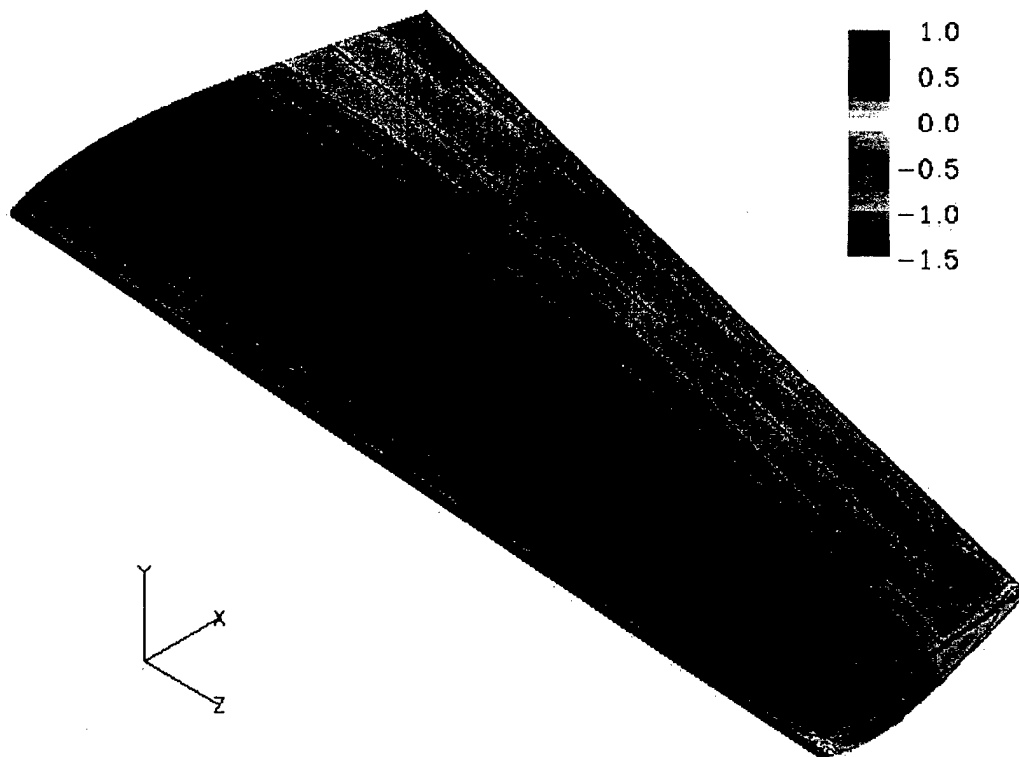


Figure: A-4 Dimensionless pressure coefficient (C_p) contours on the upper wing surface. This case is for Mach 0.1 and a 4 degree angle of attack.

Lower Surface C_p ; Mach 0.10; Alpha 4.0
+x Downstream; +y Vertical; +z Spanwise

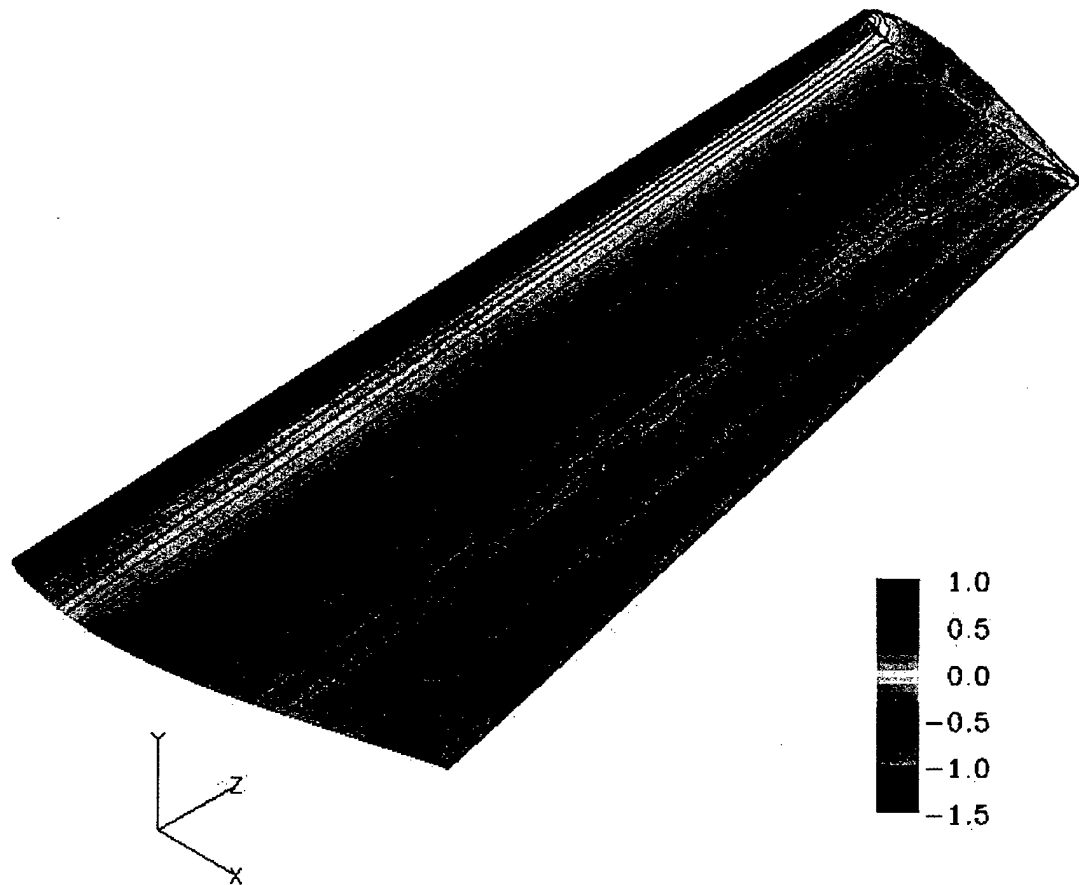


Figure: A-5 Dimensionless pressure coefficient (C_p) contours on the lower wing surface. This case is for Mach 0.1 and a 4 degree angle of attack.

B Sliding-Mode Control Applied to Aircraft Attitude Control

B.1 Introduction

B.1.1 Motivation

Attitude control systems are an integral part of all modern airplanes and other aircraft. The actuators used for attitude control are mostly hinged control surfaces. Most attitude control systems are based on linear systems theory. Indeed, most attitude control systems are based on classical single-input, single-output linear systems theory.

This is somewhat surprising given significant successes in past decades regarding the control of nonlinear systems in general and spatial mechanical systems in particular. One reason why nonlinear, geometrical methods have had little impact on practical attitude control is that they typically require sophisticated models that are difficult to determine practically. Another reason is that conventional methods work well enough under normal flight conditions that it is difficult to justify the cost and risk of using unconventional methods.

There are two obvious reasons for abandoning conventional attitude control methods. First, in the control of stealthy aircraft, hinged control surfaces are undesirable. Using fundamentally different actuators invalidates current methods, requiring immediate research and development. Second, conventional methods are not valid for arbitrarily large attitudinal errors. One would like to be able to recover from stalls, spins, and other extraordinary flight conditions.

This project is to apply geometrical sliding-mode control methods to attitude control of aircraft, especially airplanes. Sliding mode control is a well known method of robust trajectory control (Utkin, 1977; Slotine and Li, 1991; Hung et al., 1993). Most investigations have considered robust attitude control of spacecraft, see for example Vadali (1986); Dywer and Sira-Ramirez (1988); Iyer and Singh (1988); Robinett and Parker (1996); Tsiotras (1996). The attitude of a rigid body such as an idealized spacecraft can be represented in many ways (Shuster, 1993). Representations previously used in sliding mode attitude control include Euler angles (Iyer and Singh, 1988), Euler parameters (complete or reduced) (Vadali, 1986; Robinett and Parker, 1996) and (modified) Cayley-Rodrigues parameters (Dywer and Sira-Ramirez, 1988; Tsiotras, 1996). For example, Vadali (1986) uses a reduced set of Euler parameters (i.e., just the vector part) to regulate the attitude of a spacecraft. The sliding surface is defined as a linear combination of the body-relative angular velocities and the reduced Euler parameters. The desired reduced Euler parameters are assumed to be zero. Robinett and Parker (1996) use a complete set of Euler parameters to make a spacecraft track a desired attitude. They define attitude error as the algebraic difference between the reference Euler parameters and the actual parameters. The sliding surface is defined to be a linear combination of the attitude error and its temporal derivative. Iyer and Singh (1988) use Euler angles to make a spacecraft track a desired attitude. They define attitude error as the difference between the desired Euler angles and the actual Euler angles. The sliding surface is defined to be a linear combination of this error and its temporal derivative. Dywer and Sira-Ramirez (1988) use Cayley-Rodrigues parameters to regulate the attitude of a spacecraft. They define a sliding surface to be an abstract nonlinear function of the body-relative angular velocity and the desired and actual attitude parameters. The actual sliding surface is to be specified by the control system designer.

Two distinctions of the proposed methods from many reported methods are: (1) The measure of attitudinal error used is intrinsically defined, Euclidean-geometric, and intuitive. From Euler's theorem it follows that given a desired and actual attitude of a rigid body there exists an axis and angle of rotation relating the two attitudes. This defines a relative rotation (pseudo) vector, which is used as an intrinsically defined, intuitive measure of error. (2) A novel, dynamically nonlinear sliding function is used that results in a simple control law given suitable aircraft and actuator models. The parameters of this function are dynamically and geometrically intuitive.

The aforementioned methods are only applicable for large attitudinal errors given (1) a valid aircraft dynamic model and associated dynamic uncertainty model, and (2) an actuator quasistatic (quasisteady) model and associated uncertainty model. The phase one investigation shall focus on suitable airplane roll dynamic modelling and active flow control (AFC) actuator modelling. The AFC actuators shall ultimately be feedback controlled themselves to more predictably generate the moments required for attitude control.

All developed methods shall be as generic as possible, so that they are more readily extended to other airplane types, actuator types, and flight conditions. It is significant that the airplane and actuator uncertainty models are an integral part of the control algorithms. They are used to guarantee robustness even given crude airplane and actuator models.

B.1.2 Objectives

As shall be described in some detail, a sliding-mode attitude control paradigm is to be investigated. We shall focus on roll control in Phase I. The attitude controller determines a desired roll torque, which is to be achieved approximately by a subservient flow controller using flow sensors and active flow control (AFC) actuators. Both the magnitude and angular error bounds of the controlled roll torque must be estimated. Similarly, additional aerodynamic roll torques need to be measured or otherwise estimated. The magnitude and angular error bounds of this torque must be estimated.

In theory the error bounds could be quite large as long as sufficient control authority were available. Given the limited control authority of ACF actuators compared with conventional actuators, it may not be possible to control attitude given large error bounds (inaccurate models).

The technical objectives from the controls perspective are:

1. Develop generic attitude control algorithms based on sliding-mode methods.
2. Develop models of control and other aerodynamic torques and bound the errors of magnitude and direction of associated estimates.
3. See if the models are sufficiently accurate to guarantee acceptable performance given the limited control authority of AFC actuators.

B.2 Technical Details

B.2.1 Control Problem

Consider the problem of making an aircraft track a desired attitude trajectory. Attitude can be represented by a direction cosine matrix A_a . Rows of A_a are unit vectors of an aircraft (AC) frame in Earth-Centered Inertial (ECI) coordinates. Premultiplication by A_a is a transformation from ECI to AC coordinates. The desired attitude is represented by matrix A_d . Desired and actual aircraft attitude frames are depicted in Fig. B.1.

In general given a vector w , let \tilde{w} denote the *cross-product matrix* of w , the matrix \tilde{w} such that $\tilde{w}v = w \times v$ for any vector v , where \times denotes the Euclidean cross product. Let ω_a be the angular velocity of the aircraft in AC coordinates. The rate of change of attitude is given by

$$\dot{A}_a = -\tilde{\omega}_a A_a \quad (B.1)$$

The dynamics are assumed to be second order:

$$\dot{\omega}_a = f + Bu \quad (B.2)$$

In this equation f is the drift function, B is the input matrix, and u is an n -tuple of control inputs. In general f and B can be functions of any measurable variable including states. Let \hat{f} and \hat{B} be estimates of f and B . The extent of the model uncertainty is assumed to be bounded in the following way:

$$|\hat{f} - f| \leq F \quad (B.3)$$

$$B = (I + \Delta_B)\hat{B}, \text{ for } |\Delta_B| \leq D_B \quad (B.4)$$

where all inequality constraints and the absolute value function are applied element-wise. Tuple F bounds the uncertainty of f , matrix D_B the uncertainty of B .

Assume that the estimated input matrix, \hat{B} , and the actual input matrix, B , are always nonsingular and that $\hat{B} = B$ in the absence of parametric uncertainty ($\Delta_B = 0$). The problem is to make the aircraft attitude $A_a(t)$ track the desired attitude $A_d(t)$ in the presence of model uncertainty and disturbances.

B.2.2 Tracking Error

From Euler's theorem it follows that given a desired and actual attitude, A_d and A_a , there exists a unit axis e and an angle ψ of rotation relating the two attitudes. This defines a relative rotation vector, which can be used as a measure of error:

$$\theta_e = \psi e \quad (B.5)$$

where the angle of rotation ψ is restricted to the interval $[0, \pi]$ so that θ_e is uniquely defined. The error angle ψ and error axis e are depicted in Fig. B.1.

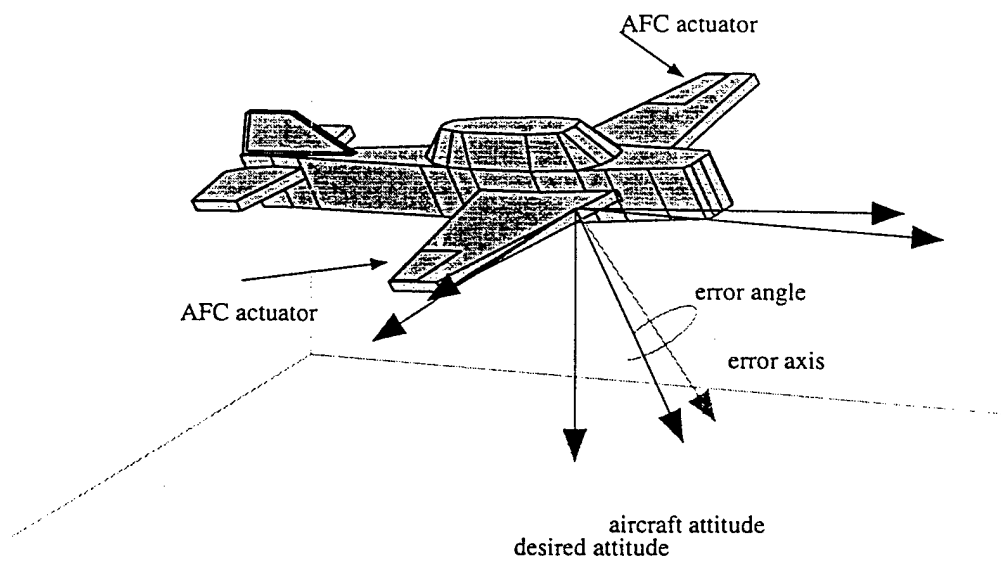


Figure B.1: Desired and actual aircraft attitude frames; attitudinal error angle and error axis

Attitudinal error can also be expressed as an error matrix, A_e , which is related to $\tilde{\theta}_e$ by the exponential:

$$A_e^T = A_d A_a^T = \exp(\tilde{\theta}_e) \quad (B.6)$$

At any instant, given A_d and A_a one can compute $A_e = A_a A_d^T$, from which the rotation vector parameters can be computed:

$$\psi = \cos^{-1} \left(\frac{\text{tr}(A_e) - 1}{2} \right) \quad (B.7)$$

$$e = -\frac{1}{\sin \psi} \text{as}(A_e) \quad (B.8)$$

where $\text{tr}(A_e)$ is the trace of A_e and $\text{as}(A_e)$ is the antisymmetric part of A_e . Axis e has been computed in AC coordinates. The derivative of A_e can be expressed as an angular velocity, ω_e :

$$\dot{A}_e = -\tilde{\omega}_e A_e \quad (B.9)$$

From (B.6) it follows that

$$\tilde{\omega}_e = -\dot{A}_e A_e^T = \tilde{\omega}_a - A_e \tilde{\omega}_d A_e^T \quad (B.10)$$

This is equivalent to the vector equation

$$\omega_e = \omega_a - A_e \omega_d \quad (B.11)$$

where ω_a is the actual angular velocity and ω_d is the desired angular velocity (in desired AC coordinates). This is in (actual) AC coordinates.

Deriving the rate of change of θ_e is somewhat involved. Readers are referred to Appendix B of Goeree et al. (1997) for details. If $\psi = 0$ then

$$\dot{\theta}_e = \omega_e \quad (B.12)$$

Otherwise

$$\dot{\theta}_e = \left[\frac{\psi}{2 \sin \psi} (\text{tr}(A_e)I - A_e) + \left(1 - \cos \psi \frac{\psi}{\sin \psi} \right) ee^T \right] \omega_e \quad (B.13)$$

The angular acceleration is found by differentiating (B.11).

$$\dot{\omega}_e = \dot{\omega}_a + \tilde{\omega}_e A_e \omega_d - A_e \dot{\omega}_d \quad (B.14)$$

In the control law θ_e , ω_e and $\dot{\omega}_e$ must be computed.

B.2.3 General Case: Attitude Control of Spatial Mechanical Systems

The first step is to define a sliding surface that achieves a set of desired error dynamics.

Sliding Variable and Surface Define the sliding variable s as:

$$s = \omega_e + \Lambda \theta_e \quad (\text{B.15})$$

where Λ is a 3×3 , symmetric, positive-definite matrix. Sliding variable s is a linear combination of ω_e and θ_e . The angular velocity difference ω_e is not the rate of change of error θ_e . The desired error dynamics corresponding to $s = 0$ are therefore dynamically nonlinear. This definition results in a simple control law. The dynamic behavior is intuitive, despite the dynamic nonlinearity. A more in-depth discussion of the behavior and the selection of Λ is given in Goeree and Fasse (2000).

Because the sliding function is nonlinear we must analyze the stability of the error dynamics. Define function V to be the square of the rotation angle:

$$V = \psi^2 = \theta_e^T \theta_e \quad (\text{B.16})$$

The rate of change of the rotation angle equals the projection of the angular error velocity on θ_e (Shuster, 1993):

$$\dot{\psi} = e^T \omega_e = \frac{1}{\psi} \theta_e^T \omega_e \quad (\text{B.17})$$

The rate of change of V is

$$\dot{V} = 2\psi\dot{\psi} = 2\theta_e^T \omega_e = 2\theta_e^T (s - \Lambda \theta_e) \quad (\text{B.18})$$

If the sliding variable is kept at zero then the rate of change is strictly negative because Λ is symmetric and positive-definite. If the sliding variable is kept at zero, V is a Lyapunov function and the error goes to zero.

Tracking Error Bounds Bounds on the sliding variable can be translated into bounds on the tracking error. From (B.18) the rate of change of ψ satisfies

$$\dot{\psi} + \psi e^T \Lambda e = e^T s \quad (\text{B.19})$$

This is a nonlinear differential equation for ψ because e is not a constant. It follows that

$$\dot{\psi} + \lambda_{\min} \psi \leq \|s\|_2 \quad (\text{B.20})$$

where $\lambda_{\min} > 0$ is the smallest eigenvalue of Λ . Assuming that the magnitude of $s(t)$ is bounded by ϕ for all time, then angular error ψ is bounded as well (Slotine and Li, 1991):

$$\psi \leq \epsilon = \frac{\phi}{\lambda_{\min}} \quad (\text{B.21})$$

Sliding Conditions To guarantee that the sliding variable s indeed approaches the sliding surface $s = 0$ we choose the control law such that each s_i^2 is a Lyapunov-like function. The rate of change of these functions is negative-definite if for each index i the sliding conditions are satisfied:

$$\frac{1}{2} \frac{d}{dt} s_i^2 = s_i \dot{s}_i \leq -\eta_i |s_i| \quad (\text{B.22})$$

If the sliding variable is initially off the sliding surface, the sliding surface will be reached in finite *reaching time* bounded by (Slotine and Li, 1991):

$$t_{ri} \leq \frac{|s_i(t=0)|}{\eta_i} \quad (\text{B.23})$$

Parameter η_i determines the maximum reaching time.

Control Law The selected control law is the sum of the *equivalent* control term, u_{eqv} , and the *robust* control term, u_{rob} :

$$u = u_{eqv} - u_{rob} \quad (\text{B.24})$$

The equivalent control term uses the dynamic model of the system to keep the sliding variable on the sliding surface in the absence of errors. This is achieved by letting the rate of change of the sliding variable be zero. From the definition of the sliding variable (B.15) follows

$$\dot{s} \equiv 0 = \dot{\omega}_e + \Lambda \dot{\theta}_e \quad (\text{B.25})$$

Using expression (B.14) for the angular error acceleration

$$\dot{s} \equiv 0 = \dot{\omega}_a - A_e \dot{\omega}_d + \tilde{\omega}_a A_e \omega_d + \Lambda \dot{\theta}_e \quad (\text{B.26})$$

Using the estimate of the system dynamics (B.2) one can solve for the equivalent control: $u = u_{eqv}$:

$$u_{eqv} = \hat{B}^{-1}(-\hat{f} + A_e \dot{\omega}_d - \tilde{\omega}_a A_e \omega_d - \Lambda \dot{\theta}_e) \quad (\text{B.27})$$

The robust control term ensures that the sliding conditions are met in the presence of model uncertainty. Let k be a three-tuple with strictly positive elements. The robust term is assumed to be of the form

$$u_{rob} = \hat{B}^{-1} \check{k} \text{sign}(s) \quad (\text{B.28})$$

where the sign function operates element-wise on s and \check{k} denotes the diagonal matrix with the elements of k on the diagonal. Three-tuple k must be chosen so that the sliding conditions (B.22) are satisfied. A particular choice that satisfies these constraints is

$$k = (I - D_B)^{-1} (F + D_B |-\hat{f} + A_e \dot{\omega}_d - \tilde{\omega}_a A_e \omega_d - \Lambda \dot{\theta}_e| + \eta) \quad (\text{B.29})$$

The discontinuous control law leads in practice to chattering. Therefore the discontinuous control law is approximated by a continuous control law in a thin (control) boundary layer. This is standard practice, see Goeree and Fasse (2000); Slotine and Li (1991) for mathematical details.

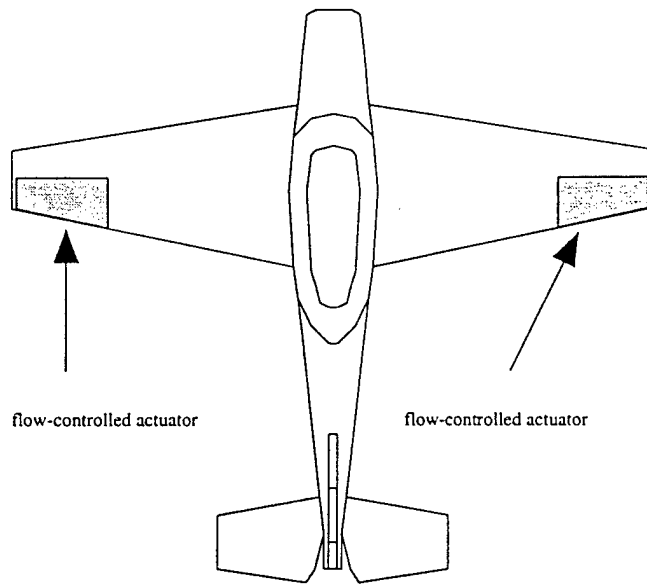


Figure B.2: Aircraft planform

Qualitatively, outside the boundary layer the control law is chosen as before. Hence, outside the boundary layer the sliding conditions (B.22) are satisfied. All system trajectories approach the boundary layer. Once inside the boundary layer the sliding conditions guarantee that the system trajectories remain there, so that the boundary layer is an invariant set. Interpolation of the control law in the boundary layer leads to tracking within a guaranteed precision rather than the theoretically perfect tracking. One can show (Slotine and Li, 1991) that smoothing the control discontinuity inside the boundary layer in effect assigns a low pass filter structure to the local dynamics of the sliding variables. Chattering can be eliminated by choosing the boundary layer thickness such that unmodeled high-frequency dynamics are not excited.

B.2.4 Attitude Control of Aircraft

General The aircraft is assumed to be actuated by a set of active flow control (AFC) actuators. The Phase I prototype will have a pair of such actuators as indicated in Fig. B.2. The AFC actuators will likely be actively controlled to achieve desired control torques. This shall be discussed to an extent in the sequel.

The attitude dynamics are

$$\dot{\omega}_a = -J_a^{-1} \tilde{\omega}_a J_a \omega_a + J_a^{-1} (\tau_{act} + \tau_{ext}) \quad (B.30)$$

where J_a is the aircraft inertia matrix, τ_{act} is the net actuator torque, and τ_{ext} is the remainder of the net external torque due primarily to aerodynamic forces. All entities are in AC coordinates.

For tracking controller design we introduce the input u , which is simply the nominal net actuator torque (the nominal τ_{act}). These two variables are related by the expression

$$\tau_{act} = (I + \Delta_E)u, \text{ with } |\Delta_E| \leq D_E \quad (B.31)$$

for some hopefully small bounding matrix D_E . These bounds will depend on how accurately the AFC actuators can be modelled and controlled. Rather than using elaborate analysis we envision choosing this matrix as follows. An "error" is a deviation of actual net torque from nominal net torque. Assume that the maximum fractional error of torque magnitude is d_{act} . Assume that the maximum angular error of torque direction is θ_{act} . Then matrix D_E is given by

$$D_E = \begin{bmatrix} d_{act} & (1 + d_{act})\theta_{act} & (1 + d_{act})\theta_{act} \\ (1 + d_{act})\theta_{act} & d_{act} & (1 + d_{act})\theta_{act} \\ (1 + d_{act})\theta_{act} & (1 + d_{act})\theta_{act} & d_{act} \end{bmatrix} \quad (B.32)$$

Using the nominal net torque as control input the dynamic equation is equivalent to (B.2), where

$$f = -J_a^{-1} \tilde{\omega}_a J_a \omega_a + J_a^{-1} \tau_{ext} \quad (B.33)$$

$$B = J_a^{-1} (I + \Delta_E) \quad (B.34)$$

The estimates of f and B are

$$\hat{f} = -\hat{J}_a^{-1} \tilde{\omega}_a \hat{J}_a \omega_a + \hat{J}_a^{-1} \hat{\tau}_{ext} \quad (B.35)$$

$$\hat{B} = \hat{J}_a^{-1} \quad (B.36)$$

The inertia matrix is assumed to be nearly equal to its estimate, so that

$$J_a = (I + \Delta_J) \hat{J}_a, \text{ with } |\Delta_J| \leq D_J \quad (B.37)$$

for some small bounding matrix D_J . To first order:

$$J_a^{-1} \approx \hat{J}_a^{-1} (I - \Delta_J) \approx (I - \Delta_J^T) \hat{J}_a^{-1} \quad (B.38)$$

because matrices J_a and \hat{J}_a are symmetric.

The net external torque is assumed to have bounded magnitude:

$$\|\tau_{ext}\|_2 \leq \tau_{max} \quad (B.39)$$

for some positive scalar τ_{\max} . In theory this bound and all of the bounding matrices could vary with time. This assumption shall be made more realistic in the future using methods like those used to model the uncertainty of the actuator torques.

The next step is to translate the various physical parameter error bounds into error bounds of drift \mathbf{f} and input matrix \mathbf{B} . To first order the difference between the actual and estimated drift is

$$\mathbf{f} - \hat{\mathbf{f}} \approx -\hat{\mathbf{J}}_a^{-1} (\Delta_J \tilde{\omega}_a - \tilde{\omega}_a \Delta_J) \hat{\mathbf{J}}_a \omega_a + \hat{\mathbf{J}}_a^{-1} (\mathbf{I} - \Delta_J) \tau_{\text{ext}} \quad (\text{B.40})$$

The magnitude of uncertainty can next be bounded by using the Euclidean matrix norm and the physical parameter uncertainty bounds:

$$\|\mathbf{f} - \hat{\mathbf{f}}\| \leq \mathbf{F} = 2\|\hat{\mathbf{J}}_a^{-1}\|_2 \|\mathbf{D}_J\|_2 \|\hat{\mathbf{J}}_a\|_2 \|\omega_a\|_2^2 \mathbf{1} + \|\hat{\mathbf{J}}_a^{-1}\|_2 (1 + \|\mathbf{D}_J\|_2) \tau_{\max} \mathbf{1} \quad (\text{B.41})$$

where $\mathbf{1} = [1; 1; 1]$ is a column matrix of ones.

Next consider the uncertainty of \mathbf{B} . Using equations (B.38) and (B.34) it is true to first order that

$$\mathbf{B} \approx (\mathbf{I} - \Delta_J^T) \hat{\mathbf{J}}_a^{-1} (\mathbf{I} + \Delta_E) \quad (\text{B.42})$$

Let $\Delta'_E = \hat{\mathbf{J}}_a^{-1} \Delta_E \hat{\mathbf{J}}_a$ such that $\Delta'_E \hat{\mathbf{J}}_a^{-1} = \hat{\mathbf{J}}_a^{-1} \Delta_E$. Then it is true to first order that

$$\mathbf{B} \approx (\mathbf{I} - \Delta_J^T + \Delta'_E) \hat{\mathbf{J}}_a^{-1} = (\mathbf{I} - \Delta_J^T + \Delta'_E) \hat{\mathbf{B}} \quad (\text{B.43})$$

It is clear that the uncertainty of the input matrix is

$$\Delta_B = -\Delta_J^T + \Delta'_E \quad (\text{B.44})$$

Next we make a critical but gratuitous assumption:

$$\|\Delta_E\| \leq \mathbf{D}'_E = \hat{\mathbf{J}}_a^{-1} \mathbf{D}_E \hat{\mathbf{J}}_a \quad (\text{B.45})$$

While this is a reasonable approximation, it is probably not true in general. An upper bound of the extent of uncertainty on the input matrix is then

$$\mathbf{D}_B = \mathbf{D}_J^T + \mathbf{D}'_E \quad (\text{B.46})$$

With these bounds on the uncertainty the control law presented in Sec. 3 can be used.

Specific Example As an example of a simple aerodynamic model consider that given in Isidori (1995). The aircraft is described by a standard forward-right-down frame centered at the center of mass, as indicated in Fig. B.1. The three components of the aircraft angular velocity ω_a are the roll, pitch and yaw rates. As before, the angular velocity dynamics are given by (B.30). The linear velocity dynamics are

$$\dot{\mathbf{v}}_a^0 = \frac{1}{m} \mathbf{f}^0 \quad (\text{B.47})$$

where \mathbf{v}_a^0 is the aircraft velocity in inertial coordinates, m is the mass, and \mathbf{f}^0 is the net force acting on the aircraft in inertial coordinates.

The velocity of the aircraft in body coordinates is

$$\mathbf{v}_a = \mathbf{A}'_a \mathbf{v}_a^0 \quad (\text{B.48})$$

The angle-of-attack α and sideslip angle β are

$$\alpha = \tan^{-1} \left(\frac{-v_{3a}}{v_{1a}} \right) \quad (\text{B.49})$$

$$\beta = \sin^{-1} \left(\frac{-v_{2a}}{v} \right) \quad (\text{B.50})$$

where $v = \|\mathbf{v}_a^0\| = \|\mathbf{v}_a\|$ is the speed.

A model of the external, aerodynamic forces is

$$\boldsymbol{\tau}_{\text{ext}} = v \begin{bmatrix} a_{12}\omega_{3a} + a_{13}\omega_{1a} \\ a_{23}\omega_{2a} \\ a_{32}\omega_{3a} + a_{33}\omega_{1a} \end{bmatrix} + v^2 \begin{bmatrix} a_{11} \sin \beta \\ a_{21} + a_{22} \sin \alpha \\ a_{31} \sin \beta \end{bmatrix} \quad (\text{B.51})$$

A model of the actuation torques is

$$\boldsymbol{\tau}_{\text{act}} = v^2 \mathbf{B}_{\text{aero}} \mathbf{u} = v^2 \begin{bmatrix} b_{11} \cos \beta & 0 & b_{13} \cos \beta \\ 0 & b_{22} \cos \alpha & 0 \\ 0 & 0 & b_{33} \cos \beta \end{bmatrix} \mathbf{u}_{\text{aer}} \quad (\text{B.52})$$

where $\mathbf{u}_{\text{aer}} = [u_{\text{ael}}; u_{\text{elv}}; u_{\text{rud}}]$ is a three-tuple of aileron, elevator and rudder inputs.

Assume that an estimate of the angular velocity is available via a three-axis gyroscope. Assume that only crude estimates of the angle of attack and sideslip are available. In particular they may be constants associated with a trim condition. In this case the estimated aerodynamic torques are

$$\hat{\boldsymbol{\tau}}_{\text{ext}} = \hat{v} \begin{bmatrix} \hat{a}_{12}\omega_{3a} + \hat{a}_{13}\omega_{1a} \\ \hat{a}_{23}\omega_{2a} \\ \hat{a}_{32}\omega_{3a} + \hat{a}_{33}\omega_{1a} \end{bmatrix} + \hat{v}^2 \begin{bmatrix} \hat{a}_{11} \sin \hat{\beta} \\ \hat{a}_{21} + \hat{a}_{22} \sin \hat{\alpha} \\ \hat{a}_{31} \sin \hat{\beta} \end{bmatrix} \quad (\text{B.53})$$

A model of the actuation torques is

$$\hat{\boldsymbol{\tau}}_{\text{act}} = \hat{v}^2 \hat{\mathbf{B}}_{\text{aero}} \mathbf{u} = \hat{v}^2 \begin{bmatrix} \hat{b}_{11} \cos \hat{\beta} & 0 & \hat{b}_{13} \cos \hat{\beta} \\ 0 & \hat{b}_{22} \cos \hat{\alpha} & 0 \\ 0 & 0 & \hat{b}_{33} \cos \hat{\beta} \end{bmatrix} \mathbf{u}_{\text{aer}} \quad (\text{B.54})$$

Remember that the sliding mode control input \mathbf{u} is the nominal net actuator torque, $\hat{\boldsymbol{\tau}}_{\text{act}}$. Given the desired \mathbf{u} one can compute a set of approximately corresponding actuator commands:

$$\mathbf{u}_{\text{aer}} = \frac{1}{\hat{v}^2} \hat{\mathbf{B}}_{\text{aero}}^{-1} \mathbf{u} = \frac{1}{\hat{v}^2} \hat{\mathbf{B}}_{\text{aero}}^{-1} \hat{\boldsymbol{\tau}}_{\text{act}} \quad (\text{B.55})$$

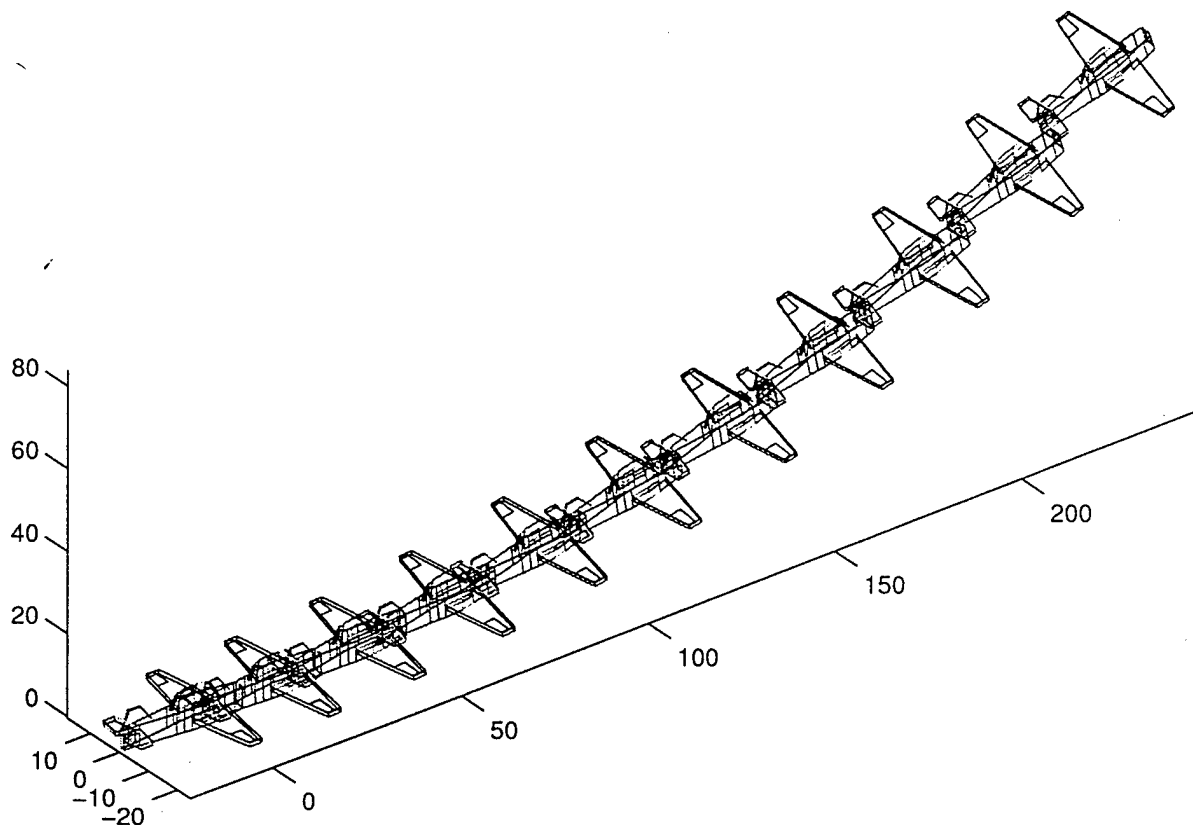


Figure B.3: Desired trajectory

B.3 Simulation Results

The attitude controller has been simulated using Matlab. A detailed discussion of the simulation and results is outside the scope of this report. Graphical results are shown in Figs. B.3–B.3.

Figure B.3 shows the desired trajectory. The desired attitude trajectory is simple, having constant desired roll and pitch rates. During the maneuver the airplane is accelerating with a constant thrust. The rectilinear motion of the airplane is determined by a simple aerodynamic model. Details of the model are not given so as not to distract from the more important attitude dynamic model.

Without feedback control the system is unstable, as evidenced by Fig. B.4. With feedback control the airplane follows the desired trajectory as seen in Fig. B.3.

The simulation results suggest that the theoretical results are self-consistent and potentially useful.

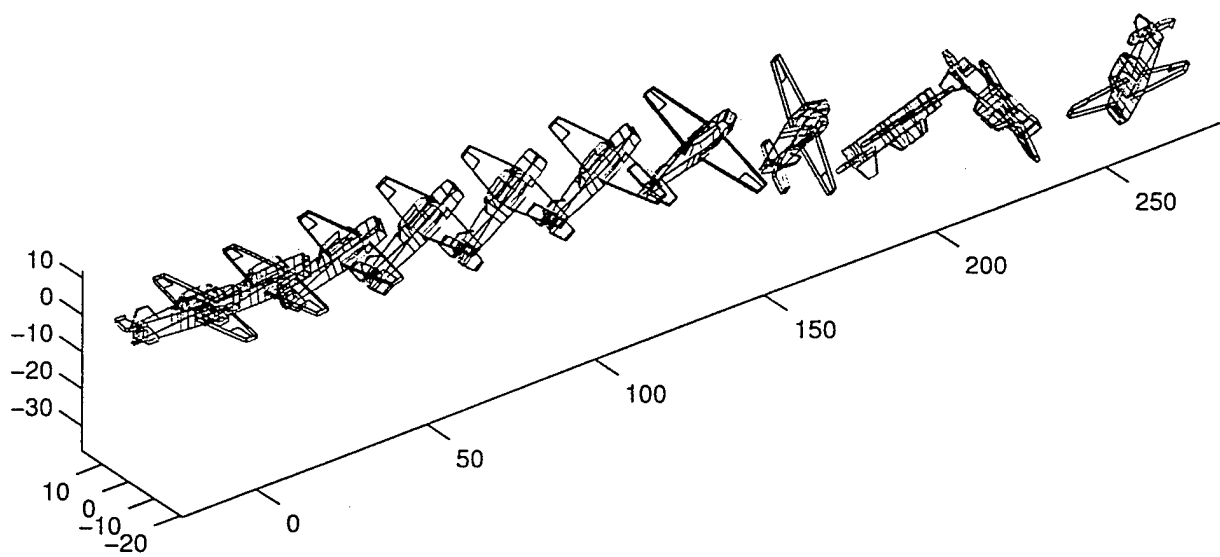


Figure B.4: Trajectory without attitude control

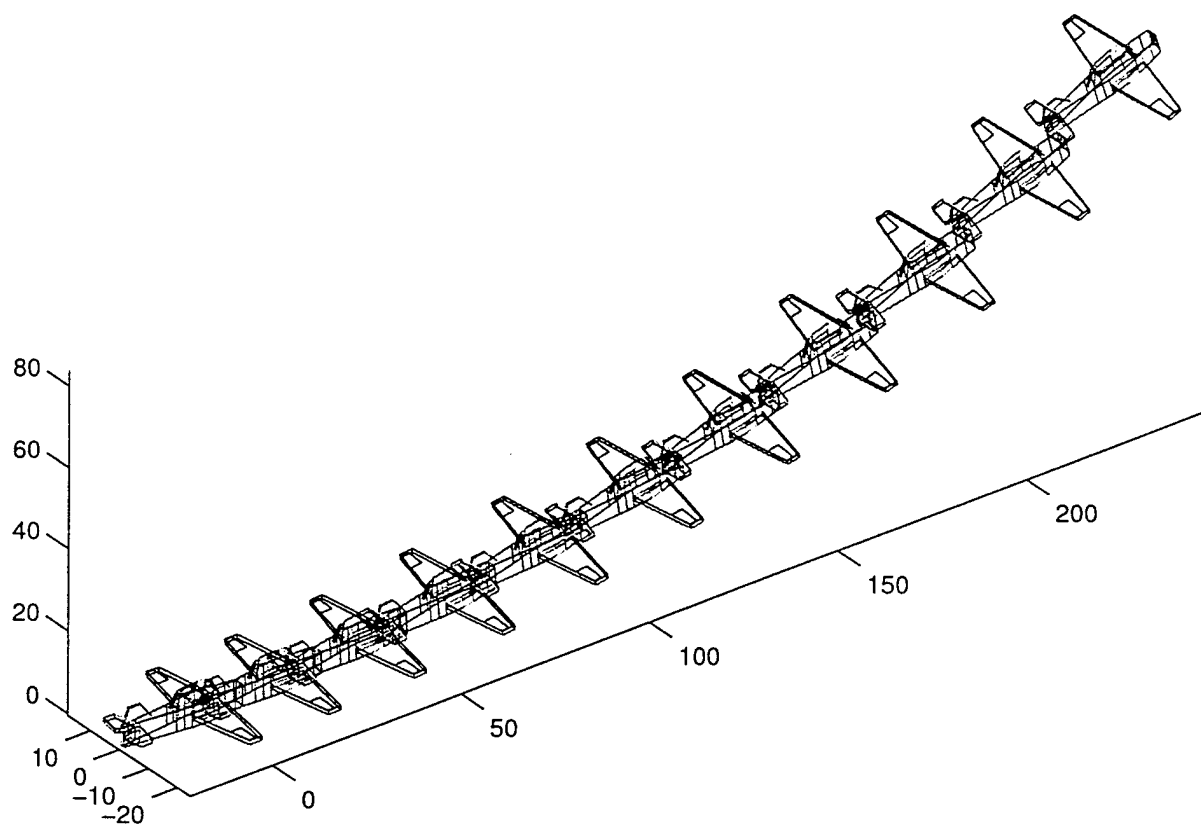


Figure B.5: Trajectory with attitude control

Acknowledgement

The successful development of the flight model would not have been possible without the contribution of our graduate students Tim Roediger, Armin Kurz, Andreas Gross and Lian Yuan and undergraduate students Chris Ruelle and Kevein Hess. We would also like to acknowledge our pilots, Jason Shulman and Dr. Michael Marcellin, whose expertise was essential for completing the very ambitious flight demonstration program in the short time available to the program.

References

- A. Cain and R. Bush. Numerical wave propagation on stretched grids. Technical Report 94-0172, AIAA, 1994.
- M. Choudhari and E. J. Kerschen. Instability wave patterns generated by interaction of sound waves with three-dimensional wall suction or roughness. AIAA Paper 90-0119, AIAA, 1990.
- T. Dywer, III. and H. Sira-Ramirez. Variable structure control of spacecraft attitude maneuvers. *AIAA J. of Guidance, Control and Dynamics*, 11:262–270, 1988.
- B. Goeree and E. Fasse. Sliding mode attitude control of a small satellite for ground tracking maneuvers. In *Proceedings of the American Control Conference*, pages 1134–1138, Chicago, IL, June 2000.
- B. Goeree, E. Fasse, M. Tiernego, and J. Broenink. Sliding mode control of spatial mechanical systems decoupling translation and rotation. In *Proc. of the ASME Dynamic Systems and Control Division*, volume 61, pages 545–554, 1997.
- D. Greenblatt and I. J. Wygnanski. The control of flow separation by periodic excitation. *Progress In Aerospace Sciences*, 36(7):487–545, Oct. 2000.
- P. Huerre and P. A. Monkewitz. *Annual Review of Fluid Mechanics*, volume 22, chapter Local and Global Instabilities in Spatially Developing Flows, pages 473–537. Annual Reviews Inc., 1990.
- J. Hung, W. Gao, and J. Hung. Variable structure control: A survey. *IEEE Trans. on Industrial Electronics*, 4:2–22, 1993.
- A. Isidori. *Nonlinear Control Systems*. Springer, third edition, 1995.
- D. M. Israel and H. F. Fasel. Numerical investigation of compressibility effects on active control of boundary layer separation. AIAA Paper 2000-2771, AIAA, June 2001.
- D. M. Israel and H. F. Fasel. Numerical investigation of turbulent separation control using periodic disturbances. AIAA Paper 2000-0409, AIAA, Jan. 2002.

- A. Iyer and S. Singh. Variable structure control of decoupleable systems and attitude control of spacecraft in presence of uncertainty. In *Proc. American Control Conference*, pages 2238–2243, 1988.
- E. J. Kerschen. Boundary layer receptivity. AIAA Paper 89-1109, AIAA, 1989.
- R. H. Leibbeck. Design of subsonic airfoils for high lift. *J. Aircraft*, 15:547–561, 1978.
- L. G. Pack and A. Seifert. Dynamics of active separation control at high Reynolds numbers. AIAA Paper 2000-0409, AIAA, Jan. 2000.
- W. H. Press, B. P. Flannery, S. A. Teukolsky, and W. Vetterling. *Numerical Recipes*. Cambridge University Press, 1986.
- R. B. Rivir, R. Sondergaard, J. P. Bons, and J. P. Lake. Passive and active control of separation in gas turbines. AIAA Paper 2000-2235, AIAA, June 2000. Fluids 2000.
- R. Robinett and G. Parker. Spacecraft Euler parameter tracking of large angle maneuvers via sliding mode control. *AIAA J. of Guidance, Control and Dynamics*, 19:702–703, 1996.
- C. W. Rowley, D. R. Williams, T. Colonius, R. M. Murray, D. G. MacMartin, and D. Fabris. Model-based control of cavity oscillations part ii: System identification and analysis. AIAA-Paper 2002-0972, AIAA, Jan. 2002. 40th AIAA Aerospace Sciences Meeting & Exhibit.
- A. Seifert and L. G. Pack. Active control of separated flows on generic configurations at high Reynolds numbers. AIAA Paper 99-3403, AIAA, June 1999.
- A. Seifert and L. G. Pack. Sweep and compressibility effects on active separation control at high Reynolds numbers. AIAA Paper 2000-0410, AIAA, Jan. 2000.
- M. Shuster. A survey of attitude representations. *J. of the Astronautical Sciences*, 41:439–517, 1993.
- J.-J. Slotine and W. Li. *Applied Nonlinear Control*. Prentice Hall, New Jersey, 1991.
- B. S. Stratford. An experimental flow with zero skin friction throughout its region of pressure rise. *Journal of Fluid Mechanics*, 5:17–35, 1959.
- P. Tsiotras. Stabilization and optimality results for the attitude control problem. *AIAA J. of Guidance, Control and Dynamics*, 19:772–779, 1996.
- V. Utkin. Variable structure systems with sliding modes. *IEEE Trans. on Automatic Control*, 22: 212–222, 1977.
- S. Vadali. Variable structure control of spacecraft large angle maneuvers. *AIAA J. of Guidance, Control and Dynamics*, 9:235–239, 1986.